All Theses and Dissertations (ETDs)

1-1-2011

Ultra-high-Q Microresonator with Applications towards Single Nanoparticle Sensing

Jiangang Zhu
Washington University in St. Louis

Follow this and additional works at: https://openscholarship.wustl.edu/etd

WASHINGTON UNIVERSITY IN ST. LOUIS

School of Engineering and Applied Science

Department of Electrical and Systems Engineering

Dissertation Examination Committee:
Lan Yang, Chair
Stephen Arnold
Da-Ren Chen
Arye Nehorai
Jung-Tsung Shen
Barry Spielman
Frank Vollmer

Ultra-high-Q Microresonator with Applications towards Single Nanoparticle Sensing

by

Jiangang Zhu

A dissertation presented to the Graduate School of Arts and Sciences
of Washington University in partial fulfillment of the
requirements for the degree of

DOCTOR OF PHILOSOPHY

December 2011
Saint Louis, Missouri

ABSTRACT OF THE DISSERTATION

Ultra-high-Q Microresonator with Applications towards Single Nanoparticle Sensing

by

Jiangang Zhu

Doctor of Philosophy in Electrical Engineering

Washington University in St. Louis, 2011

Research Advisor: Professor Lan Yang

Whispering-gallery mode microcavities confines light and enables enhanced light-matter interaction. They are great platforms for enhanced light-matter interactions. Using ultra-high-Q microtoroids and focusing on a phenomenon called mode splitting, we demonstrate the theory and experiments for real-time and label-free detection and size measurement of individual nanoparticles and viruses, with a theoretical size limit of $R < 10$ nm. It enables us to cover a large range of virus and nanoparticle sizes of great interest for biomedicine, nanotechnology, and environmental science. Moreover, this approach allows to identify the components of homogenous mixtures of particles. It exceeds the capabilities of existing schemes with its unique single particle resolution and ability for quantitative size measurement of individual nanoparticles. The techniques described here also pave the way for using active lasing microresonators as particle sensors, in which mode splitting serves as the origin of the radio frequency beatnote in the laser which indicates the binding of nanoparticles. It also lays a solid ground for using microresonators for bio-molecule detection. In addition, two non-spectrogram gased nanoparticle detection techniques: fiber taper detection and

resonator reflection mode detection are demonstrated and future implementation on bimolecular detections are discussed.

Acknowledgments

Contents

List of Tables

List of Figures

ix

xiii

Chapter 1

Introduction

1.1 Dissertation Outline

Nanoparticle detection and characterization techniques have been widely sought as the awareness of the potential benefits and risks of the continuously generated by-product or massively synthesized nanoparticles are increasing (Colvin 2003, Hoet, Bruske-Hohlfeld and Salata 2004). Nanoparticles of special interests range from biological agents and virions to specially synthesized semiconductor, metal and polymer nanoparticles. While the detection of the former is important for bio-defense and early detection of pandemic outbreaks, detection and characterization of the latter group of nanoparticles are indispensable for their broad range of applications in nanotechnology.

In addition to conventional microscopic techniques which, despite their high sensitivity and resolution, are not suitable for field measurements due to their expensive and bulky constructions, long processing times and the necessity of pre-treatment (labeling with fluorescent dyes, etc.) of the particles, there exist many variations of optical particle counters (Gucker and Rose 1954, Heringa et. al. 2005) which rely on light scattering measurements, allow field measurements, detect and count individual or ensemble of particles. These counters require off-axis detectors for the collection of the scattered light, have bulky configurations and require sophisticated signal processing.

Recently, there is a growing interest for nanoparticle detection using nano- and micro-scale sensors, which, with their unprecedented sensitivity, have the potential for in-situ sensing. The nano/micro-mechanical sensors (Burg et.al. 2007, Naik et.al. 2009) detect particles by monitoring the resonance frequency changes caused by the additional effective mass of the binding particles, while resonator-based micro/nano-optical resonator sensors rely on the resonance frequency shift (Vollmer and Arnold 2008, White, Oveys and Fan 2006) due to the change in the effective polarizability of the resonator-environment system upon particle binding. Detecting and counting individual nanoparticles as small as radius R=12.5 nm (Lu et. al. 2010) and single molecules (A. M. Armani et.al. 2007) has been reported (There is question on the validity of Armani's results, see discussions by Arnold, Shopova and Holler 2010). This high sensitivity is attributed to the resonance enhanced interaction between the particle and the evanescent tail of the light field due to tight light confinement and extended interaction time provided by the high quality factor (Q) resonance.

Silica microtorid (D. K. Armani et.al. 2003) with its ultra-high quality factor ($> 10^8$) and very small mode volume ($< 200\mu m^3$ for a microtoroid with major diameter $< 40\mu m$), is a very good candidate for sensor. Its properties make it easier to evoke a phenomenon call mode splitting (Weiss et.al. 1995, Kippenberg, Spillane and Vahala 2002, Mazzei et. al. 2007). In this dissertation we utilized this phenomenon and found that it not only allows us to detect single naoparticles but also to gives us the capability to measure them. We hence developed the techniques of detecting and sizing consecutively adsorbed nanoparticles using microtoroid.

1.2 Chapter Overview and Collaborative Work

Chapter 2 is an introduction to optical microresonators. Different aspects of the microresonators, such as their geometry, quality factor and coupling methods are introduced. The main device for this dissertation is microtoroid, on which the fabrication and measurement techniques are discussed. Its physical properties are also analyzed. Microtoroid is a excellent platform for sensor. A few applications such as temperature and humidity sensing are studied in this chapter.

Chapter 3 focuses on the application of single nanoparticle detection and sizing using mode splitting phenomenon in microtorid. A detailed theoretical and experimental analysis is presented and it's advantage and limitations are analyzed. The particle delivery system used in this dissertation is developed by our collaborator Da-Ren Chen, Lin Li and Qisheng Ou.

Chapter 4 solves the problems on interaction between multiple particles and a resonator. Through the developed theory a new experiment procedure is developed to measure each consecutively adsorbed particles on the resonator surface. It enables detecting and sizing individual virions and inorganic particles, as well as discriminating the modality in particle mixtures. A detailed analysis section is included to study the efficiency and performance of this measurement scheme.

Chapter 5 demonstrates two non-spectrogram based single nanoparticle detection scheme. The first one utilizes particle induced back scattering in a resonator-taper system. Theory and experiments are presented and accordingly, unprecedented sensitivity is projected. The second scheme bases on a simple tapered fiber. Theory and experiments are presented to show that with its exposed guided optical mode, the tapered fiber is a convenient and cost effective sensor to detect nanoparticles.

Chapter 6 is a conclusion chapter and it also briefly talks about the successive work on nanoparticle detection, including nanoparticle detection with microcavity lasers and detection of nanoparticles in water. It includes the collaborative efforts with Lina He and Woosung Kim for their effort on microcavity lasers detection (He et.al. 2011) and particle detection in water (Kim et.al. 2010).

Chapter 2

Whispering Gallery Microresonators

Whispering gallery mode (WGM) optical microresonators with ultra-high quality factors and microscale mode volumes are of interest for a variety of scientific disciplines ranging from fundamental to applied physics. Significantly enhanced light-matter interactions (Vahala 2003) make WGM resonators remarkably sensitive transducers for detecting perturbations in and around the resonator, e.g., virus/nanoparticle detection at single particle resolution (Vollmer and Arnold 2008, White, Oveys and Fan 2006, Zhu, et.al. 2010) and ultrasensitive detection of micromechanical displacement (Kippenberg et.al. 2005). Moreover, the mutual coupling of optical and mechanical modes mediated by enhanced radiation pressure within the microresonator provides a superb platform to study parametric oscillation instabilities and radiation pressure induced cooling of mechanical modes (Kippenberg and Vahala 2007). In addition, WGM microresonators with asymmetry (e.g., induced by structural deformations etc.) have been useful for investigating the correspondence between quasieigenstates and associated classical dynamics in mesoscopic systems (Lee et.al. 2009). Level crossing have been demonstrated in microtoroids by tuning the microtoroid aspect ratio (Carmon et.al. 2008).

2.1 Characterization of Microresonators

In this section the important aspects of microresonator and its characterization techniques are discussed. The theoretical equations describe the light field in the resonator is presented and simulations are discussed.

2.1.1 Types of Microresonators

In as WGM resonator, light field circulates around the circular periphery of a structure with near-ideal total internal reflection which enables extreme confinement of the field (Vahala 2003). WGM resonators come in various sizes and geometries with a common feature that there exists a curved boundary which refocuses the propagating field. The propagation of the resonant light field in a WGM resonator can be intuitively understood using the arguments of geometrical optics in which the rays of light reflects off the inner surface (Fig. 2.1a). Here we have considered a cylindrical resonator of radius R and refractive index n surrounded by an environment of refractive index 1. If the path taken by the WGM during a roundtrip within the resonator is a multiple of the wavelength λ of the WGM light field then a resonance occurs. Simply put, the resonance condition is given by $2\pi R n_{eff} = m\lambda$ where m is an integer mode number. n_{eff} is the effective mode index which is a value between n and 1. this is because in electromagnetic wave presentation of WGM, part of the propagating wave is outside of the resonator exposed in the medium (evanescent tail). Using finite element simulation, the mode profile is clearly revealed (Fig. 2.1b).

There exist a variety of WGM microresonators. They are generally categorized by their geometries Fig. 2.2. For example, the most popular microresonator is probably microspheres (Braginsky, Gorodetsky and Ilchenko 1989, Vahala 2003). They can be easily fabricated by melting the tip of a tapered fiber. A silica sphere is formed naturally by surface tension of the melted glass material. In recent years we have witnessed the invention of many new WGM microresonators. Micro-cylinder (White, Oveys and Fan 2006) and micro-bottle (Sumetsky 2004, Kipp et.al. 2006) can be fabricated by heating and pulling glass tubes while inflate the softened material with inert gas. Microring(Xu, Fattal and Beausoleil 2008), microdisk (Little and Chu
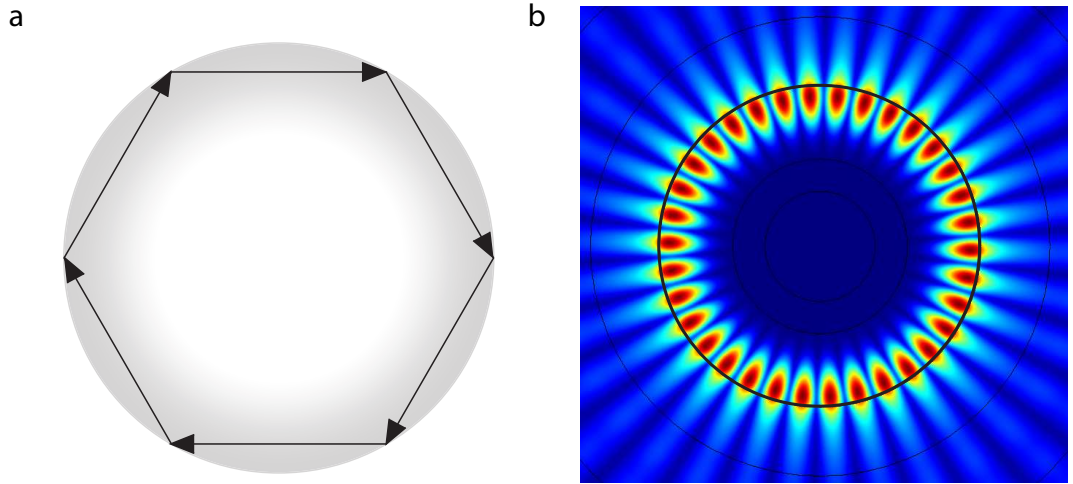
Figure 2.1: Illustration of WGM in a microresonator. **a,** Ray optics view. The light ray undergoes total internal reflections as it travels along the periphery of the resonator. **b,** Electromagnetic wave view. The WGM is distributed along the periphery in the resonator while part of the guided wave is outside the resonator consisting the evanescent tail.

1994) and microtoroid (D. K. Armani et.al. 2003) are fabricated on silicon chip by standard micro fabrication techniques, thus can be mass-produced. Crystalline WGM microresonator is fabricated by polishing crystal materials (e.g. CaF_2) (Grudinin, Ilchenko and Maleki 2006).

2.1.2 Quality Factor

The most important figure of merit for a WGM resonator is its quality factor (Q factor). It quantifies the resonator's optical quality and describes the its ability to confine light. The Q factor is defined as the ratio of energy stored in the resonator to the amount of dissipated energy per optical cycle:

$$Q = 2\pi \frac{EnergyStored}{EnergyDissipatedPerCycle} \tag{2.1}$$

Another derivative definition is:

$$Q = \frac{\omega}{\delta\omega} = \frac{\lambda}{\delta\lambda} \tag{2.2}$$
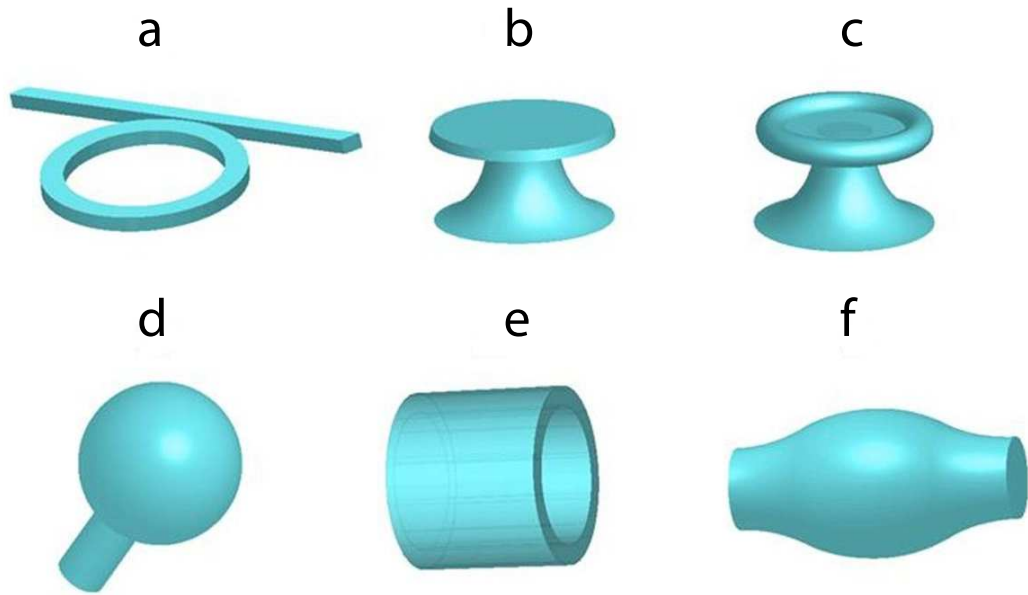
Figure 2.2: Illustrations of different WGM optical resonator genometries. **a,** waveguide coupled micro-ring, **b,** microdisk, **c,** microtoroid, **d,** microsphere, **e,** micro-cylinder, and **f,** bottle.

where $\delta\omega$ is an angular bandwidth of the resonance and $\delta\lambda$ is the bandwidth express in wavelength. For example, microspheres commonly have Q factors from 10^8 to 10^9, at a wavelength of $\lambda = 1.55\mu m$, the linewidth will be 15.5 fm when $Q = 10^8$. It also means a photon life time of $\tau = 82$ ns. Such a long photon life time allows light to circulate the resonator over 10^5 times before dissipated into the environment.

2.1.3 Fiber Taper

There are a number of methods to evanescently couple light into and out of these microresonators. For example, prism coupling (Otto 1968) and tapered fiber coupling (Knight 1997) are the two most studied method. Fiber taper, because of its high coupling efficiency, easy fabrication process and compactness, has gained popularity among researchers. A fiber taper is usually fabricated by thinning an commercial fiber down to a diameter of 1-3 μm. Techniques such as heating and pulling using hydrogen flame or CO_2 laser, buffer HF etching are used to reduce the taper thickness. Near 100% transmission can be obtained in a taper if fabricated carefully. Coupling to a microresonator is achieved by bringing the taper mode close to the WGM, evanescent

tails of the two optical modes overlaps and the energy in the taper is transferred into the WGM, and vice versa, the WGM can be coupled back to the taper allowing observing the resonance at the output end. The mode index of the taper mode and WGM mode has to be as close as possible, in other words, phase matching condition has to be maintained for efficient coupling.

2.1.4   Rate Equation

Denoting the taper mode as a_{in} and WGM as a, we can write the taper-resonator coupling equation:

$$\frac{\mathrm{d}a}{\mathrm{d}t} = -(i\omega_c + \frac{\kappa_0 + \kappa_1}{2})a - \sqrt{\kappa_1}a_{in} \tag{2.3}$$

where ω_c is the cavity resonance angular frequency, κ_0 is the intrinsic resonator damping rate and κ_1 is the mutual coupling rate between the fiber taper and the resonator. At steady state, the transmission of the taper-resonator system is given by:

$$T = \frac{|a_{in} + \sqrt{\kappa_1}a|^2}{|a_{in}|^2} = 1 - \frac{\kappa_0\kappa_1}{(\Delta\omega)^2 + (\frac{\kappa_0+\kappa_1}{2})^2} \tag{2.4}$$

where $\Delta\omega$ is the laser-cavity detuning. From Eq. 2.4 we can see that the resonance curve is in Lorentzian shape and the linewidth is given by $\kappa_0 + \kappa_1$. So that we can define the intrinsic and external Q factor as:

$$Q_0 = \frac{\omega_c}{\kappa_0}, \quad Q_{ext} = \frac{\omega_c}{\kappa_1} \tag{2.5}$$

Critical coupling is defined when $\kappa_1 = \kappa_0$. At this point, the transmission diminishes at the resonance point ($\Delta\omega = 0$), as seen in Eq. 2.4. In experiments, the transmission spectra of a resonator-taper system is acquired by sweeping a tunable laser across a resonance, while capture the transmitted power by a photo-detector.
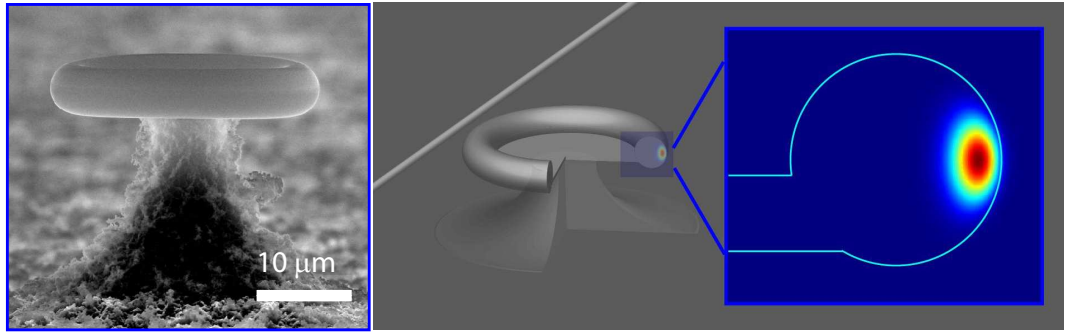
Figure 2.3: SEM pictures of a microtorid (left). The right panel shows the crosssection of a microtoroid and its optical mode.

2.2 Microtoroid

The microresonator we use in this dissertation is microtorid (Fig. 2.3. It is fabricated using standard photolithography, XeF_2 etching and CO_2 laser reflow (D. K. Armani et.al. 2003). These on-chip resonators have very high Q factor $> 10^8$ and a small mode (volume $< 200 \mu m^3$ for a 40 μm diameter microtoroid). This enables one of strongest light-matter interactions among all types of microresonator. As a result, microtorid has been used to studied various non-linear phenomena including simulated Raman scattering, parametric oscillation, four-wave-mixing and frequency up-conversion. It has also been used to create microcavity lasers (rare-earth ion doped or Raman)(Yang et.al. 2005, Kippenberg et.al. 2005). Recently it is found that it is relatively easy to excite the mechanical modes through radiation pressure in microtoroids, which makes it an ideal platform to study meso-scale opto-mechanics (Kippenberg et.al. 2005). Microtoroid is also a great sensor, thanks to its Q factor and small size.

2.3 Opto-Thermal Properties of Microtorid

Because of its high Q factor, the circulating optical power insider a microtorid is usually very strong. The minor absorption coefficient of silica material cannot be neglected. During strong pumping on resonance, the cavity will be heated and hence its resonance wavelength is shifted (Carmon, Yang and Vahala 2004). Temperature of the cavity mode volume can rise over tens of degrees Celsius with a few mW of
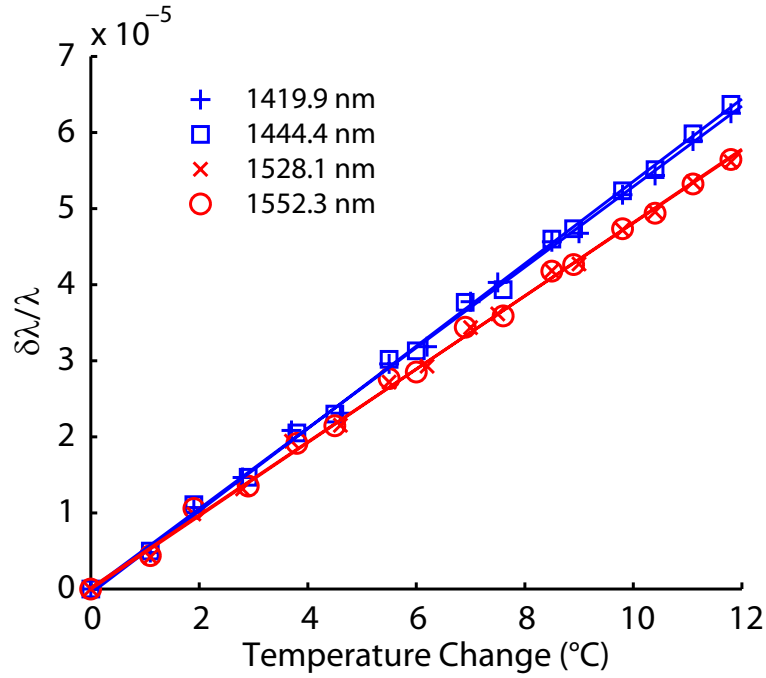
Figure 2.4: Changes in the resonance wavelengths of different WGMs in a microtoroid as a function of temperature changes. Lines are linear fits.

power input. Fig. 2.4 gives an example showing the change of resonance wavelength when the cavity temperature is raised. For different modes, since they have different spatial distribution, the percentage of the mode volume that is in silica and in air are different. This in turn gives different modes different effective mode index. Therefore they may have different response on resonance shift upon temperature change (Fig. 2.4).

The on-resonance optical heating is also greatly affected by the geometry of the microtoroid. This is due to the change of heat dissipation ability for different disk and pillar sizes. Much more heat is dissipated through the disk structure and the supporting silicon pillar then through air convection. Thus if the toroid ring is closer to the pillar, heat can be conducted faster. This principle is verified by the measurements in Fig 2.5. By tailoring the geometries of microtorids, one can enhance or reduce the opto-thermal effects. For example when observing the transmission spectrum of a microtoroid, a relatively larger pillar is preferred to minimize the resonance lineshape deformation caused by opto-thermal heating.
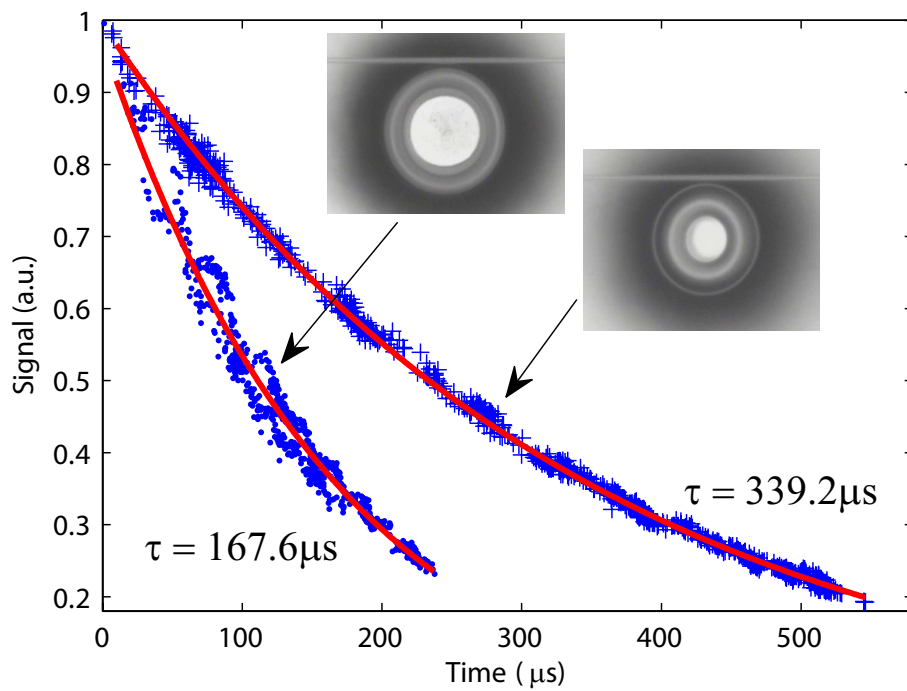
Figure 2.5: Measurement of thermal relaxation time constant for two microtoroids geometries. Larger pillar allows quicker dissipation of heat inside a microtoroid, thus gives a shorter thermal relaxation time constant.
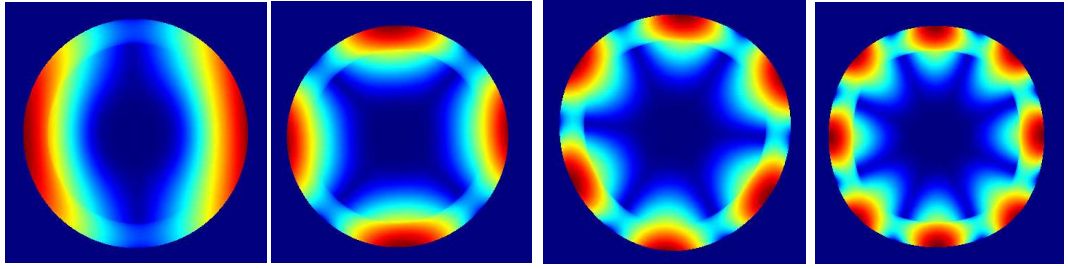
Figure 2.6: Finite element simulations showing 1th to 4th order flapping mode in a microtoroid. False color shows the mechanical displacement.
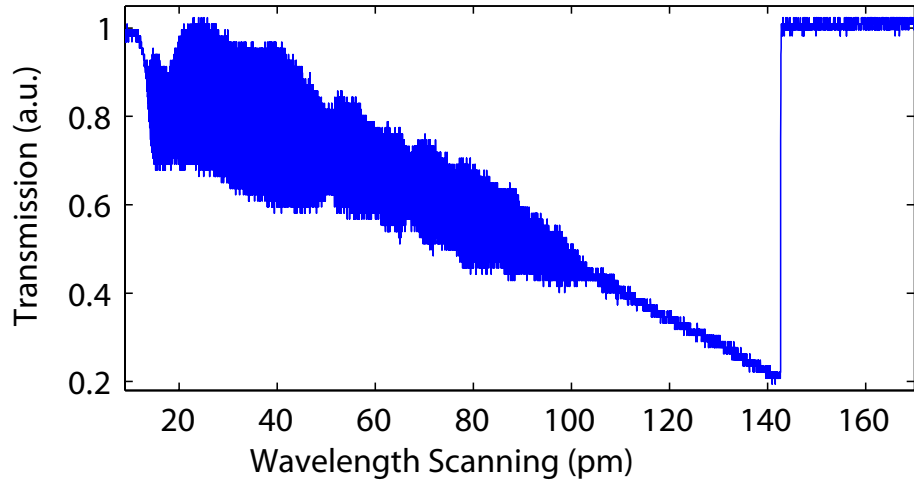
Figure 2.7: Finite element simulations showing 1th to 4th order flapping mode in a microtoroid. False color shows the mechanical displacement.

2.4 Mechanical Properties of Microtoroid

Although Silica is a rigid material in macroscale, under strong on-resonance pumping, the radiation force exerted on the toroid ring may cause the $2\mu m$ thin disk structure to deform. As a result various mechanical modes can be excited through photon-phonon energy transfer (Kippenberg and Vahala 2007). These mechanical modes typically have frequency ranging from a few MHz to hundreds of MHz. Figure 2.6 shows examples of mechanical modes in a microtoroid.

On the transmission spectra, mechanical modes manifest themselves as high frequency noise (Fig. 2.7) whose frequency coincides with the frequency of mechanical vibration.

The triangular shape in Fig. 2.7 is due to opto-thermal heating induced wavelength red-shift (Carmon, Yang and Vahala 2004).

2.5 Microtoroid as Environmental Sensors

Enhanced light-matter interaction make microtoroids excellent sensors. The resonance condition is very sensitive to environmental perturbations such as temperature, refractive index and scattering centers. Sensing signal is usually extracted from resonance wavelength shift or linewdith change. In this section we show a few simple examples.

2.5.1 Temperature Sensor

In the last section we have shown that the resonance wavelength shifts upon temperature change. This mechanism can be used to make extremely sensitive temperature sensor. From Fig. 2.4 we know that the temperature response is about $5 \times 10^{-6} K^{-1}$ for $\Delta\lambda/\lambda$. Given a resonator with Q factor of 10^8 and considering a resonance shift of 1/20 of its linewidth detectable, it will have a minimal temperature sensitivity of:

$$\Delta T = \frac{1}{10^8 \times 20} \times \frac{1}{5 \times 10^{-6}} = 10^{-4} K \tag{2.6}$$

Considering the small size of a microtoroid, it has the potential to precisely measure local temperature changes.

2.5.2 Humidity Sensor

Normally silica material is not very sensitive to humidity changes. For microtoroid, its Q factor can stays around 10^8 until 90% relative humidity and its resonance wavelength is not sensitive to humidity change, either. Therefore to measure humidity
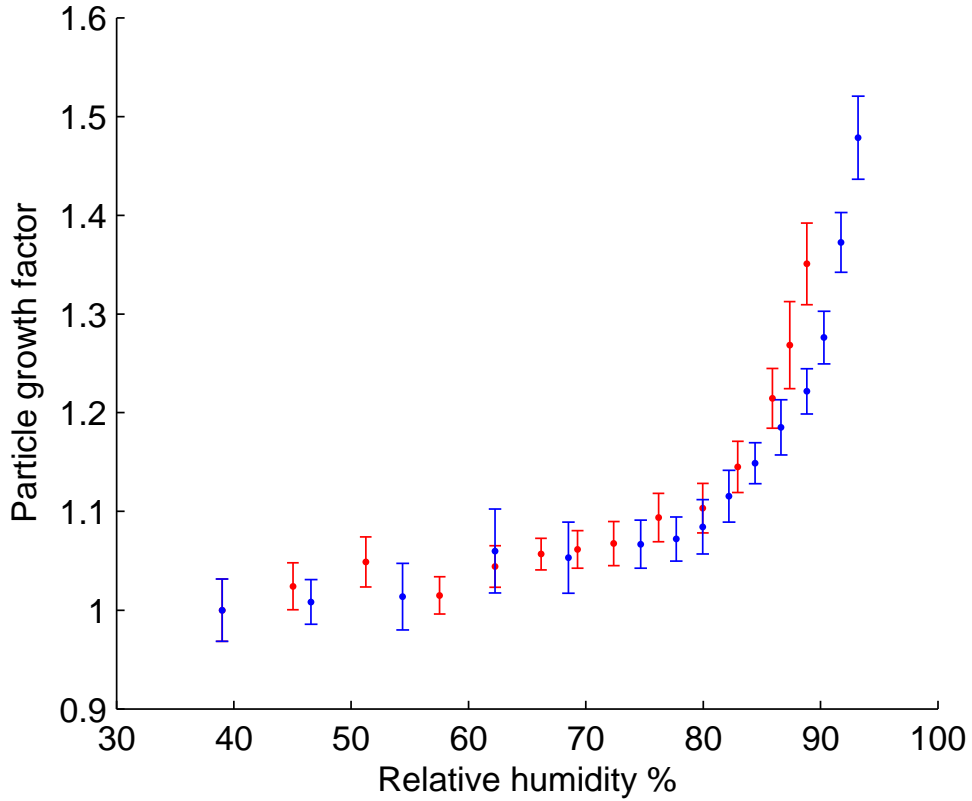
Figure 2.8: Relations of sugar particle size growth factor measured on a microtoroid with respect to relative humidity change. The blue and red data points are taken when humidity is increasing and decreasing, respectively.

below 90%, the microtoroid has to be modified with humidity sensitive material. For example, one can coat the resonator with humidity sensitive polymer whose refractive index changes with humidity. By monitoring the resonance wavelength shift one can effectively map it to humidity change.

In our initial test, we took a different approach. We deposited sugar nanoparticles on a microtoroid. Sugar particle is known to have deliquescence properties which makes their sizes gradually increase when humidity rises. Using the particle size measurement techniques describing in Chapter 3 and 4, by measuring the size change of sugar particles, we can monitor the humidity changes. Fig. 2.8 shows the measured sugar particle size factor versus relative humidity. With sugar particle, we can effectively measure humidity above 70%. To cover the range below 70%, one may use other salt particle materials which have transitions at a lower relative humidity.

14

2.5.3 Refractive Index Sensor

Refractometric sensor can be made from microresonators by simply immersing the resonator into the liquid of interest. Due to the evanescent tail exposed in the surrounding medium, the WGM index changes with the refractive index of the medium and hence the resonance wavelength shifts which can be monitored. The WGM extends outside the resonator further in liquid than in air because the reduced refractive index contrast between the resonator and medium materials. The sensitivity of this scheme can reach 10^{-8} RIU for ultra-high-Q microresonators (Hanumegowda et.al. 2005). It can be used to detect tiny amount of chemicals in liquid (e.g. alcohol in water). The main difficulty for these sensors is to maintain the high Q factor in the aqueous solutions, as micro-sized particulate contaminations can easily decreases the Q factor to below 10^4.

Chapter 3

Single Scatterer Induced Mode Splitting

[1]Mode splitting phenomenon has been constantly observed in ultra-high-Q microresonators. A single resonance mode splits into doublet in the presence of coupling between the clockwise (CW) and conter-clockwise (CCW) travelling-wave modes (Weiss et.al. 1995, Kippenberg, Spillane and Vahala 2002, Mazzei et. al. 2007). This coupling lifts the natural 2-fold degeneracy in circular resonators. Scattering centers in the mode volume has the ability to scatter a fraction of energy into the opposite direction propagating mode, and therefore creating the coupling between CW and CCW modes.

In this Chapter, single nanoparticles are used as the agent to induce mode splitting. Their ability to scatter light is directly captured in the subsequent mode splitting spectrum. This study reveals that the polarizability of a nanoparticle can be calculated from the mode splitting spectrum (Mazzei et. al. 2007), and the particle size can be estimated if it's refractive index is known, or vice versa (Zhu et. al. 2010).

---

[1]Part of this section has appeared in "On-chip single nanoparticle detection and sizing by mode splitting in an ultrahigh-Q microresonator", Nature Photonics, vol. 4, pp. 46-49, 2010.

3.1 Back-scattering and Mode Splitting

Ideally modal coupling does not exist in pure circular silica microresonators, however due to minor contaminations on the resonator surface, structure defects or material inhomogeneity, back-scattering can be created in a resonator. This category of mode splitting is normally called intrinsic splitting (Weiss et.al. 1995, Gorodetsky, Pryamikov and Ilchenko 2000). It is more frequently observable in the microtoroids with smaller major and minor diameters and Q factors above 100 million (Kippenberg, Spillane and Vahala 2002). The signature of this type of mode splitting is that the split modes have very similar linewidth and the separation between them is relatively large comparing with their linewidths (usually > 10). But overall the intrinsic splitting is small and normally does not exceed $2/10^7$ of laser frequency.

We are more interested in another type of mode splitting, in which the modal coupling is induced by a single Rayleigh Scatterer. This Scatterer can be a subwavelength particle or a fiber tip. To simplify the study of the scatterer's light scattering properties, we prefer to choose microtoroid modes without observable intrinsic splitting (the resonance mode appears as a single peak). However, we believe there is always some amount of intrinsic splitting in a resonance, since scattering from the silica material or the surrounding medium is inevitable. But this tiny amount of splitting may not be visible if the amount of splitting is much smaller than linewidth of the resonance. In this case we can neglect it.

3.1.1 Single Rayleigh Scatterer

The mechanism responsible for single-particle induced mode splitting can be intuitively explained as follows. A Rayleigh (Radius $R \ll \lambda$) nanoparticle in the evanescent field of WGMs acts as a scatterer. A portion of the scattered light is lost to the environment creating an additional damping channel (with coefficient Γ_R), while the rest (with coefficient g) couples back into the opposite propagating mode and induces coupling between the counter-propagating WGMs (Fig. 3.1), whose 2-fold degeneracy is lifted consequently (Mazzei et. al. 2007, Arnold et. al. 2003).
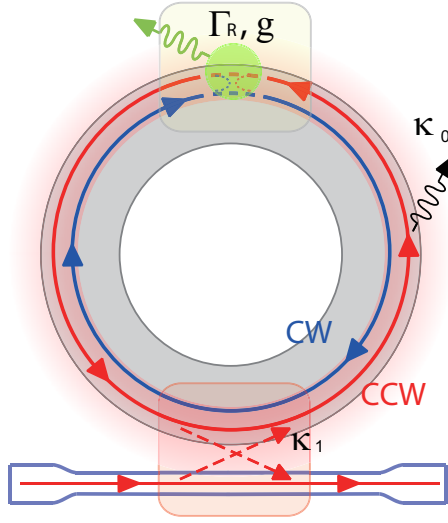
Figure 3.1: Illustration of the coupled nanoparticle-microtoroid system. κ_1: microtoroid-taper coupling rate, κ_0: intrinsic damping rate (material and radiation losses), g: coupling coefficients of the light scattered into the resonator, and Γ_R: additional damping rate due to scattering loss.

The superposition of CW and CCW modes give rise to two standing-wave-modes (SWMs) (or Eigen modes) that are split in frequency as manifested by the doublet in transmission spectrum (Fig 3.2). The SWMs redistribute themselves according to the scatterer's location: The symmetric mode (SM) locates the particle at the anti-node (mode maxima) while the asymmetric mode (ASM) locates it at the node (mode minnima). The underlying physical mechanism can be intuitively understood from the Fermat's principal, which states that rays of light traverse the path of stationary (could be maximal or minimal) time (Zhu et.al. 2010). Since the system is rotational symmetric except for the symmetry breaking particle, when the SWMs try to arrange (rotate) themselves in the system, the particle is the only strong reference. SM takes the maximal (when the refractive index of particle is larger than that of surroundings) and ASM takes the minimal. Consequently, SM experiences significant frequency shift due to the refractive index difference between the particle and the surroundings and linewidth broadening due to the additional damping channel by the particle scattering.

Finite element simulations are used to study this phenomenon. Two Dimensional resonator model is created in Comsol Multiphysics. The resonator area is set to have a refractive index of 1.45 and the surroundings to have refractive index of 1.
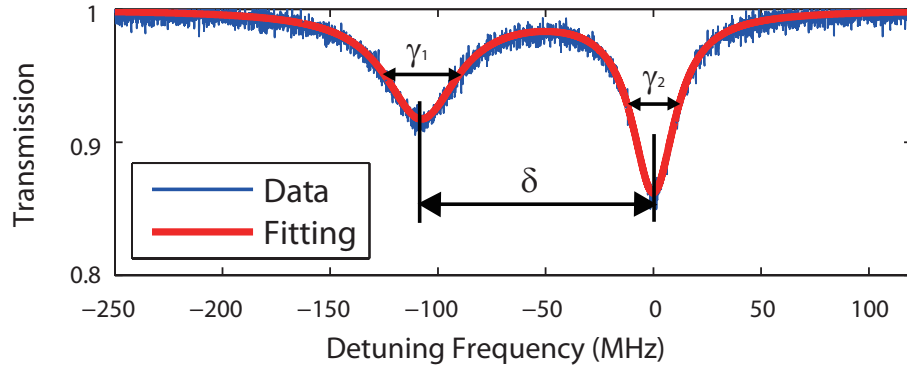
Figure 3.2: Experimentally obtained transmission spectrum (blue) after the deposition of a single nanoparticle and the curve fitting (red). Mode splitting is significant if $2\delta > \gamma_1 + \gamma_2$ is satisfied.
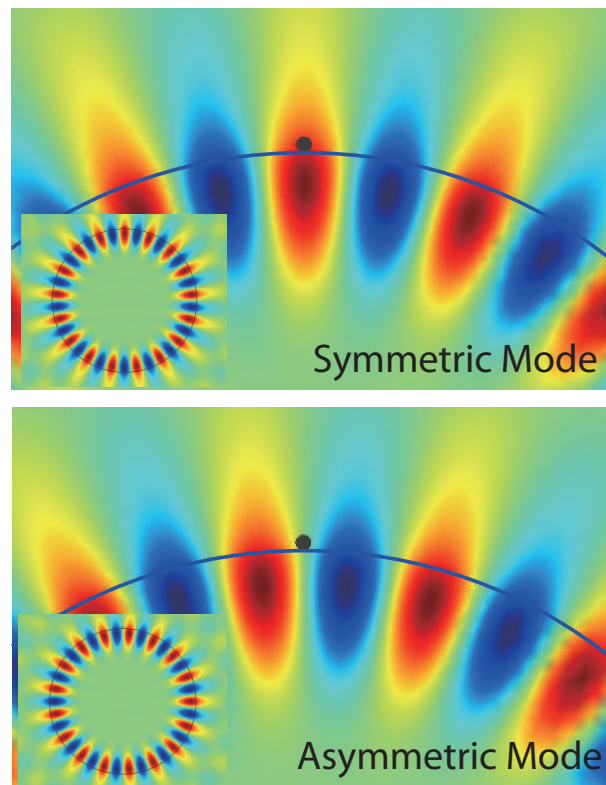
Figure 3.3: Field distribution of symmetric (SM) and asymmetric modes (ASM) relative to the position of the nanoparticle using finite-element-method simulation. Insets show the mode along the periphery of the resonator.

Eigen modes are searched around a resonance wavelength and their wavelength and linewidth can be calculated precisely in the software. In the model a subwavelength particle with refractive index of 1.5 is added on the surface of the resonator, and pairs of Eigen modes are found in the solutions. As expected, the pairs of Eigen modes represent the doublet in mode splitting (SM and ASM), and they distribute according to the location of the particle. The SM and ASM distributions are depicted in Fig. 3.3.

The particle induced frequency shift and linewidth damping on the SM is also studied in the simulation. The particle size is varied and the corresponding resonance frequency and linewidth of SM and ASM is plotted in Fig. 3.4 and 3.5.

The frequency and linewith of the SM is found to vary significant when the size of particle is changed. As seen in Fig. 3.4, linear relation exists between the frequency shift of the SM and particle size square (R^2). In addition, Fig. 3.5 shows the linewidth broadening of the SM changes proportionally with the particle size to the power of 4 (R^4).

3.1.2 Rate Equations

A perfect azimuthally symmetric microresonator supports two counter-propagating WGMs (CW and CCW) with the degenerate resonant angular frequency ω_c and the same normalized field distribution function $f(\mathbf{r})$, where $\mathbf{r}$ denotes any point in the mode volume (can be inside microtoroid or outside in the evanescent field).

In the presence of a scatterer, one of the modes, e.g., CW, couples to the scatterer. The scattered light couples back to either the CW or the CCW mode. The same is true when the CCW couples to the scatterer. We assume the coefficient g for all of these coupling processes. For a Rayleigh scatterer, the interaction between the WGM and the scatterer can be modeled using the dipole approximation (Jackson 1962) where a dipole is induced in the scatterer by the electric field of the coupled WGM. The coupling coefficients are given as (Mazzei et. al. 2007):
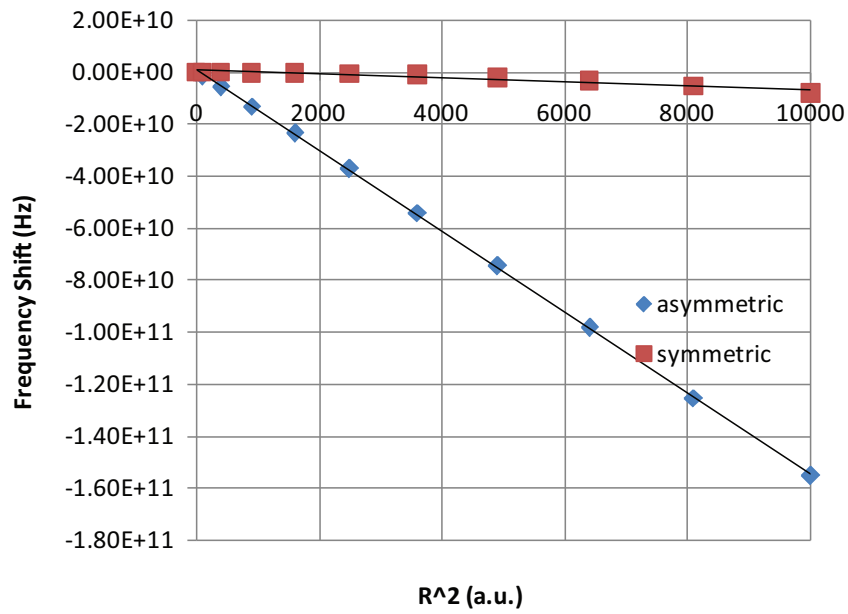
Figure 3.4: Finite element simulation results of the frequency of split modes versus the particle size square (R^2). It shows a linear relation between the frequency shift of the symmetric mode and R^2, while the frequency of the asymmetric mode does not change significantly.
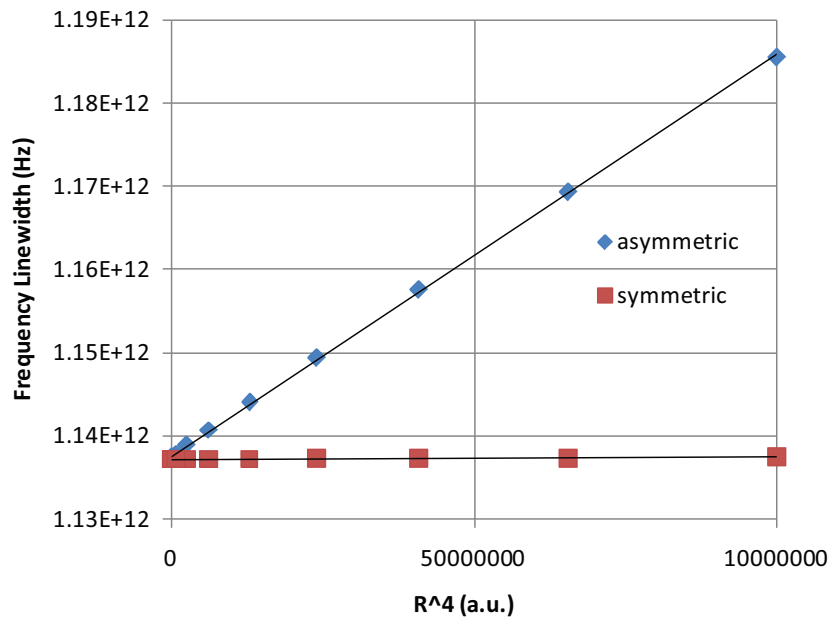
Figure 3.5: Finite element simulation results of the linewidth of split modes versus the particle size to the power of 4 (R^4). It shows the linear relation between the linewidth of the symmetric mode and R^4, while the linewidth of the asymmetric mode does not change significantly.

$$g = -\frac{\alpha f^2(\mathbf{r})\omega_c}{2V} \tag{3.1}$$

where $f^2(\mathbf{r})$ accounts for the cavity mode functions of the CW and CCW modes and V denotes the normalized mode volumes of the WGM. α is the polarizability of the scatterer which for a spherical scatterer of radius R can be expressed as $\alpha = 4\pi R^3(\epsilon_p - \epsilon_m)/(\epsilon_p + 2\epsilon_m)$ where ϵ_p and ϵ_m denote electric permittivities of the particle (scatterer) and the surrounding medium, respectively. Damping rates due to coupling to the reservoir via Rayleigh scattering can be derived as (Mazzei et. al. 2007):

$$\Gamma_R = \frac{\alpha^2 f^2(\mathbf{r})\omega_c^4}{6\pi\nu^3 V} \tag{3.2}$$

where $\nu = c/\sqrt{\epsilon_m}$, and c is the speed of light in vacuum. Then the rate equations of the fiber coupled microresonator-scatterer system can be written as:

$$\frac{\mathrm{d}a_{CW}}{\mathrm{d}t} = -[i(\omega_c + g) + \frac{\Gamma_R + \kappa_0 + \kappa_1}{2}]a_{CW} - (ig + \frac{\Gamma_R}{2})a_{CCW} - \sqrt{\kappa_1}a_{CW}^{in} \tag{3.3}$$

$$\frac{\mathrm{d}a_{CCW}}{\mathrm{d}t} = -[i(\omega_c + g) + \frac{\Gamma_R + \kappa_0 + \kappa_1}{2}]a_{CCW} - (ig + \frac{\Gamma_R}{2})a_{CW} - \sqrt{\kappa_1}a_{CCW}^{in} \tag{3.4}$$

where $\kappa_0 = \omega_c/Q_0$ denotes the intrinsic damping due to material and radiation losses, and $\kappa_1 = \omega_c/Q_{ext}$ is the fibre taper-resonator coupling rates with Q_0 and Q_{ext} being the intrinsic and external quality factors, respectively. Defining the normal modes of the resonator as $a\pm = (a_{CW} \pm a_{CCW})/\sqrt{2}$ and that of the input modes as $a_{\pm}^{in} = (a_{CW}^{in} \pm a_{CCW}^{in})/\sqrt{2}$, we find that in steady-state regime normal modes can be expressed as:

$$(-i(\Delta - 2g) + \frac{\kappa_0 + \kappa_1 + 2\Gamma_R}{2})a_+ + \sqrt{\kappa_1}a_+^{in} = 0 \tag{3.5}$$

$$(-i\Delta + \frac{\kappa_0 + \kappa_1}{2}]a_- + \sqrt{\kappa_1}a_-^{in} = 0 \qquad (3.6)$$

where $\Delta = \omega - \omega_c$ denotes the lase-cavity detuning. It is clear that the symmetric SWM $(+)$ has a detuning of $2g$ from the degenerate WGM, and its damping rate is given as $\kappa_0 + \kappa_1 + 2\Gamma_R$. The asymmetric SWM $(-)$ is not affected by the Rayleigh scatterer. In the absence of CCW input, i.e., $a_{CCW}^{in} = 0$, we can write the transmission and reflection coefficient of the coupled system as:

$$t = 1 - \frac{\kappa_1\beta}{\beta^2 - (ig + \Gamma_R/2)^2} \qquad (3.7)$$

$$r = \frac{\kappa_1(ig + \Gamma_R/2)}{\beta^2 - (ig + \Gamma_R/2)^2} \qquad (3.8)$$

where $\beta = -i\Delta + ig + (\kappa_0 + \kappa_1 + 2\Gamma_R)/2$, and the input output relation of the fiber taper coupled resonator system is given as $a_{CW}^{out} = a_{CW}^{in} + \sqrt{\kappa_1}a_{CW}$.

Note that the finite-element simulation results in the previous subsection agrees well with the theory there. In 2 dimensional case, the polarizability of a particle is proportional to R^2. Therefore, the frequency shift of SM scales with R^2 and linewidth broadening scales with R^4.

3.1.3 Nanoparticle Size Estimation

The mode splitting observed in the transmission spectrum can be utilized to estimate the size of Rayleigh scatterer. Assuming that the surrounding medium is air, from Eqs. 3.1 and 3.2 we find $\Gamma_R/g = 8\pi^2\alpha/3\lambda^3$ where λ is the resonance wavelength before splitting. Then $\alpha = 3(\Gamma_R/g)\lambda^3/(8\pi^2)$, which implies that polarizability of the particle can be calculated from the measured values of g and Γ_R. Subsequently, nanoparticle size can be accurately estimated provided that its refractive index is known. Figure 3.2 shows a typical transmission spectrum with a double Lorentzian resonance captured by an oscilloscope. We extract g and Γ_R by fitting a double Lorentzian function expressed as:

$$f(\omega) = 1 - \frac{A_1\gamma_1^2/4}{(\omega - \omega_1)^2 + \gamma_1^2/4} - \frac{A_2\gamma_2^2/4}{(\omega - \omega_2)^2 + \gamma_2^2/4} \tag{3.9}$$

to the acquired transmission spectrum. In Eq. 3.9, ω_1, and ω_2 denote the locations of resonance dips, γ_1 and γ_2 designate the linewidths of these resonances, and A_1 and A_2 correspond to the relative depths of the resonances.

During the fitting process, the parameters in Eq. 3.9 are varied until the best fit is obtained by minimizing mean square error. The amount of splitting is calculated from $\delta = |\omega_1 - \omega_2|$ and equated to the coupling coefficient as $2g = \delta$. The values of γ_1 and γ_2 are used to obtain additional damping parameter using $2\Gamma_R = \gamma_1 - \gamma_2$. Then we find

$$\alpha = 4\pi R^3 \frac{n_p^2 - 1}{n_p^2 + 2} = \frac{3\lambda^3}{8\pi^2} \frac{\gamma_1 - \gamma_2}{\delta} \tag{3.10}$$

where n_p denotes the refractive index of the particle. Consequently the particle radius R is given by

$$R = [\frac{(3\lambda^3/8\pi^2)(\gamma_1 - \gamma_2)/\delta}{4\pi(n_p^2 - 1)/(n_p^2 + 2)}]^{\frac{1}{3}} \tag{3.11}$$

3.2 Single Nanoparticle Detection and Sizing

In principle, one can use different resonance modes of a microtoroid resonator to estimate the size of deposited particle. In our single particle sizing experiments, we observed that although splitting for different resonance modes in a microtoroid were different, there was no significant difference in $(\gamma_1 - \gamma_2)/\delta$ which is used to determine the particle size. This is, indeed, a proof that sizing can be done without the information of particle-mode overlap $f(\mathbf{r})$. Due to this observation, we used
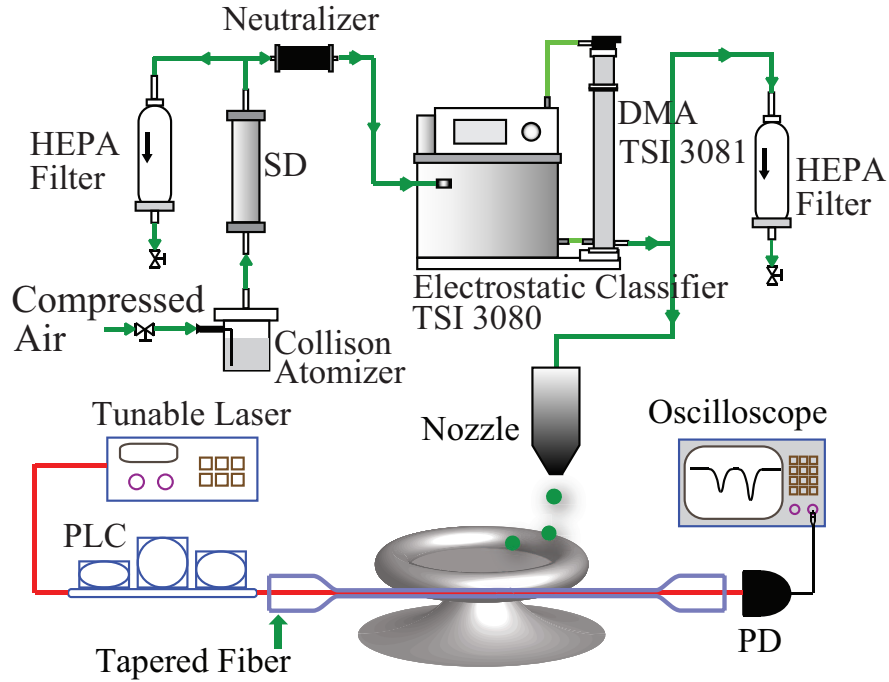
Figure 3.6: Schematic of the experimental set-up for particle detection. The experimental set-up consists of a differential mobility analyzer (DMA) system for size classification of nanoparticles, a nozzle for depositing nanoparticles onto the microtoroid, and a taper-fibre coupled resonator system. PLC: Polarization controller, PD: Photodetector, SD: Silica gel desiccant dryer, DMA: Differential mobility analyzer.

the transmission spectrum of one resonance to estimate the particle size. Moreover, real-time measurement benefits from focusing on one resonance mode.

A schematic illustration of our apparatus for the generation of monodisperse nanoparticles and their deposition on the microtoroid resonator is presented in Fig. 3.6.

In order to couple light from a tunable laser into and out of the microtoroid resonators, taper-fibres (Cai, Painter and Vahala 2000, Spillane et.al. 2003) were fabricated by pulling single mode fibres heated by a hydrogen (H_2) flame. Position of the microtoroid is finely controlled by a piezo stage to adjust the air gap between the taper and microtoroid. During the experiments, two tunable lasers in the 670 nm and 1450 nm wavelength bands were used. Their wavelengths were linearly scanned around the resonance wavelength of the microtoroid. The real-time transmission spectra were obtained by a photodetector followed by an oscilloscope. This enabled a real time monitoring of the transmission spectra on the oscilloscope. In order to eliminate the

observable effects of thermal nonlinearity (Carmon, Yang and Vahala 2004, Schmidt et.al. 2008) on the ultra-high-Q microtoroid due to heat build-up in the resonator, wavelength scanning speeds and powers of both tunable lasers were optimized. Typical operating conditions for scanning speed and laser power were 40 nm/s and 15 μW, respectively.

3.2.1 Nanoparticle Delivery

We used potassium chloride (KCl) and polystyrene (PS) microspheres (Thermo Scientific, 3000 series, radii range 30-175 nm) in mode splitting and subsequent particle detection and sizing experiments. Polydisperse droplets are carried out by compressed air using a Collison atomizer. The solvent in droplets is then evaporated in the dryer with the silica gel desiccant. Solid particles are further neutralized by a Po^{210} radioactive source such that they have a well-defined charge distribution. Particles are sent to a DMA where they are classified according to their electrical mobility (Liu and Pui 1974) (Fig. 3.6). Thus, particles within a narrow range of mobility can exit through the output slit of the DMA. The flow rate is controlled and the ratio of particle flow rate to the sheath flow (particle-free air flow) rate was set to 1:10. The resulting monodisperse particle flow has a concentration of about $10^5/cm^3$ and a geometrical standard size deviation of approximately 5% (Knutson and Whitby 1975).

A stainless steel nozzle with a tip inner diameter of 80 μm was placed at about 200 μm above the microtoroid to deliver nanoparticles to its mode volume (Figs. 3.7 and 3.8). In later experiments, a different nozzle fabricated by pulling glass capillary above a hydrogen flame is also used. The flow rate at the nozzle was 0.02 cm^3/s. In order to force the particle's trajectory towards the microtoroid, a metal sheet connected to a -400V source was placed under the silicon chip to exert an electrical field on the particle. But later we found that this is not necessary. When a particle reaches the microtoroid and adsorbed on its surface, the interaction of the WGM with the particle and re-distribution of the resonator field due to the scattering from the particle leads to a mode splitting which could be observed in the transmission spectrum. Under the operation conditions given above, we observed one mode splitting corresponding to one particle binding event in every 5s, on average. Thus the overall capture efficiency of particles to the sensing area of our system is
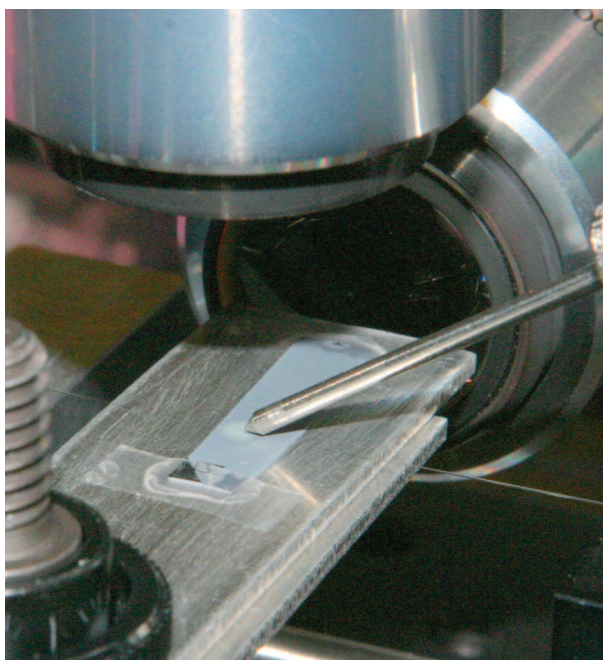
Figure 3.7: Camera image showing the microtoroid and the stainless steel nozzle used to deposit nanoparticles. The inner diameter of the nozzle is about 80 μm, while the outter shape of the nozzle is conical and is much larger. In later experiments, a different nozzle fabricated by pulling glass capillary above a hydrogen flame is also used.

Figure 3.8: Microscopic image showing the microtoroid and the nozzle used to deposit nanoparticles.

estimated as $10^5 cm^{-3} \times 0.02 cm^3/s \times 0.2s^{-1} = 0.01\%$ This low efficiency is due to the fact that most particles bounce off the smooth resonator surface. It could be improved by a better design of the nozzle system for controlling particle dynamics. The particle-microtoroid binding events are described by a Poisson process. In these experiments, the particle concentration was very low so that the average time interval between two events was longer than 10-15 seconds. This allowed us to shut off the aerosol flow immediately after a mode splitting was observed in the transmission spectrum and ensures that one and only one particle is adsorbed in the mode volume of the microtoroid. The particles deposited outside the mode volume on the microtoroid do not affect the WGM, so they have no effect on the resonance spectrum. To investigate the bonding between the nanoparticle and microtoroid, we kept the microtoroids with adsorbed nanoparticles in a gel-box for two weeks and didn't see any noticeable change in the resonance spectrum. This suggests that particle attachment to the microtoroid is stable under room conditions.

To utilize the particle sensing strategy carried out in this study, the microtoroid cavity needs to be cleaned upon the completion of detecting a single particle. To remove submicron particles from semiconductor surfaces, several cleaning techniques, which can also be used to remove particles from microtoroid surface, have been developed.

Hydrophilic or water (solvent)-soluble particles can be removed by simply condensing water vapor on the surface of microtoroids and then by drying the surface with dry air or nitrogen. This is the technique we used in our study to remove KCl particles from the microtoroid surface. The cleaning step took less than a second. The microcavity can be reused immediately after the cleaning.

For hydrophobic or insoluble particles several cleaning techniques (or their combination) have been developed: (1) Steam laser cleaning (Heroux et.al. 1996, Leiderer et.al. 2000): The technique makes use of a thin liquid film which is condensed onto the surface (by vapor condensation) before a laser pulse is fired. The laser rapidly heat up the liquid film to create bubble nucleation at the solid/liquid interface and the subsequent explosive vaporization of the liquid removes particles. One can also use alternative heating sources such as focused white light. (2) The cleaning technique by a high-speed mixture of steam and purified water droplets has been utilized to remove sub-micrometer particles from semiconductor surfaces (Watanabe et.al. 2009).

This technique removes fine particles without using any chemicals. We can apply this cleaning technique to remove submicron particles from our micro-cavity surfaces by injecting the mixture through micro-jet nozzles. (3) High velocity aerosol cleaning using ultrapure water or dilute aqueous solutions (e.g. dilute ammonia) is also very common in semiconductor IC fabrication. The combination of droplet impact forces with continuous liquid flow improves the cleaning efficiency for sub-100nm particles. (4) Particle cleaning can be accomplished by impinging solid argon or nitrogen aerosol (or CO_2 aerosol) upon the surface to be cleaned (McDermott et.al. 1994, Banerjee and Campbell 2005). The evaporated aerosol is removed by venting along with the particles dislodged. (5) Dry laser cleaning process has also been used to remove submicron particles from semiconductor surfaces (Leiderer et.al. 2000, Lu et.al. 1997, Song et.al. 2002). The technique removes particles by irradiating the surface with a short laser pulse. The strong acceleration at the surface due to thermal expansion leads to inertia forces strong enough to overcome the particle-surface adhesion force.

3.2.2 Single Particle Detection and Sizing

Before particle attachment, the transmission of a microtoroid shows a single Lorentzian resonance. After the first nanoparticle is deposited, SWMs are formed and the 2-fold degeneracy is lifted, which is confirmed by the double resonances in the spectra. Consecutive particle depositions lead to changes in both the splitting and the linewidths of the resonances. Fig. 3.9 shows the corresponding resonance spectra change when particles are deposited. The optical image of the microtoroid also confirms the number of particles. The changes in spectra are discrete, indicating the adsorption of particle to silica resonator surface is instantaneous ($< 0.1s$ which is the frame capture time of the spectra).

Fig. 3.10 shows the amount of mode splitting changes with the number of particles adsorbed onto the microtoroid. Note that in these data, different microtoroids are used, but they are on the same chip and having very similar sizes and resonance characteristics. As seen in fig. 3.10, larger particles lead to more significant changes in the amount of splitting, which is expected since they have stronger light scattering ability (or polarizability). Given enough data, one could use the statistics of splitting change to estimate the average size of particle ensemble.
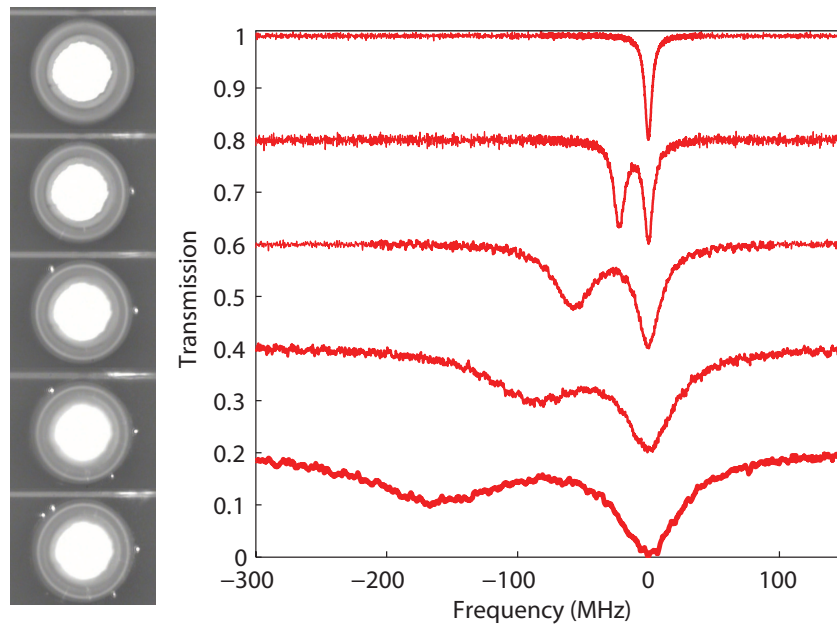
Figure 3.9: Transmission spectra and the amount of splitting versus number of deposited particles. Series of normalized transmission spectra taken at 1550 nm wavelength band and the corresponding optical images (particle scattering visible, assisted by a visible light laser) recorded for four consecutive depositions of KCl nanoparticles. The spectra are vertically shifted for clarity.
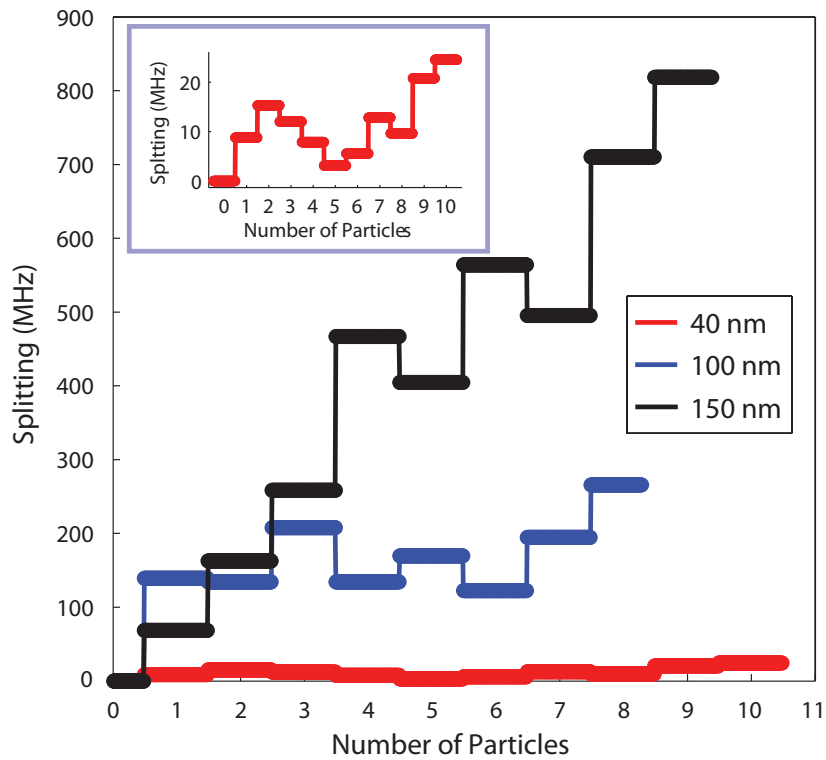
Figure 3.10: Normalized splitting $2g/\omega_c$ versus particle number for KCl nanoparticles of different sizes. Each discrete step (lines are drawn for eye guide) corresponds to a single nanoparticle binding event. The inset shows the an enlarged plot for nanoparticles of R=40 nm. $2g$: splitting frequency, and ω_c: resonance frequency.
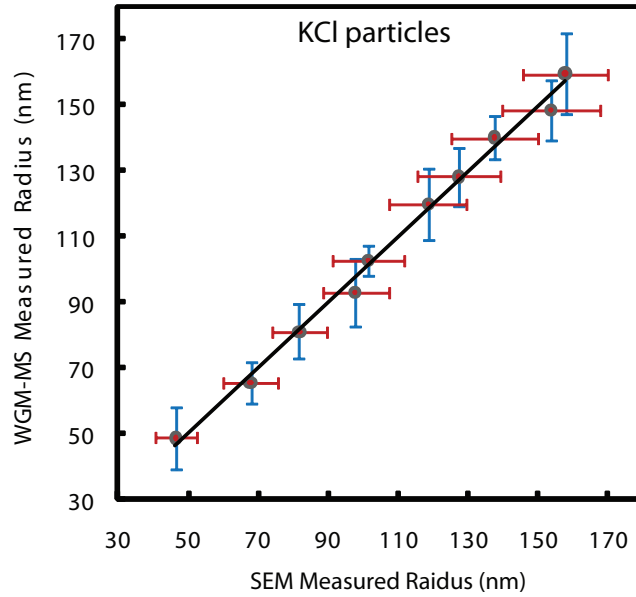
Figure 3.11: Single KCl particle sizing using mode splitting in a microtoroid resonator. Estimated sizes of particles as a function of their actual sizes are shown. Error bars denote the standard deviations of size distributions.

Equation 3.11 indicate that we can calculate the size of the first particle adsorbed onto the resonator, from the mode splitting spectra. We tested this method using particles of different sizes and materials, including KCl and PS microspheres. Note that Eq. 3.11 applies to spherical particles. The shape of KCl particles are irregular (between cubic and spherical). Eq. 3.11 is still a good approximation for KCl particles.

Figure 3.11 and 3.12 give the particle size measurement results. The nominal KCl particle sizes are taken by measuring over 100 particles under SEM for each size and we use the nominal PS particle sizes provided by the manufacturer. For both materials, the average measured sizes using mode splitting method agrees very well with the nominal values. KCl particles sizing yield much larger standard deviations than PS. It is mostly attributed to the their non-spherical shapes.
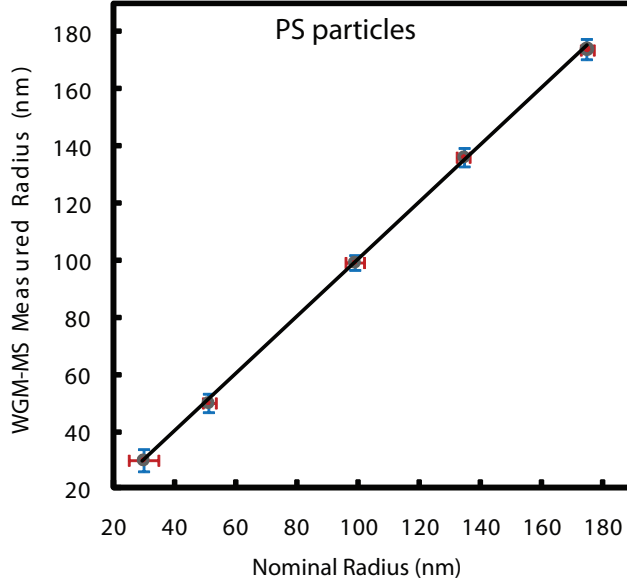
Figure 3.12: Single PS particle sizing using mode splitting in a microtoroid resonator. Estimated sizes of particles as a function of their actual sizes are shown. Error bars denote the standard deviations of size distributions.

3.2.3 Limitations

A nanoparticle is detectable if the splitting can be resolved in the transmission spectrum. This requires that the amount of splitting quantified as $|2g|$ should be greater than the sum of the frequency linewidth ω_c/Q of the WGM and the additional damping rate Γ_R. The lower detection limit can be derived from

$$|2g| = \frac{\alpha f^2(\mathbf{r})\omega_c}{V} > \frac{\omega_c}{Q} + \Gamma_R \tag{3.12}$$

where $\kappa_0 + \kappa_1 = \omega_c/Q$. Here, we define splitting quality as $Q_{sp} = |2g|/(\omega_c/Q + \Gamma_R)$, or the ratio of splitting over average linewidth. As long as $Q_{sp} > 1$ is satisfied, mode splitting can be clearly observed. In the cavity absorption limited regime ($\omega_c/Q >> 2\Gamma_R$) (Ozdemir et.al. 2011), the linewidths of the doublet are determined by the cavity linewidth, thus particle size information cannot be extracted. However, beyond this

regime, particle induced linewidth broadening becomes observable implying that the cavity linewidth is no longer the dominant factor. For the range of particles in our experiments, $2\Gamma_R/(\omega_c/Q) > 5\%$ is always satisfied. This means that particle induced linewidth broadening is measurable and size information can be extracted accurately as shown in Fig. 3.11 and 3.12.

For small nanoparticles, we have $\Gamma_R \ll \omega_c/Q$. Linewidth information cannot be accurately extracted in this case. But if $|2g| > \omega_c/Q$ the particle is still detectable, and it gives the lower detection limit of our scheme:

$$\alpha > \frac{1}{f^2(\mathbf{r})Q/V} \tag{3.13}$$

Consequently the lower limit of detectable particle radius is found as

$$R_{min} = \frac{\lambda}{2\pi n}\left[\frac{3(n_p^2 + 2)}{2F(n_p^2 - 1)}\right]^{\frac{1}{3}} \tag{3.14}$$

where $F = (3\lambda^3 Q)/(4\pi^2 n^3 V)$ is the Purcell factor and n is the effective refractive index of the resonance mode.

The highest Q achieved for microtoroid is around 4×10^8, and the microtoroid should not be smaller than $30\mu m$ in major diameter (Fig. 3.13a) to maintain this value, because further decrease of radius will increase radiation loss as well as surface scattering and surface contaminant related absorption (Kippenberg, Spillane and Vahala 2004). Such a microtoroid yields a mode volume of about $V = 1.5 \times 10^{-16} m^3$ which is calculated by numerical simulation using finite-element method. Figures 3.13b and 3.13c show the simulated WGM field distribution in the cross-section of the toroid ring quantified as $f(\mathbf{r})$ around 670 nm wavelength. On the surface of this microtoroid, the maximum value of $f(\mathbf{r})$ is 0.36. Inserting the values of V, Q and $f(\mathbf{r})$ in Eq. 3.14, we calculate the lower limit as R=9.2 nm and R=8.7 nm for KCl (n_p=1.49) and PS (n_p=1.59).
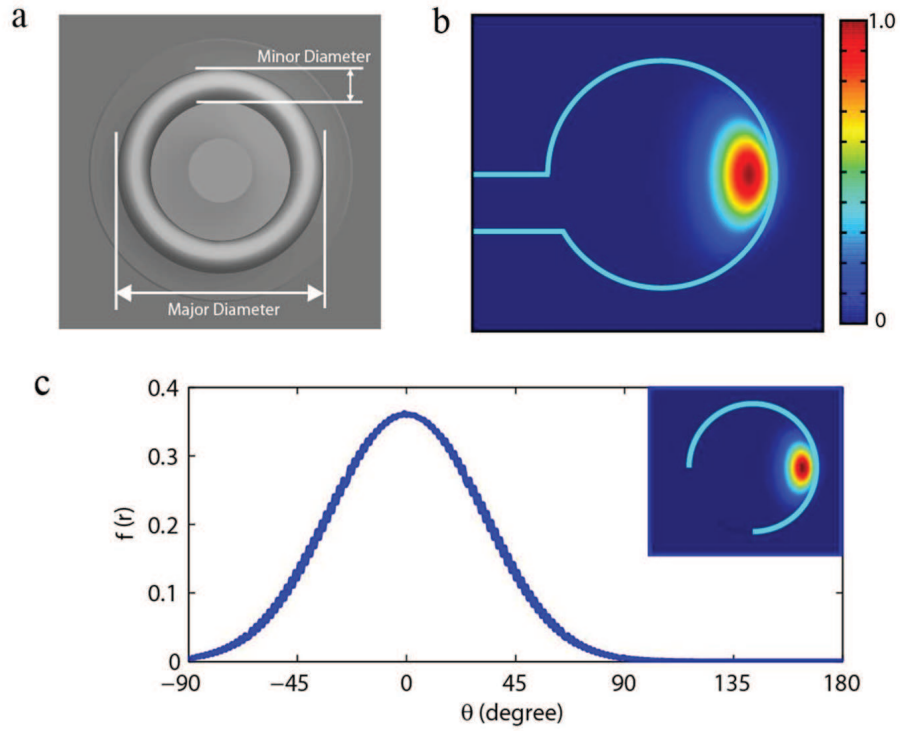
Figure 3.13: Field distribution of the whispering gallery mode for the microtoroid used in the experiments. **a**, Illustration of a toroid showing size notations. **b**, Normalized WGM field distribution in the cross-section of a microtoroid (Major diameter: $30\mu m$, and minor diameter: $5\mu m$) obtained by simulation for light wavelength of 670 nm. **c**, The normalized field distribution $f(\mathbf{r})$ along the outer surface of the microtoroid cross-section shown in **b**. The inset shows the trajectory of data points.
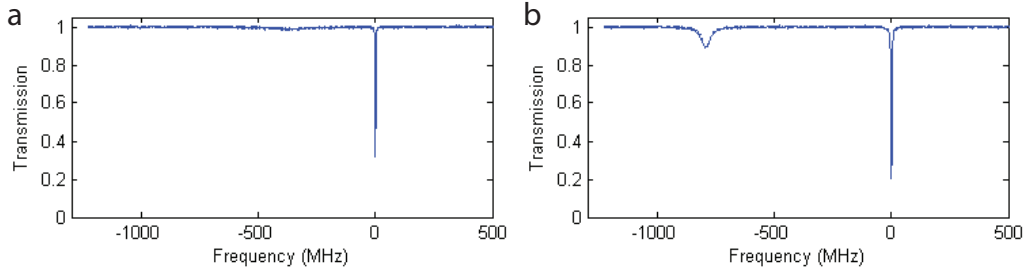
Figure 3.14: Transmission spectra obtained at two different wavelengths for a single PS nanoparticle of R=110 nm. **a**, For visible light at 670 nm band, symmetric mode cannot be clearly observed. **b**, For near-infrared light at 1450 nm band, the symmetric mode is seen due to the decreased damping at this wavelength band.

The upper detection limit, on the other hand, can be estimated from the conditions of Rayleigh scattering and dipole approximation which assume that $R \ll \lambda$. In our experiments, KCl and PS nanoparticles up to 100 nm in radius are detectable in 670 nm band, and the spectrum agrees well with the theoretical prediction derived using dipole approximation. For particles above this size, we see a large additional damping as $\Gamma_R \sim R^6$ (see Eq.3.2), consequently the Q-factor of the symmetric mode (SM) could become very low. The big difference in Q-factors of SM and ASM resonances makes it very difficult to monitor them simultaneously (Fig. 3.14a). However, when the wavelength is switched to near-infrared band (1450 nm) both resonances become clear (Fig. 3.14b) as the damping rate, which scales as $\Gamma_R \sim 1/\lambda^4$ decreases significantly.

It is worth noting here that although the theoretical model developed above states that there is no change in the linewidth of the high-Q mode (ASM), in the experiments we observed that for KCl particles of large size ($R \geq 180$ nm) the linewidth of ASM is also perturbed. Note that this size just exceeds the Rayleigh scattering regime and the theory in this chapter will not be accurate for this size. Table 3.1 shows the change in the linewidth of the ASM (high-Q mode) for KCl particles of different sizes for a single binding event. Although the table shows an 18% change in the linewidth of the high-Q mode for R =180 nm, we see that this does not lead to a significant error in size estimation.

37

Table 3.1: Changes in the linewidth of the high-Q mode (ASM) for KCl particles of various sizes. Linewidth of the High-Q mode is calculated using the curve fitting technique described above. The high-Q mode linewidth increases noticeably for large particles.

Intrinsic Q factor	Nominal Particle Radius (nm)	Change in High-Q mode linewidth	Measured Particle Radius (nm)
1.16×10^8	75	1.97%	72.49 ± 7.14
1.60×10^7	135	2.49%	131.03 ± 5.25
5.79×10^6	160	2.98%	160.27 ± 3.13
4.60×10^6	180	18.01%	178.78 ± 4.17

3.3 Regime for split and non-split mode nanoparticle measurement

The amount of frequency splitting and linewidth broadening between the split modes for the case of a single nanoparticle is given as $2g = -\alpha f^2(\mathbf{r})\omega_c/V$ and $2\Gamma_R = (\alpha^2 f^2(\mathbf{r})\omega_c^4)/(3\pi\nu^3 V)$. We have introduced a dimensionless parameter Q_{sp} (Ozdemir et.al. 2011) to quantify how well the splitting can be observed in the transmission spectrum of a scatterer-coupled WGM resonator. The splitting quality is given as:

$$Q_{sp} = \frac{2g}{\frac{\omega_c}{Q} + \Gamma_R} \tag{3.15}$$

that is the ratio of the frequency splitting over the average linewidth of the split modes (see Fig. 3.15). In order to identify mode splitting, $Q_{sp} > 1$ should be satisfied, as it is seen in Fig. 3.15 When $0.6 < Q_{sp} < 1$, although one cannot observe very clear split modes, the effect of the interaction between resonator and nanoparticle reflects itself as a "flat-top" feature. For $0 < Q_{sp} < 0.6$, one can observe only one resonance, i.e., mode splitting cannot be observed, and there is a single peak feature where the light-particle interaction is reflected as the change in resonant frequency and linewidth while keeping the lorentzian shape.
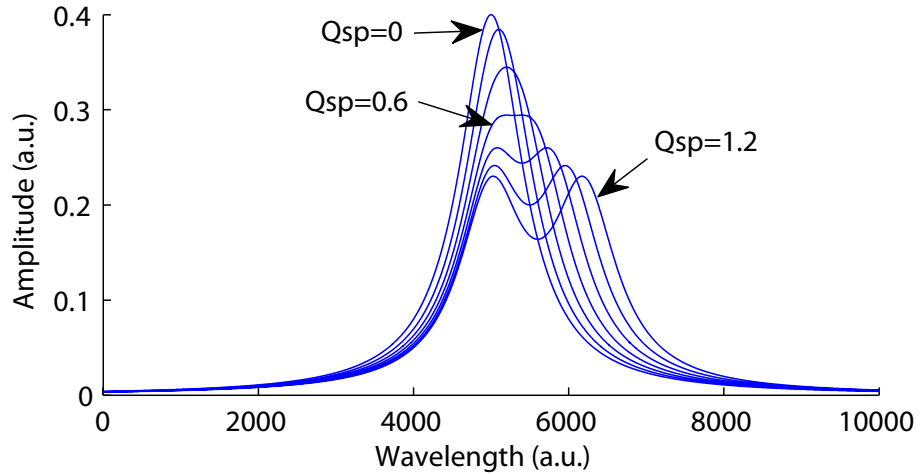
Figure 3.15: The effect of splitting quality Q_{sp} on the transmission spectrum of a WGM resonator. Q_{sp} is changes from 0 to 1.2 with increments of 0.2.

These observations suggest, with a conservative estimation, that the presence of a nanoparticle within the resonator mode volume will not lead to mode splitting if $Q_{sp} < 0.6$ is satisfied; and in order to observe a good mode splitting with well separated Lorentzian peaks which enables a good size estimation for the nanoparticle, Q_{sp} has to satisfy $Q_{sp} > 1.2$. Denoting the desired mode splitting quality as η, we can find a theoretical bound on Q such that there is no observable mode splitting in the transmission spectrum ($\eta < 0.6$) or well separated splitting ($\eta > 1.2$). It is straightforward to show that this bound can be derived from the condition $Q_{sp} < (>)\eta$ as

$$Q < (>) \frac{\omega_c}{\frac{\alpha f^2(\mathbf{r})\omega_c}{\eta V} - \frac{\alpha^2 f^2(\mathbf{r})\omega_c^4}{6\pi\nu^3 V}} \tag{3.16}$$

which relates Q-factor to the particle polarizability α (or size if refractive index is known).

The accuracy of size measurement depends on how well one can measure the frequency and linewidth of the split modes. In practice noise has a significant effect on whether the change induced by a particle can be observed in the transmission spectrum or not. It also affects how accurately the size measurement can be achieved.

For the size range of particles tested in our experiments, $|2g|/\Gamma_R$ is always satisfied, i.e. the amount of mode splitting or spectral shift is much larger than the amount of linewidth broadening induced by a single particle. Therefore, in our experiments it is always easier to measure the amounts of mode splitting or the spectral shift than to measure the linewidth broadening because any amount of measurement noise affects the estimation of linewidth broadening more than the estimation of mode splitting or spectral shift, i.e., in our experiments the signal-to-noise-ratio (SNR) of spectral shift measurement is much better than the SNR of linewidth measurement. Therefore, when considering whether a particle can be sized, linewidth measurement is the limiting factor with the present instrumentation systems.

In our experiments, the linewidth of the resonance is measured by curve-fitting of the frequency spectrum acquired by fine scan of the laser wavelength. Linewidth measurement noise arises due to laser noise, fiber-taper-toroid air gap fluctuation, other environmental noise in or around the microtoroid resonator (e.g. temperature fluctuations), and curve-fitting error. Linewidth measurement noise is relatively more significant when Q-factor of the resonance mode is high. To accurately measure a change in the linewidth, it is crucial that the change is larger than the noise level. In order to quantify the noise level in linewidth estimation, we acquired the transmission spectra over a course of 10 seconds corresponding to 100 frames during which the microtoroid was kept at normal experimental conditions without nanoparticle deposition (Fig. 3.16). By curve fitting to the resonances in each of these frames, we calculated the standard deviation of the measured linewidth which is an indication of the noise in linewidth measurement.

Figures. 3.17 and 3.18 summarize the relations between the standard deviation of measured linewidth (σ_Γ) vs. mean linewidth (ω_c/Q), and measured linewidth coefficient of variance CV (ratio of standard deviation over mean value σ_Γ/μ_Γ) vs. Q-factor. We observed that the linewidth noise becomes smaller when linewidth is smaller (or Q is larger), while the linewidth CV increases as linewidth goes smaller (or Q goes larger). From Fig. 3.18, we conclude that in our experiments σ_Γ is larger than 1/40 of the linewidth when $Q > 10^7$, and σ_Γ is larger than 1/20 of the linewidth when $Q > 10^8$. Thus, linewidth measurement noise plays a significant role especially in the size measurement of smaller nanoparticles using ultra-high-Q-factor resonance modes.
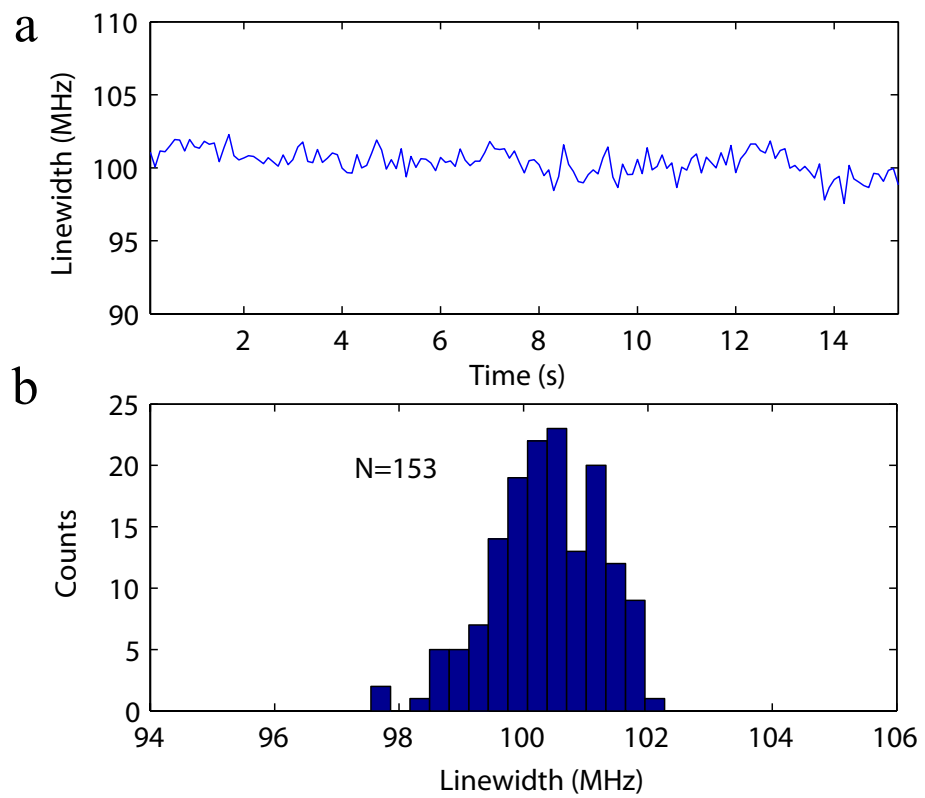
Figure 3.16: Measured linewidths vs. time showing the fluctuations in linewidth measurement. **a**, time signal. **b**, histogram of the measured linewidth
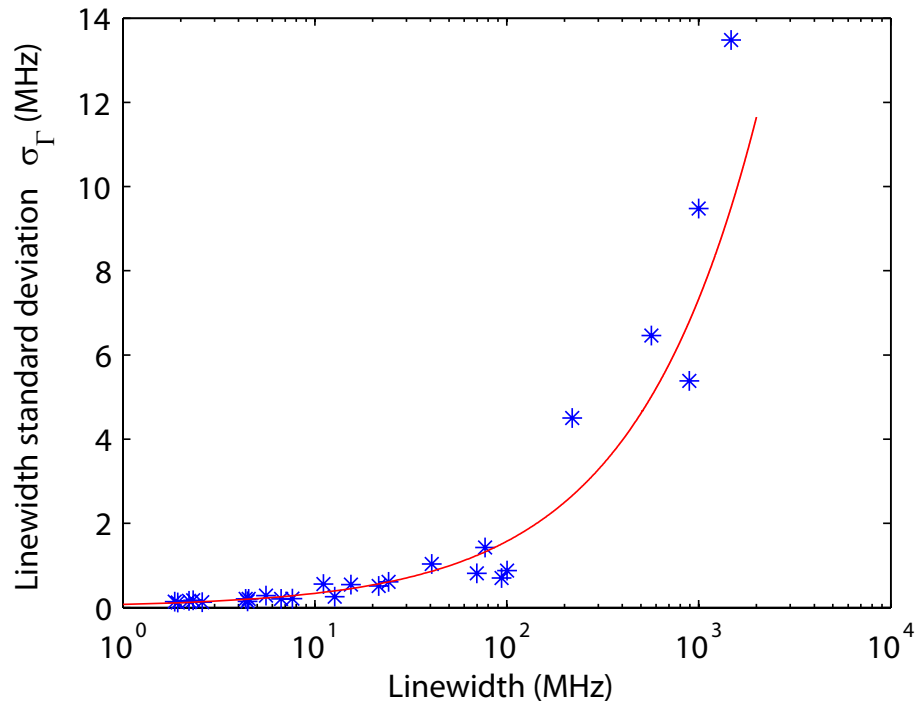
Figure 3.17: Measured linewidth standard deviation (σ_Γ) v.s. linewidth with the fitting curve given in red.
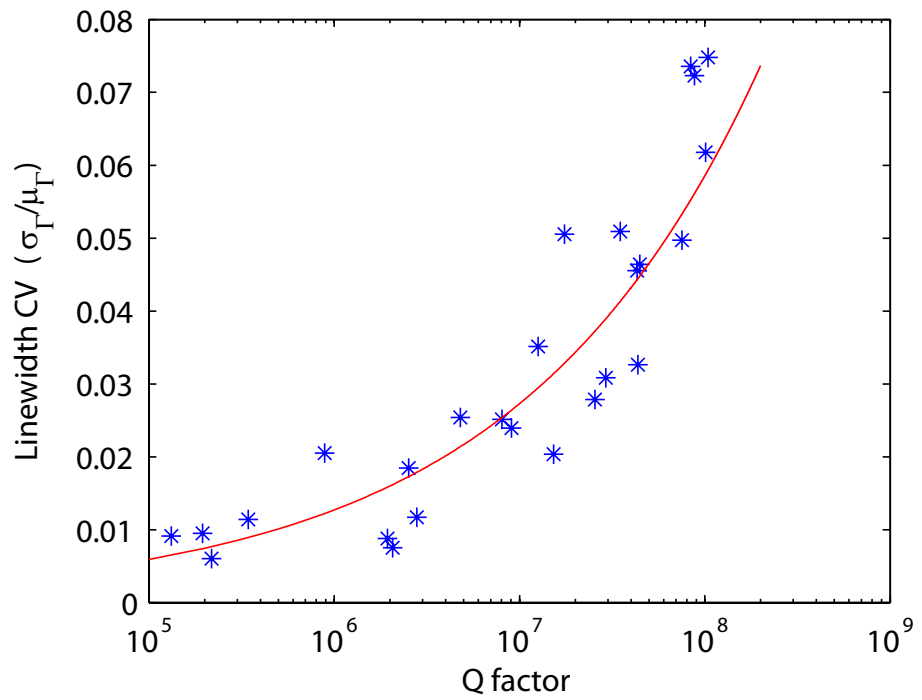
Figure 3.18: Measured linewidth coefficient of variance (σ_Γ/μ_Γ) v.s. Q-factor with the fitting curve given in red.

As we have mentioned above, accurate size measurement of a nanoparticle requires that the linewidth change (or broadening) induced by the particle is greater than the noise level of linewidth measurement, or linewidth standard deviation σ_Γ measured above. Imposing this, we find the relation:

$$Q > \frac{\sigma_\Gamma \omega_c}{\mu_\Gamma \Gamma_R} \tag{3.17}$$

which gives a lower bound for the Q factor for accurate size measurement. In Eq. 3.17, Γ_R is the linewidth broadening induced by a single mode, or average change of linewidth for split modes, ω_c/Q is the pre-scatterer linewidth of the single mode, or average linewidth of split modes before particle arrival. The value of σ_Γ/μ_Γ is dependent on Q and is given in Fig. 3.18. By curve fitting to the experimentally obtained data of Fig. 3.18, we find $\sigma_\Gamma/\mu_\Gamma \approx 0.00013 Q^{0.3317}$. Substituting this into Eq. 3.17, we arrive at

$$Q > (0.00013 \frac{\omega_c}{\Gamma_R})^{1.496} \tag{3.18}$$

In the multiparticle case in the next chapter, this bound is also valid for sizing an individual particle arriving at the resonator. In this case, the average Q-factor of the split modes before each particle deposition has to satisfy Eq. 3.18.

From the above discussions, it is clear that depending on the noise level, Q of the resonator and particle size, a WGM-resonator-based nanoparticle detection and measurement scheme operates either in a single mode or a split mode regime. In the single mode regime, no mode splitting is observed in the transmission spectra and measurement is based on detecting the spectral shift and linewidth broadening of a single resonance mode (Ren et.al. 2007). In the split mode regime on the other hand, the size measurement is based on detecting the total change in the frequencies and linewidths of the split modes. Combining the above equation sets we derive the boundaries of these two regimes as a function of particle size and Q of the resonator.
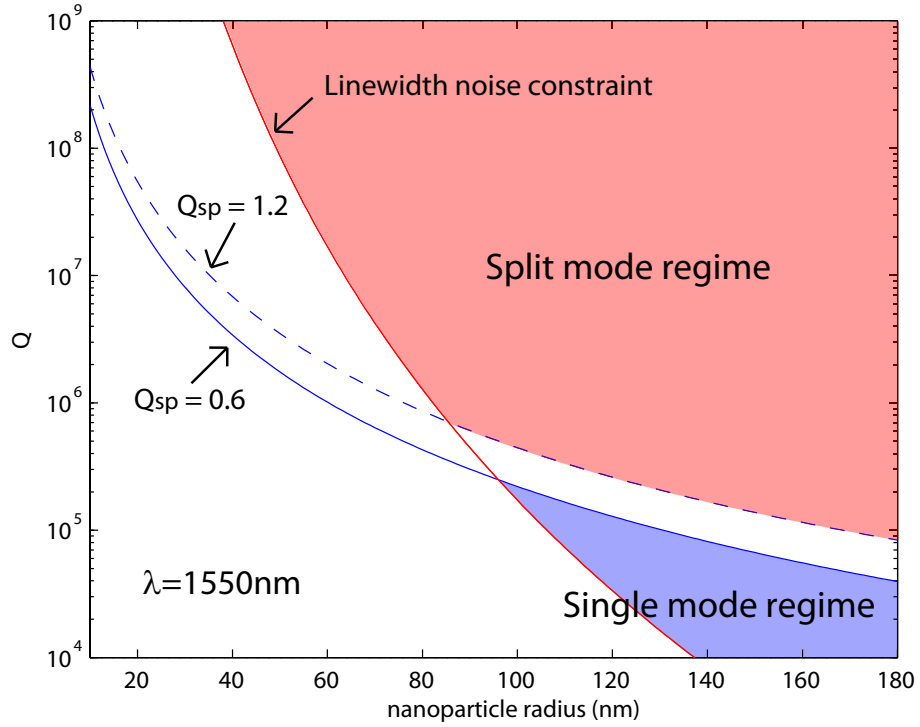
Figure 3.19: Regimes for single mode and split mode particle measurement at $\lambda = 1550nm$.

The results are shown in Figs. 3.19 and 3.20 considering PS nanoparticles (refractive index: 1.59) for the 1550nm and 670nm wavelength bands, respectively. The red curves in these figures denote the linewidth noise constraint (Eq. 3.18) and blue line is the boundary separating different operation regimes (Eq. 3.16). The upper limit for particle size in the plots are chosen to be the Rayleigh limits (R=180nm for 1550nm band and R=80nm for 670nm). Other parameters used in the simulations are $f(\mathbf{r}) = 0.36$ and $V = 200\mu m^3$.

In Figs. 3.19 and 3.20, the regions colored in blue correspond to the single mode regimes whereas the red colored regions are the split mode regimes. It is clear that the operation is single mode for lower Q and larger particle sizes (closer to Rayleigh limit). In this regime, one can measure the frequency shift and linewidth broadening of a single mode accurately and then calculate the polarizability (or size if refractive index is known) of the nanoparticle. In a system where Q-factor of a WGM resonator is low ($< 10^6$), it is likely that the measurement scheme will be in the single mode regime and size of a large nanoparticle can be estimated from the measurement of frequency

44
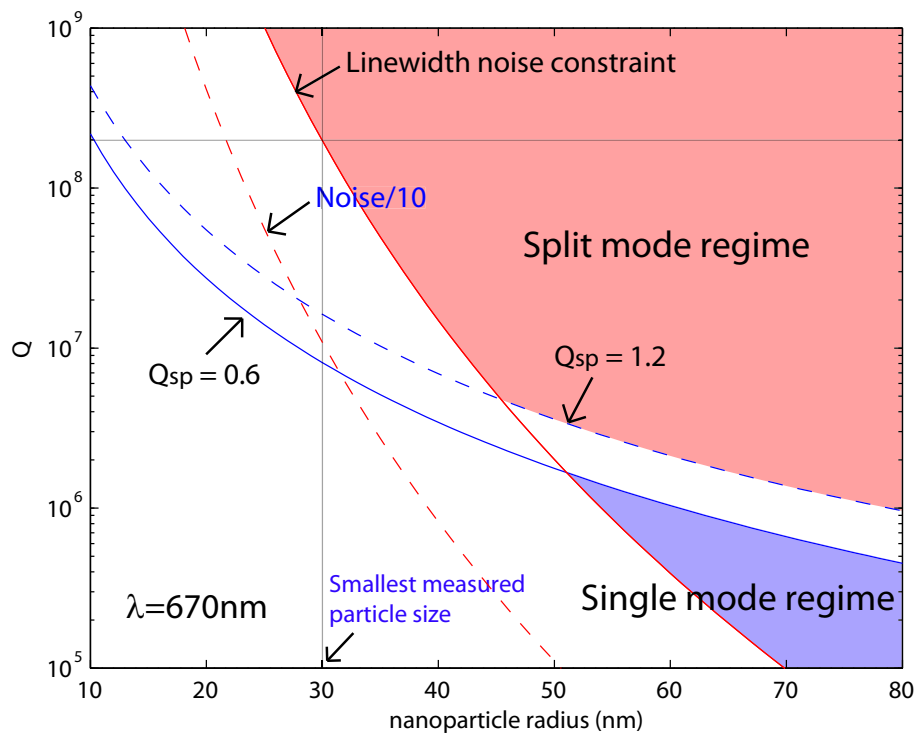
Figure 3.20: Regimes for single mode and split mode particle measurement at $\lambda = 670nm$. The smallest size of PS particle measured in experiment is 30nm in radius, which is measured close to the boundary of split mode regime. Dashed red curve shows the boundary if linewidth noise is decreased by 10 fold.

shift and linewidth broadening. For higher Q factors, split mode operation becomes possible. These figures suggest that with ultra-high- Q microtoroids ($Q > 10^7$), resonator-based measurement scheme will operate in split-mode regime.

Microtoroid resonators used in our experiments have Q values larger than 10^7 in air, therefore our measurement system almost always operated in the split mode regime (see Figs. 3.19 and 3.20). Working in the split mode regimes has two advantages: a) With higher Q-factor (or smaller mode linewidth), absolute standard deviation of linewidth measurement is smaller (Fig. 3.17). Thus, linewidth measurement is more precise. Consequently, size estimation is more accurate. b) Detection and measurement of much smaller particles are possible due to the higher Q-factor it utilizes.

Performance of both the single and split mode regimes is limited by the error in linewidth measurement. For example, if we could reduce the noise measured in our experiments by a factor of 10 (see Fig. 3.20, red dashed line), the areas of both single and split mode regimes will increase, thus smaller particles can be measured. In this case, the smallest measurable size for split mode regime would improve from R=30nm to 22nm (limited by the highest Q-factor obtainable 2×10^8) and that of single mode regime would improve from R=51nm to about 31nm.

During the particle deposition process, it may occur that $0.6 < Q_{sp} < 1.2$, and the transmission may appear as a "flat-top" Gaussian shape. In this case the linewidth measurement cannot be accurately performed because curve fitting error is relatively large. This problem is usually solved when more consecutive particles are deposited and Q_{sp} becomes larger than 1 again.

3.4   Summary

Mode splitting as a new scheme to detect and size nanoparticles have many advantages. First, the detection is based on the change of splitting frequency, which is naturally self-referenced. The split resonance may be affected by environmental perturbations and experience spectral shift. But the amount of splitting is not affected and only depend on the scattering signature of the nanoparticle. Second, the use

of both frequency and linewidth information gives this scheme its unique ability to quantify the nanoparticle adsorbed, without regard to the particle's location on the resonator and the Q factor and mode volume of the resonance. As the results show, this method is quite accurate considering this is only the prototype demonstration.

One big limitation of this method is that the sensitivity is bounded by the Q factor of the resonator and the sizing only applies to the first adsorbed particle. While the former restriction seems difficult to overcome for passive resonators, the latter limitation is solved in the next chapter, where new theory is developed to consider multiple scatterers in the system and allows real-time sizing of each consecutively deposited particles.

Chapter 4

Multiple Scatterers induced Mode Splitting

[2]In this chapter, we solve the problem of interaction between multiple Rayleigh scatters and resonator. The developed theory directly gives a method to allow consecutive detecting and sizing of incoming particles. It makes the microresonator a more realistic candidate for nanoparticle measurement applications since one can continuously measure each particle in the binding sequence. We start with the most simple case of two scatterers, where the theory is verified both in simulations and experiments. Then the theory is extended to multiple scatterers and applied to measure different types of nanoparticles and Influenza Virions.

4.1   Two Rayleigh Scatterers

When there is only one scatterer on the resonator, the two standing wave modes (SWMs) distribute according to the position of the scatterer (Mazzei et.al. 2007). The symmetric mode (SM) places its anti-node at the particle location and the asymmetric mode (ASM) places its node at the particle locations. In the case of two scatterers, situations are complex because the particle is no longer at the node or anti-node of a SWM (except for some specially cases). Both SWMs are perturbed by the

---

[2]Part of this chapter has appeared in "Controlled manipulation of mode splitting in an optical microcavity by two Rayleigh scatterers," Opt. Express 18, 23535-23543 (2010), and "Single virus and nanoparticle size spectrometry by whispering-gallery-mode microcavities," Opt. Express 19, 16195-16206 (2011).

scatterers, and the back-scattering from each scatterer will interfere and possibly enhance or decrease each other (Chantada et.al. 2008). Hence the coefficients we used to denote the coupling between the CW and CCW modes have to be modified. The damping effect, on the other hand, describe the dissipation of scattered light into the environment. For a traveling wave mode (TWM) the scattering loss from two scatterers are the same as the sum of the scatterers when they act independently. Because of this we know that the overall damping or linewidth broadening of the two SWMs should be just the summation of the two damping channel of the two scatterers according to the formulation in the last chapter.

4.1.1 Rate Equations

Instead deriving from the TWMs, we start from the SWMs to build the model and denote the the frequency of the too SWMs as (ω_-) and (ω_+). A single Rayleigh scatterer with polarizability α_1 located at $\mathbf{r}_1$ in the resonator mode volume V leads to a mode splitting quantified with the coupling strength $2g_1 = -\alpha_1 f^2(\mathbf{r}_1)\omega_0/V$ and the additional linewidth broadening $2\Gamma_1 = \alpha_1^2 f^2(\mathbf{r}_1)\omega_0^4/3\pi c^3 V$ where c is the speed of light, ω_0 is the resonance frequency before splitting, and $f^2(\mathbf{r}_1)$ is the normalized spatial variation of the intensity of the initial WGM. The resulting two SWMs have periodic (sinusoidal) spatial distributions. A single scatterer locates itself at the anti-node (node) of ω^- (ω^+) with $\phi = 0$ ($\pi/2$) where ϕ denotes the spatial phase difference between the first scatterer and the anti-node of $-$ mode. If a second Rayleigh scatterer with polarizability α_2 is introduced at location $\mathbf{r}_2$ with a spatial phase difference of β from the first scatterer, the already established SWMs redistribute themselves, and the amount of disturbance experienced by split modes depends on their overlap with the two scatterers (Fig. 4.1). Subsequently, the frequency shift $(\Delta\omega^- = \omega^- - \omega_0)$ and the linewidth broadening $(\Delta\gamma^- = \gamma^- - \gamma_0)$ of ω^- mode with respect to the pre-scatterer resonance frequency ω_0 and linewidth γ_0 become

$$\Delta\omega^- \;=\; 2g_1\cos^2(\phi) + 2g_2\cos^2(\phi-\beta) \tag{4.1}$$

$$\Delta\gamma^- \;=\; 2\Gamma_1\cos^2(\phi) + 2\Gamma_2\cos^2(\phi-\beta) \tag{4.2}$$
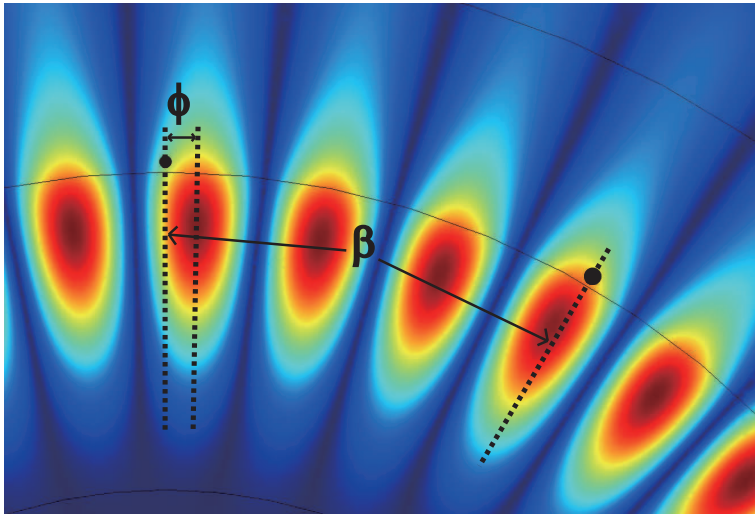
Figure 4.1: Field distribution of a standing wave mode (SWM) obtained from finite-element simulation and the definitions of ϕ and β. Black circles represent the position of two scatterers in the mode.

where subscripts (1,2) represents the first and second scatterers. The $\cos^2(\cdot)$ terms scale the interaction strength depending on the position of the scatterer on SWMs. Similar expressions for $\Delta\omega^+$ and $\Delta\gamma^+$ are obtained by replacing $\cos(\cdot)$ with $\sin(\cdot)$ since the two SWMs are always spatially orthogonal. Although Eq. 4.1 focuses on two-scatterer case, one can see that the model can be extended to arbitrary number N of scatterers by adding the terms $2g_i \cos^2(\phi - \beta_i)$ and $2\Gamma_i \cos^2(\phi - \beta_i)$, respectively, for each of the $3 \leq i \leq N$ scatterer.

To determine the distribution of the SWMs, we again use the Fermat's principal, which states that rays of light traverse the path of stationary (could be maximal or minimal) time. With the positions of the two scatterers fixed, the established SWMs are distributed in such a way that one SWM has the maximal round-trip optical path and the other one has the minimal (Chantada et.al. 2008, Zhu et.al. 2010). It in turn leads to maximal amount of splitting when one tries to adjust ϕ. In other words, the coupling rate between the two counter-propagating modes is maximized. By setting $d\Delta\omega^-/d\phi = 0$ or $d\Delta\omega^+/d\phi = 0$, we arrive at:

$$\tan(2\phi) = \frac{g_2 \sin(2\beta)}{g_1 + g_2 \cos(2\beta)} = \frac{\sin(2\beta)}{\chi\xi^2 + \cos(2\beta)} \tag{4.3}$$
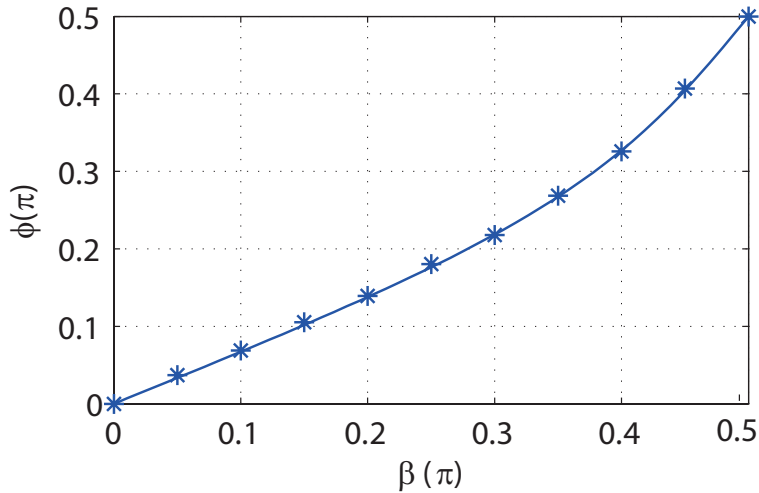
Figure 4.2: The relation between ϕ and β. Solid curve is calculated from Eq. (4.3) and $*$ represent the values calculated using finite-element simulations for $\chi = 0.5$ and $\xi = 1$.

where $\xi = f(\mathbf{r}_1)/f(\mathbf{r}_2)$ and $\chi = \alpha_1/\alpha_2$ are positive real numbers. The two solutions of ϕ have $\pi/2$ phase difference and correspond to the two orthogonal SWMs.

4.1.2 Finite Element Simulation

Verification of Eq. (4.3) is done by extensive finite-element simulations, and one example is presented in Fig. 4.2.

In this simulation for two particles. The first particle radius is $R_1 = 40/\sqrt{2}$ nm, the second has radius $R_2 = 40$ nm. Therefore, $\chi = \alpha_1/\alpha_2 = 0.5$. The two particles are placed the same distances away from the resonator surface, so that $\xi = f(\mathbf{r}_1)/f(\mathbf{r}_2) = 1$. By fixing the two particle sizes and change the position of 2nd particle, simulations give the relationship between the distribution of SWMs (ϕ) and β, as depicted in Fig. 4.2. The finite-element simulation results match very well with the calculated values from Eq. (4.3).

4.1.3   Controlled Experiments

Advances in microresonator science, particularly in cavity opto-mechanics, have revealed the need for tunable multi-mode resonators where multiple optical resonator modes interact with each other and with multiple external dipoles (e.g., emitters, particles or scatterers), lead to mechanical modes that cannot be excited in a single mode resonator, and are used to reach the standard quantum limit for cooling of mechanical modes with lower power budgets. Recently, tunable excitation and cooling of mechanical modes as well as phonon laser action have been demonstrated in a two-mode compound cavity (Grudinin et.al. 2010). Effect of a multi-mode cavity on cooling of mechanical modes has also been demonstrated in long optical cavities formed by two mirrors with tuning achieved by a heating element within the cavity (Zhao et.al. 2009). Thus, it is natural to ask whether there is a way to achieve similar tasks in a single microresonator. Controlled coupling of multiple optical modes in a single microresonator and their simultaneous or individual tunability without introducing significant damping will not only find immediate use in cavity opto-mechanics but also will facilitate applications such as filters, delays, tunable dual-wavelength lasers for terahertz radiation generation, as well as measurement of nanoparticles/molecules.

In this section we show that by tuning the coupling strength using nanoprobes or sub-wavelength scatterers, the split modes can be manipulated individually or together forming a tunable two-mode microcavity. We demonstrate that the modes can be tuned to cross or anti-cross in frequency and linewidth. Particularly interesting experimental observation is the tunable transition between standing wave mode (SWM) to travelling wave mode (TWM) and vice versa. Results of the calculation based on Eq. 4.1-4.3 explains and confirms the experimental observations as well as suggests a rather surprising dynamics, i.e., the two split modes can be made to cross each other twice in linewidth with frequencies undergoing anticrossing in one of the linewidth crossing region.

Figure 4.3 depicts the schematics of our experimental scheme which is composed of a WGM silica microtoroid resonator coupled to two nanoprobes prepared by heat-and-pull of optical fibers on a hydrogen flame followed by buffered HF etching. To couple light in and out of the resonator, a fiber taper is used. Positions of the nanoprobes
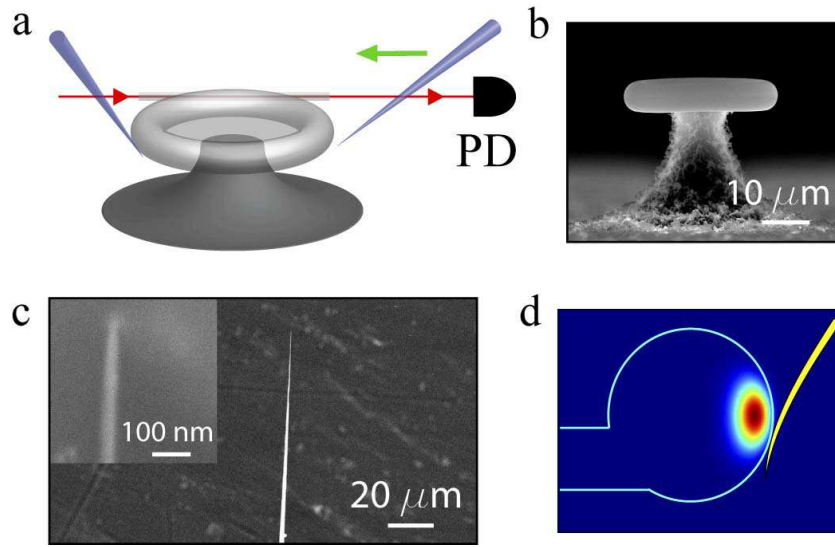
Figure 4.3: Setup of the controlled experiments with two scatterers. **a**, Schematics of the experiment showing a fiber taper coupled to a microtoroid, and two nano-fiber tips introduced into the mode volume. Transmission spectra are captured by a photo detector (PD). **b**, SEM image of a microtoroid. **c**, SEM image of a fiber tip. Inset shows the enlarged image of the tip. **d**, Cross-section of a microtoroid ring showing the position of a fiber tip in the field of a WGM.

and the fiber taper are finely controlled by 3D translational stages. We place the first nanoprobe in the resonator mode volume and fix its position when mode splitting is observed. We denote individual resonances of the doublet as ω^-(lower freuqency) and ω^+(higher frequency) modes with corresponding linewidths γ^- and γ^+ ($\gamma^- > \gamma^+$), respectively. Then the second probe is introduced. This probe bends down and slides along the surface vertically as it contacts the rim of the microtoroid. Due to the cone shape of the tip, vertical movement gradually increases its diameter allowing to simulate a scatterer of increasing size within mode volume without changing lateral position. This does not cause any observable damage to the microtoroid as witnessed by no change in the value of Q factor. As the second nano-tip size increases, it starts disturbing the already established SWMs. According to the Eq. 4.3, the evolution of SWMs and the amount of disturbance applied to $\omega^\mp$ and $\gamma^\mp$ depend on the size and location of the second probe relative to the first.

Figure 4.4 shows intensity graphs and transmission spectra recorded while the size of the second probe is increased. The second probe is used to tune the splitting between the modes and their linewidths. Crossing (Fig. 4.4b), anti-crossing (Fig.

4.4c) and shifting (Fig. 4.4d) of linewidths and resonance frequencies at different lateral positions(azimuthal direction, or β) of the second probe are observed.

In Fig. 4.4b, the initial ω^+ mode experiences red shift and linewidth broadening with increasing size of the second probe, while the ω^- mode is not perturbed much. At a specific size both modes coincide, i.e., $\omega^- = \omega^+$ and $\gamma^- = \gamma^+$. Thus, a single resonance is seen in transmission spectrum. With further increase of the second scatterer's size, the modes become separated with ω^- mode now having a larger linewidth than ω^+ whose linewidth equals to the initial γ^-. This suggests that both frequency and linewidth crossings have occurred. At the crossing point, back-scattering into the resonator vanishes as the back-scattered fields from the two scatterers have the same strength but π-phase shift. Thus the vanishing of backward reflection coupled to the taper suggests a transition from SWM to TWM. The conditions for these to take place will become clear in the later discussion. This observation implies that SWM, which limits nonclassical features of coherent matter-cavity field interaction due to the position dependence of the coupling strength, can be eliminated using external tuning with nanoprobes. This is particularly crucial in ultra-high-Q microresonators because SWMs are usually formed due to mode splitting caused by structural defects and material inhomogenety.

In Fig. 4.4(c), the second probe first disturbs ω^+ mode with no significant disturbance to ω^-. Thus ω^+ experiences linewidth broadening and red shift gradually approaching to ω^-. At a specific scatterer size, the frequency difference between the modes reduces from its initial value of 19.6 MHz to 7 MHz, and the linewidths become very close to each other. At this point, modes are strongly coupled to the scatterer and to each other. With further increase in size, ω^- strongly couples to the scatterer, and the modes start to repel each other leading to increased splitting. This suggests avoided-crossing of frequency and linewidth.

In Fig. 4.4(d), the second probe affects both ω^- and ω^+ and induces frequency shift and linewidth broadening. The rate of change in ω^- is higher than that in ω^+ suggesting that the scatterer has a greater overlap with ω^-.

To explain these experimental phenomena, we define $\delta = \Delta\omega^+ - \Delta\omega^- = \omega^+ - \omega^-$ and $\varrho = \Delta\gamma^- - \Delta\gamma^+$ as the frequency and linewidth differences of the resonance modes ω^- and ω^+, we find
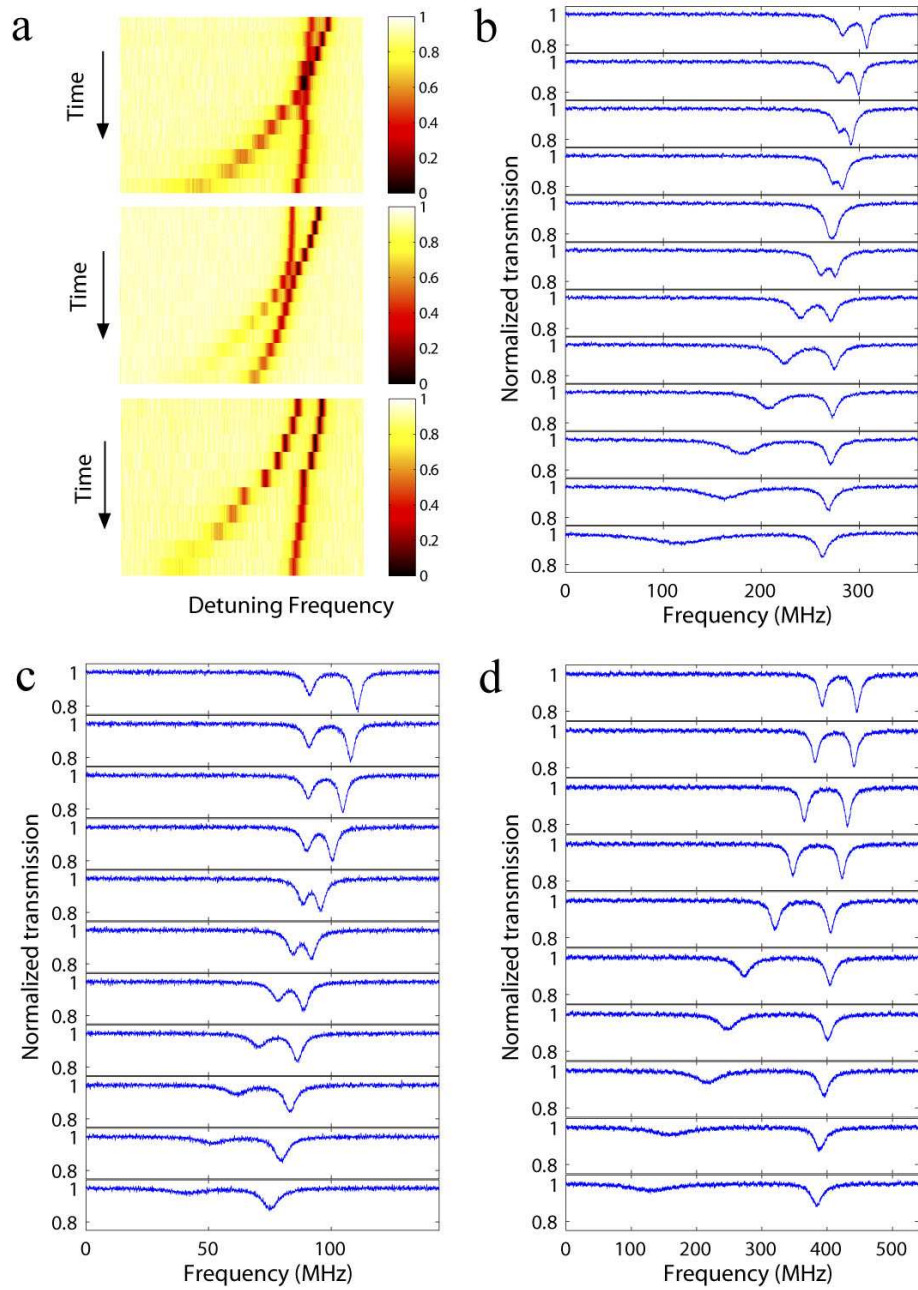
Figure 4.4: Experiment results with two nanoprobes showing different dynamics of the split modes. **a**, Intensity graphs of mode- crossing (top), anti-crossing (middle) and shift (bottom). **b-d**, Transmission spectra corresponding to the intensity graphs from top to bottom in **a**. Increasing time corresponds to increasing size of the second nanotip.

$$\delta = \frac{2|g_1|}{\chi \xi^2} [\chi^2 \xi^4 + 2\chi \xi^2 \cos(2\beta) + 1]^{\frac{1}{2}} \tag{4.4}$$

and

$$\varrho = \frac{4\Gamma_1 |g_1|}{\delta \chi^3 \xi^4} [\chi^3 \xi^4 + \chi(1 + \chi)\xi^2 \cos(2\beta) + 1] \tag{4.5}$$

from which frequency and linewidth crossings of the resonance modes can be calculated by setting $\delta = 0$ and $\varrho = 0$, respectively.

Behavior of the frequencies of the resonance modes. Conditions to observe frequency crossing is found by setting $\delta = 0$ which implies $\chi^2 \xi^4 + 2\chi \xi^2 \cos(2\beta) + 1 = 0$. It is satisfied only when $\cos(2\beta) = -1$ or $\beta = \pi/2$. In the following discussions we only consider $0 \leq \beta \leq \pi/2$, as $\cos(2\beta)$ is an even function and has period of π. Results of numerical simulations calculated from the model are shown in Fig.4.5, which coincide very well with experimental observations in Fig.4.4. Following are detailed discussions:

(i) $\beta = 0$. We find $tan(2\phi) = 0$, i.e., $\phi = 0$, implying that both particles locate at the anti-node of ω^-, and $\Delta\gamma^-$ is maximized. This leads to $\delta = 2|g_1|(1 + \chi^{-1}\xi^{-2})$. Thus decreasing χ increases δ by pushing ω^- further away from ω^+ (Fig. 4.5b). Note that if the size of the second scatterer reaches above Rayleigh limit (Knollenberg 1989), it may start disturbing ω^+, too.

(ii) $\beta = \pi/2$. The second particle stays at the anti-node of ω^+, thus increasing its size significantly affects the frequency and the linewidth of ω^+ while its effect on ω^- is minimal. Then we find $\delta = 2|g_1|(1 - \chi^{-1}\xi^{-2})$. This implies only one frequency crossing which occurs at $\chi = \xi^{-2}$, i.e., $g_1 = g_2$. For $\xi = 1$, frequency crossing occurs at $\chi = 1$ (Figs. 4.5a).

(iii) $0 < \beta \leq \pi/4$. We have $0 \leq \cos 2\beta < 1$ (i.e., cosine is positive in the first quadrant of the unit circle) which implies that for a fixed β in this interval, δ is always greater than zero ($\delta > 0$) and it increases with decreasing χ, that is with increasing α_2. Physically, this is understood as follows. The second scatterer affects both SWMs with strengths depending on its overlap with each mode. In this interval of β, the
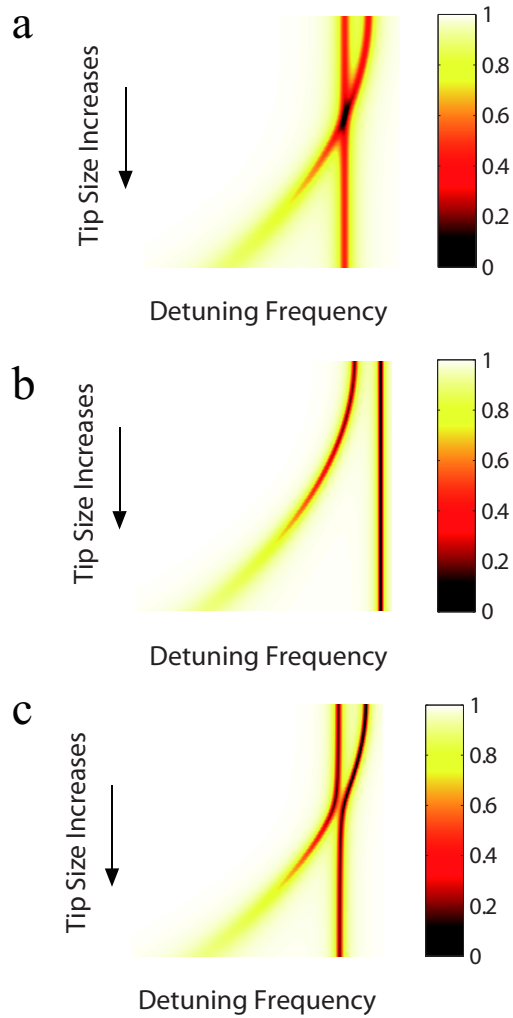
Figure 4.5: Numerical simulations showing three unique patterns of doublet evolution for increasing size of the second nanotip at **a**, $\beta = \pi/2$, **b**, $\beta = 0$, **c**, $\beta = 0.44\pi$ for $\xi = 1$, **d**, Resonance frequency and linewidth trajectories of the doublets with the exceptional point when ξ, χ and β are varied. Dashed and solid lines correspond to the two SWMs.

overlap of the second scatterer with ω^- mode is always larger than that with ω^+. Consequently, as α_2 increases, ω^- mode is further red-shifted increasing δ.

(iv) $\pi/4 < \beta < \pi/2$. We have $-1 \leq \cos 2\beta < 0$ (i.e., cosine is negative in the second quadrant of the unit circle) implying that for a fixed β in this interval, δ is always greater than zero ($\delta > 0$); however, contrary to the case (iii) δ has a minimum at $\chi\xi^2 = 1/|\cos(2\beta)| > 1$ with $\delta_{\min} = 2|g_1|(1 - \chi^{-2}\xi^{-4})^{1/2} > 0$. The physical process is explained as follows. In this case, too, the second scatterer affects both SWMs with strengths depending on its overlap with each mode. When the size of the second scatterer is small, ω^+ feels it strongly and undergoes frequency shift coming closer to ω^- as χ decreases. This changes ϕ and increases the overlap of the second scatterer with ω^- leading to their stronger interaction which consequently, red-shifts ω^- and helps avoid crossing ω^+ (Fig. 4.5c). With a sufficiently large α_2, $\phi > \pi/4$ will be achieved which means ω^- will have larger overlap with the second scatterer than the first one.

Behavior of the linewidths of the resonance modes. Setting $\varrho = 0$ in Eq. (4.5), we find the condition for linewidth crossing as $1 + \xi^4\chi^3 + \chi(1 + \chi)\xi^2 \cos(2\beta) = 0$ which can be satisfied only when $\cos(2\beta) < 0$ or $\pi/4 < \beta \leq \pi/2$, because both ξ and χ are positive real numbers.

(i) $\beta = \pi/2$. We have $\phi = 0$ and the two scatterers locate themselves at the anti-nodes of the each SWMs, i.e., 1st scatterer at ω^- and 2nd scatterer at ω^+. Thus scatterers independently affect the two SWMs. We find that a linewidth crossing takes place at $\chi^2\xi^2 = 1$, which means $\Gamma_1 = \Gamma_2$. In this case if we also have $\chi = \xi = 1$, which gives $g_1 = g_2$ and $\Gamma_1 = \Gamma_2$ implying the two SWMs have identical frequency and linewidth, but have orthogonal spatial distributions. The two SWMs merge to a TWM in the direction of the initial WGM. The other directional TWM vanishes as witnessed in experiments by vanishing of backward reflection in the fiber.

(ii) $\pi/4 < \beta < \pi/2$. The roots of $\varrho = 0$ can be found by setting $\chi^3\xi^4 + \chi(1 + \chi)\xi^2 \cos(2\beta) + 1 = 0$. This is a transcendental third-order polynominal equation whose roots are too lengthy to give here. Given $\pi/4 < \beta < \pi/2$, either none or two positive real roots can be found for χ at specific values of β and χ. This suggests that two linewidth crossing points may be observed. Indeed the double crossing patterns are seen in the calculated patterns shown in Fig. 4.6a,b. In both cases, one
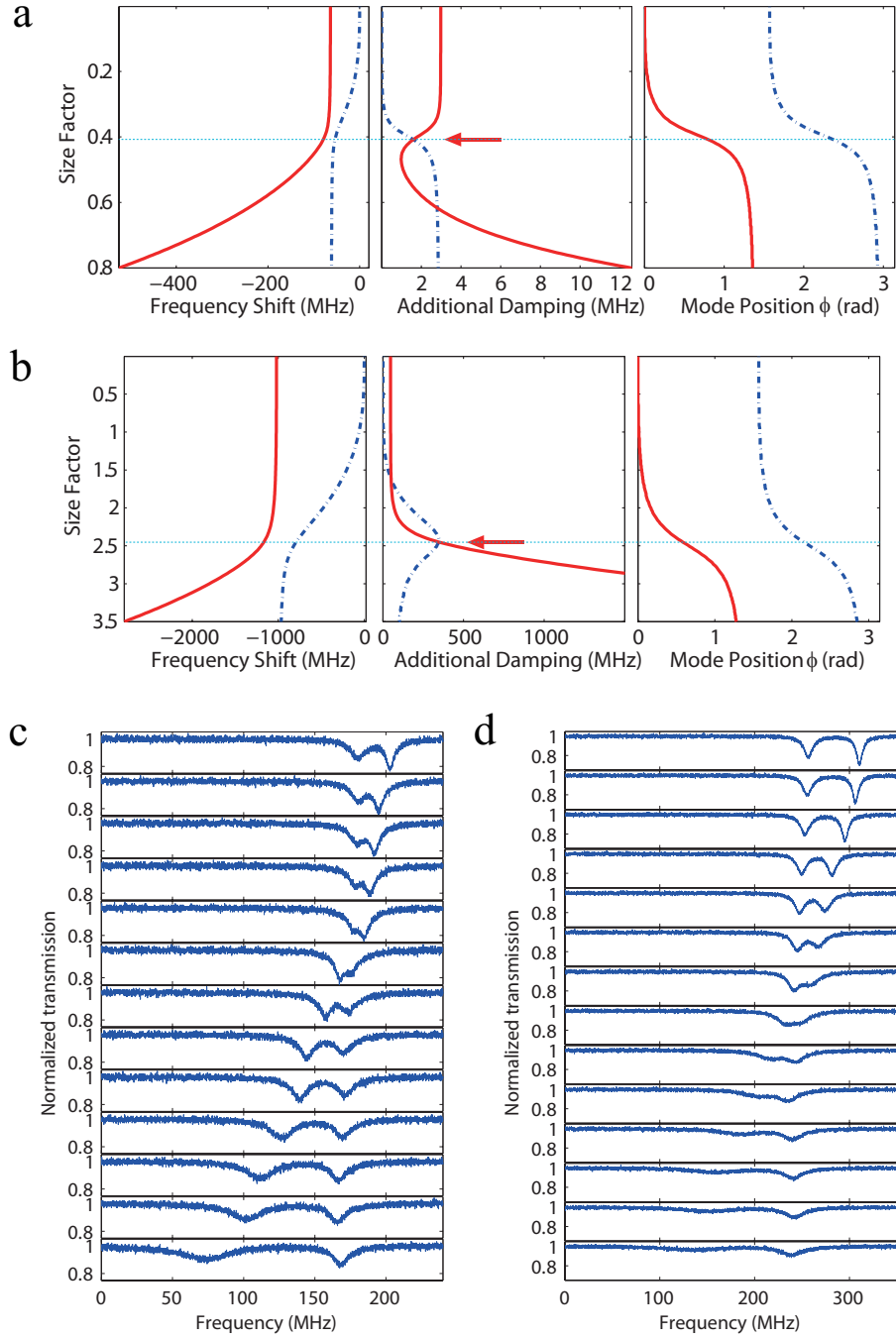
Figure 4.6: Calculated frequency shift, linewidth broadening of the doublet and SWM position ϕ as a function of the ratio of second scatterer size over the first one, for **a** $\beta = 0.44\pi$, $\xi = 1/4$, and **b** $\beta = 0.44\pi$, $\xi = 4$. Dotted and solid lines correspond to the two SWMs. **c,d** Experimental observations corresponding to **a** and **b**, respectively.

"symmetric" linewidth crossing (indicated by arrows in Fig. 4.6a,b) coincides with a frequency anti-crossing. From the plot of mode position ϕ, we see that the two SWMs "switch" distributions (ϕ shifts by $\pi/2$) around this point. This switching takes place around $\chi\xi^2 = 1$ and is the source of the symmetry of linewidth crossing. The other linewidth crossing takes place around $\chi^2\xi^2 = 1$, where the linewidth of one SWM changes significantly faster than that of the other one. This indicates that mode (red line in Fig. 4.6(a) and blue line in Fig. 4.6(b)) has much larger overlap with the second scatterer at this crossing point. Depending on whether $\xi > 1$ or $\xi < 1$, the "symmetric" linewidth crossing is observed before or after the other one. In experiments both scenarios were observed (Fig. 4.6c,d).

Moreover, in the case that no positive real roots are found for $\varrho = 0$, there is no linewidth crossing although one can always find χ for specific ξ and β which minimize ϱ. On either side of this minimum, ϱ increases implying linewidth anti-crossing. This can be explained in a similar way as the frequency anti-crossing when $\pi/4 < \beta < \pi/2$.

(iii) $0 \le \beta \le \pi/4$. In this case $\varrho \ne 0$ and similar to δ in this regime, ϱ increases as α_2 increases. Neither crossing nor anti-crossing can be observed.

In summary, this section discussed the interactions of a microresonator with two scatterers. The theory and method described here provide guidelines for manipulating the coupling of two SWMs and probing the mode splitting related phenomena.It also paves the ground for the discussions on detection of consecutively introduced nanoparticles using microresonators in the next section.

4.2 Multiple Scatterers

When multiple scatterers are in the mode volume, with each new scatterer entering the resonator mode volume, the already established WGMs are redistributed to maximize mode splitting (Fermat's principal). Subsequently, the location of individual scatterer with respect to the nodes and anti-nodes of the SWMs are modified. Assuming N-scatterers in the mode volume with ϕ_N denoting the distance between the first scatterer and the antinode of the ω_N^- mode, and β_i corresponding to the spatial

distance between the first and the i-th scatterer, we can write the frequency shift and the linewidth broadening that will be experienced by the split modes as

$$\Delta\omega_N^- = \sum_{i=1}^{N} 2g_i \cos^2(\psi_{Ni}), \quad \Delta\omega_N^+ = \sum_{i=1}^{N} 2g_i \sin^2(\psi_{Ni}) \qquad (4.6)$$

$$\Delta\gamma_N^- = \sum_{i=1}^{N} 2\Gamma_i \cos^2(\psi_{Ni}), \quad \Delta\gamma_N^+ = \sum_{i=1}^{N} 2\Gamma_i \sin^2(\psi_{Ni}) \qquad (4.7)$$

where $\psi_{Ni} = \phi_N - \beta_i$ and the $\cos^2(\ldots)$ and $\sin^2(\ldots)$ terms scale the interaction strength depending on the positions of the scatterers, and $2g_i$ and $2\Gamma_i$ correspond to the coupling strength and the additional linewidth broadening experienced by the WGM if the i-th scatterer is the only adsorbed scatterer. Imposing the condition that the modes distribute themselves to maximize mode splitting, we find that ϕ_N should satisfy

$$\tan(2\phi_N) = \frac{\sum_{i=1}^{N} g_i \sin(2\beta_i)}{\sum_{i=1}^{N} g_i \cos(2\beta_i)}. \qquad (4.8)$$

Then using the expressions in Eqs. 4.6-4.7, we find

$$\delta_N^- = 2\sum_{i=1}^{N} g_i \cos(2\psi_{Ni}), \quad \delta_N^+ = 2\sum_{i=1}^{N} g_i \qquad (4.9)$$

$$\varrho_N^- = 2\sum_{i=1}^{N} \Gamma_i \cos(2\psi_{Ni}), \quad \varrho_N^+ = 2\sum_{i=1}^{N} \Gamma_i \qquad (4.10)$$

In practical realizations, it is not possible to know the exact values of ψ_{Ni}, hence δ_N^- and ϱ_N^-, to extract useful information on the deposited scatterers. However, one can use δ_N^+ and ϱ_N^+ because these depend only on g_i and Γ_i which are directly related to the polarizability of the i-th scatterer. Consequently, we can write the polarizability of the N-th particle α_N as

$$
\begin{aligned}
\alpha_N &= -\frac{\Gamma_N}{g_N}\frac{3\lambda^3}{8\pi^2} = -\frac{3\lambda^3}{8\pi^2}\frac{\varrho_N^+ - \varrho_{N-1}^+}{\delta_N^+ - \delta_{N-1}^+} \\
&= -\frac{3\lambda^3}{8\pi^2}\frac{(\gamma_N^+ + \gamma_N^-) - (\gamma_{N-1}^+ + \gamma_{N-1}^-)}{(\omega_N^+ + \omega_N^-) - (\omega_{N-1}^+ + \omega_{N-1}^-)}
\end{aligned}
\tag{4.11}
$$

which states that by comparing the total frequencies and linewidths of the split modes before and after the deposition of the N-th scatterer, one can find the polarizability of the N-th scatterer from which the radius R_N is calculated as

$$
R_N = \left[\frac{\alpha_N}{4\pi}\frac{\epsilon_p + 2}{\epsilon_p - 1}\right]^{1/3}.
\tag{4.12}
$$

4.3 Consecutive Single Nanoparticle Measurements

Equations 4.11 and 4.12 show how to measure consecutively adsorbed nanoparticles on the microtoroid. In this section we perform the experiments to apply the developed theory. The experimental setup is essentially the same as the one used in single nanoparticle experiments. A labview program is used to capture the resonance spectra at a rate of 10 frames/s. Meanwhile the program also does curve fitting to the spectra to determine the frequency and linewidth of the split modes. When there is nanoparticle binds to the microtoroid surface, discrete changes in the frequencies or linewidths are observable indicating the binding event.

4.3.1 Influenza Virions

Purified and inactivated Influenza virus X-31 A/AICHI/68 was purchased in 4-(2-hydroxyethyl)-1-piperazineethanesulfonic acid (Hepes) buffer from Charles River Laboratories. The virus sample was passed through a 0.2 μm nylon membrane filter to remove aggregates. The virions are delivered to the microtoroid surface using the
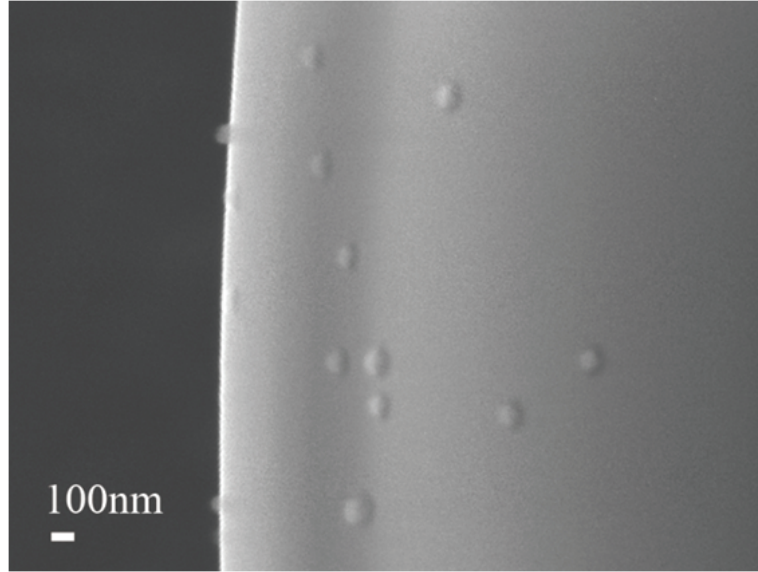
Figure 4.7: A SEM image of Influenza A virions deposited on the surface of a microtoroid resonator

method described in Chapter 3. The deposition results are confirmed by optical microscopy imaging via visible light scattering and further confirmed by SEM images (Fig. 4.7).

Figure 4.8 shows the mode splitting spectra induced by InfA virions entering the resonator mode volume one-by-one. With the arrival of the first virion, the single resonance splits into two. The subsequent single virion adsorptions lead to redistribution of the existing SWMs leading to abrupt changes in the splitting spectra (Fig. 4.8a). The amount of change in the frequency and linewidth of the resonance modes with each adsorption event depends on the positions of the virions in the mode volume. The mode splitting resonance frequencies and linewidths extracted from the spectra in Fig. 4.8a shows sudden changes corresponding to each individual virion adsorption event (Fig. 4.8b,c). Processing this data allows to extract the polarizability and hence the size of each virion (Fig. 4.8g). Note that particles deposited outside the mode volume do not affect the WGM, so they have no effect on the resonance spectrum.

Extracted frequencies and linewidths of the split resonances from the experimental data shown in Fig. 4.8a are depicted in Figs. 4.8b,c. This information is subsequently used to calculate δ_N^+ and ϱ_N^+ (Fig. 4.8d,e). Single virion adsorption events are clearly visible as discrete jumps in 4.8d,e. Although the height of each discrete jump depends
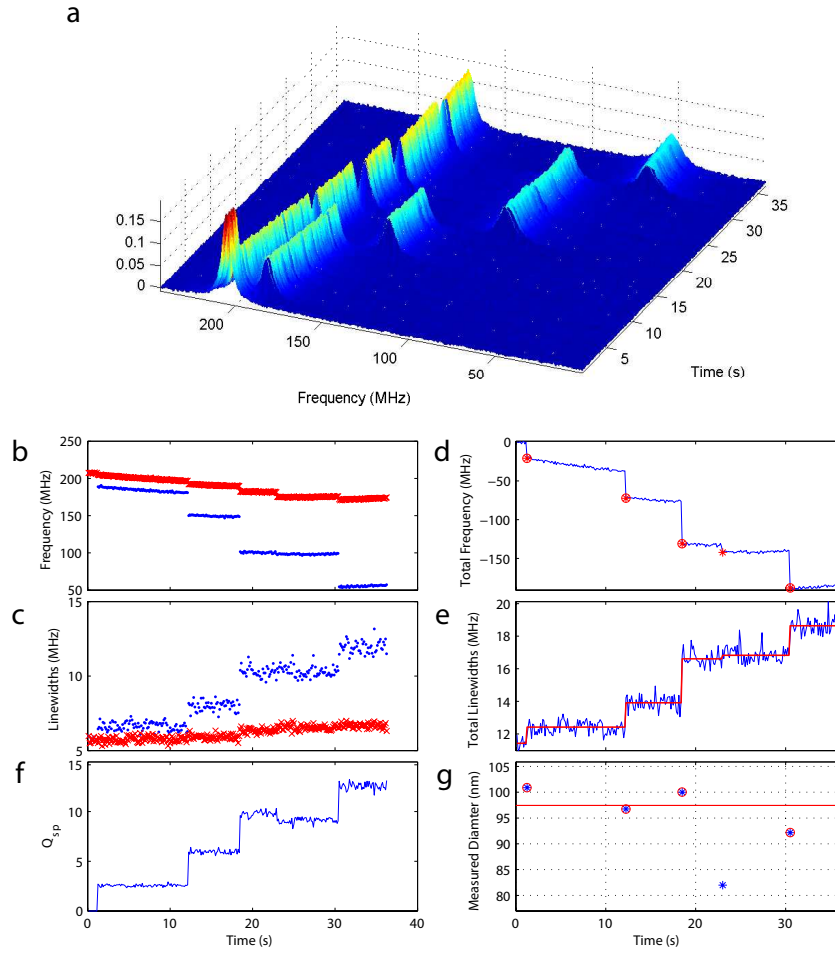
Figure 4.8: Real-time records of single InfA virion adsorption events using mode splitting phenomenon in a microtoroid optical resonator. **a,** Evolution of transmission spectra as the single virions are adsorbed onto the resonator mode volume. The single resonance splits into a doublet with the first virion binding event. The subsequent binding events lead to abrupt changes in the mode splitting spectra. Each abrupt change corresponds to detection of a single virion, and the amount of change depends on the polarizability and the position of the adsorbed virion in the mode volume (see Eqs. 4.6 and 4.7). **b,** Frequencies and **c,** linewidths of the two split modes extracted from the data in **a** by curve fitting. **d,** Sum of the frequency shifts of the two split modes with respect to frequency of the initial single mode resonance mode, δ_N^+, and **e,** sum of the linewidths of the split modes, $\rho_N^+ + 2\gamma_0$. **f,** Evolution of splitting quality $Q_{sp} = 2\delta_N^-/(\varrho_N^+ + 2\gamma_0)$ as a function of time. Note that mode splitting is observable in the transmission spectrum if $Q_{sp} > 1$. **g,** Size of each adsorbed single virion calculated from the data in **d** and **e** using Eqs. 4.11 and 4.12. The horizontal line designates the average size. In **d** and **g,** the '*' signs mark the point of single virus adsorption events, and circles mark the events from which accurate size information could be extracted.

64

on the position of each virion within the resonator mode volume, we can accurately measure the size regardless of the virion position. Using Eqs. 4.11 and 4.12, we estimated the polarizability from which the size of the adsorbed virions was derived and presented in Fig. 4.8g. Assuming a refractive index of 1.48 for virions (Wang et.al. 2010), we calculated the radii of the five adsorbed virions to be in the range $46 - 55$nm. As seen in Fig. 4.8e, the change in total linewidth ϱ_N^+ for the fourth virion adsorption event is within the noise level of our system. Although the estimated size for this virion differs from the expected nominal size, this does not prevent detecting this virion thanks to the distinct change in total frequency δ_N^+ (Fig. 4.8d).

Polarizability and size distributions of InfA virions are depicted in Fig. 4.9a and 4.9b, respectively. Measured radius $R = 53.2 \pm 5.5$nm for InfA virions agrees very well with the values reported in the literature (Vollmer, Arnold and Keng 2008, Wang et.al. 2010).

4.3.2   Inorganic Particles

We also used the same method to deliver Gold (Au) and PS nanoparticles one-by-one to the microtoroid surface, and measured their polarizability and size distributions. The deposition results are also confirmed by optical microscopy imaging via visible light scattering and further examined by SEM images (Figs. 4.10 and 4.11). The laser wavelength used for R = 50 nm gold particles is in 670 nm band and the one for R = 100 nm gold particles is in 1550 nm band. The refractive index used for gold nanoparticle is taken as $n = 0.55 + 11.5i$ at 1550 nm, and $n = 0.163 + 3.46i$ at 670nm (Palik, http://refractiveindex.info). In both cases, the pump frequency is away from the plasmon resonance frequency of the gold particles and in experiments no plasmonic effect is observed.

According to our observations the inorganic particles have much less probability to be adsorbed onto the silica resonator surface than InfA virions upon collision. Also PS particles are a little easier to bind than gold ones. The binding rate is determined by comparing the particle concentration in the carrier flow and the detecting rate of the resonator system.
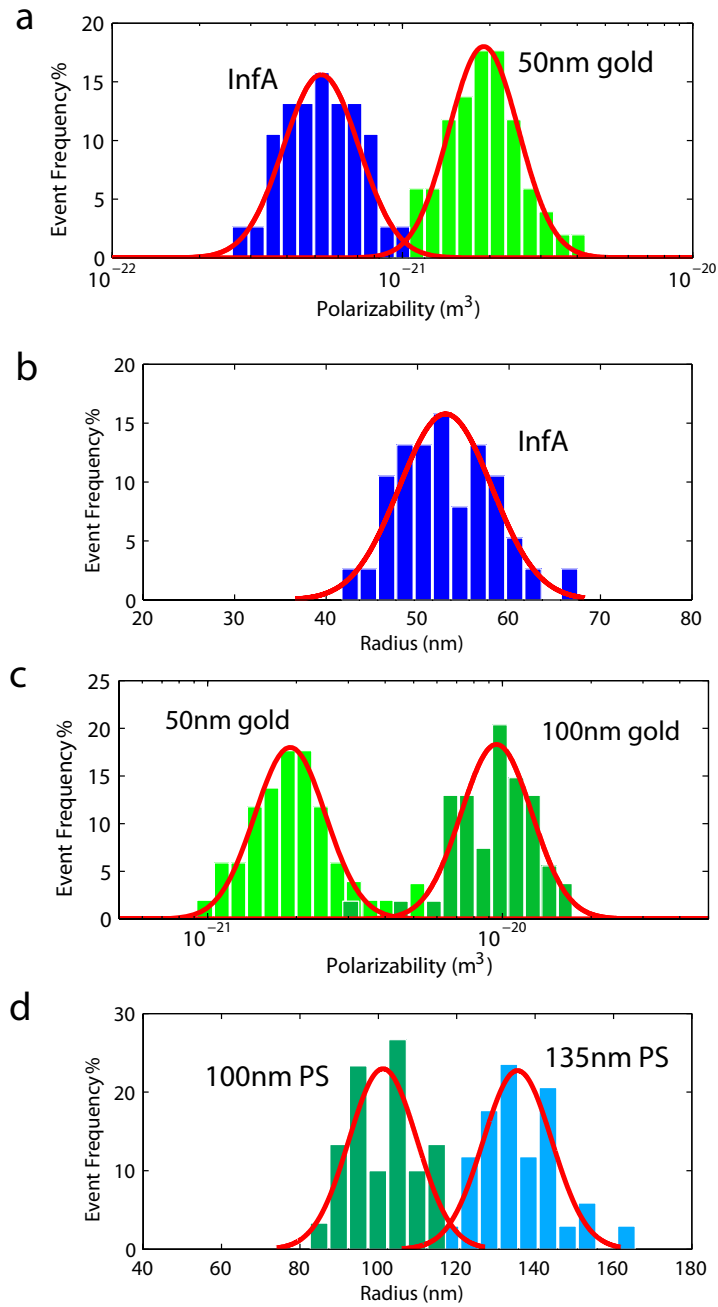
Figure 4.9: Single virus/nanoparticle spectrometry using mode splitting in a micro-toroid resonator. Polarizabilities and sizes are calculated from transmission spectra according to Eqs. 4.11 and 4.12. **a,** Measured polarizability distributions of InfA virions and 50 nm Au nanoparticles. **b,** Measured size distribution of InfA virions with average radius at 53.2 nm. **c,** Measured polarizability distributions of 50 nm and 100 nm Au particles. **d,** Measured size distrbutions of 100 nm and 135 nm polystyrene (PS) particles. Red curves are Gaussian fits to the experimentally obtained distributions.
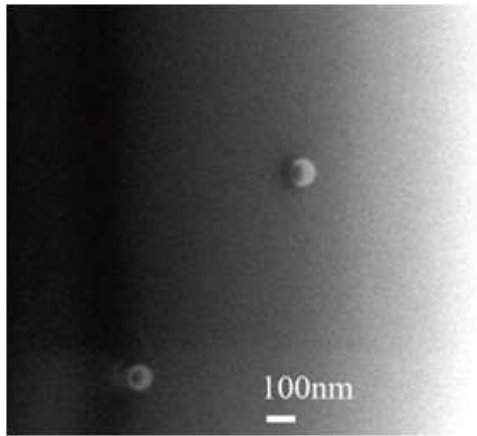
Figure 4.10: SEM image of PS particles with diameter of 100 nm deposited on a microtoroid resonator.
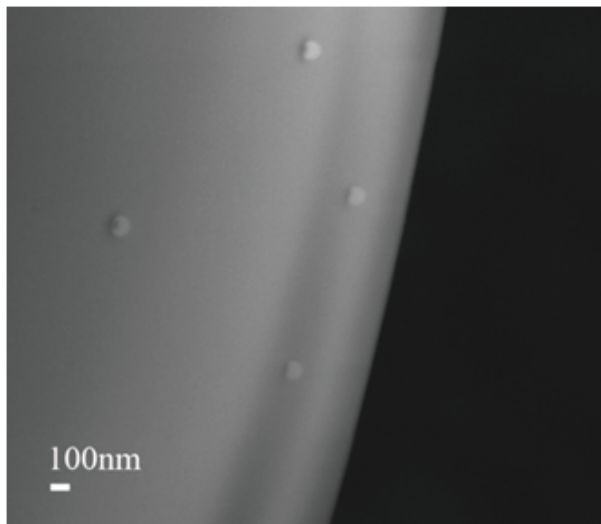
Figure 4.11: SEM image of gold particles with diameter of 100 nm deposited on a microtoroid resonator.

For comparison, we show in Fig. 4.9a,c the experimentally obtained polarizability distributions of Au nanoparticles with $R = 50$nm and $R = 100$nm. Figure 4.9d depicts the distribution of estimated sizes for PS particles of $R = 100$nm and $R = 135$nm. The measured distributions of the tested nanoparticles are significantly different correlating with their sizes and material properties.

For PS particles with nominal radius of $R = 100 \pm 1.7$ nm and $R = 135 \pm 2.1$ nm, our size estimation yielded $R = 101.2 \pm 9.05$nm and $R = 135.9 \pm 9.96$nm nm, respectively. The standard deviations of measured polarizability distributions (Fig. 4.9a,c) for Au particles are 32% and 31%, respectively for $R = 50$nm and $R = 100$nm. These are slightly larger than the 24% polarizability deviation estimated from the 8% size deviation claimed by the manufacturer.

The standard deviation of the estimated particle sizes and polarizabilities using our technique have four main contributions: (i) Standard deviation of the particles, (ii) detection noise and the laser frequency fluctuations, (iii) curve fitting noise in extracting the resonance frequencies and linewidths of the split modes, and (iv) fluctuations in the taper-resonator gap. We performed all experiments in normal laboratory environment with no active control of the conditions. Thus, we believe that the reported results can be improved by proper conditioning and control of laser phase and intensity noise as well as taper-resonator gap.

4.3.3   Spectrometry of Nanoparticle Mixtures

We also examined our system's response to a mixture of PS and gold nanoparticles with the same radii $R = 50$ nm. The two kinds of particles are simultaneously present in the air flow being blown onto the microtoroid. The measured polarizability distributions are shown in Fig. 4.12. The two maxima are easily seen and the two distributions have small overlap suggesting that our method can be reliably used to detect multiple components of a homogenously mixed ensemble of particles and to decide whether the given composition of particle ensemble is mono or poly-modal. This result is attributed to the ability of measuring particles one-by-one and it poses a significant advantage over other method, since in the schemes based on the spectral shift of a single resonance mode (in optical resonators or mechanical cantilevers), the
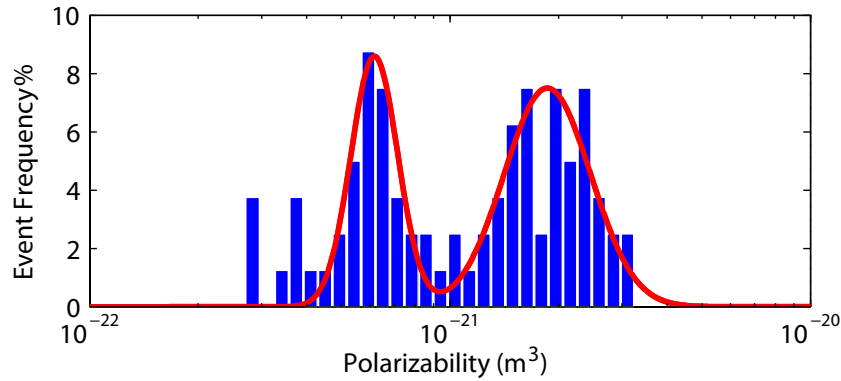
Figure 4.12: Measured polarizability distributions of a homogenous mixture of PS and Au particles with radii 50 nm. Bimodality of the mixture is accurately determined from the processing of mode splitting spectra. Red curves are the Gaussian fits to the experimentally obtained distributions.

distribution of frequency shifts induced by smaller particles could be buried within the distribution of larger ones, making it difficult to resolve the modality.

4.3.4 Experiment Procedures

Here we summarize the procedures of the consecutive particle measurements (see also Fig. 4.13):

1. Choose a microtoroid resonance mode with high Q-factor. The mode may or may not have initial mode splitting.

2. Start nanoparticle deposition using the DMA system accompanied with the nozzle and monitor the transmission spectrum continuously at a rate of > 10 frames per second. The particle concentration and flow speed are adjusted such that the chances that two particles coming out of the nozzle and landing on the resonator mode volume within one frame are negligible.

3. A particle binding event is signaled by splitting of a single resonance into two if there was no initial mode splitting, or by a sudden change in the mode splitting spectrum (frequency or linewidth change or both) if there existed mode splitting. Curve fitting is used to estimate the frequency and linewidth of split modes from each transmission spectrum.
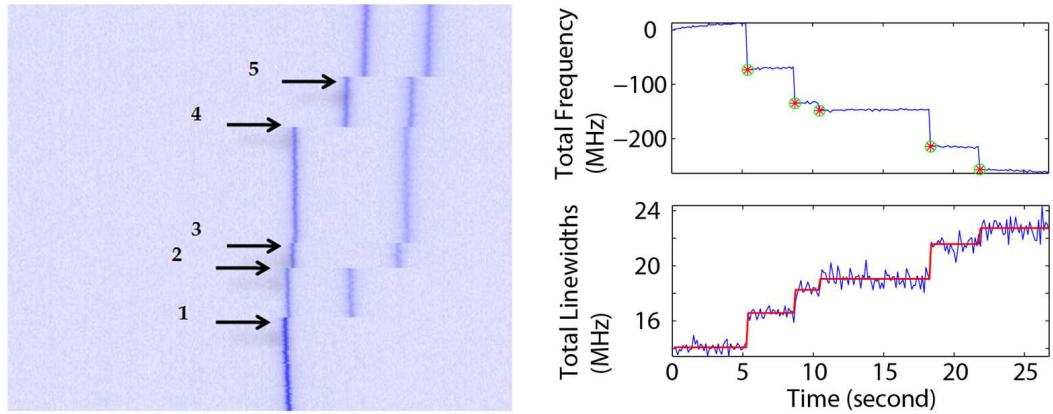
Figure 4.13: Transmission spectra (intensity graph) obtained during continuous deposition of PS particles with radius of 100 nm. Only the first 5 binding events are shown here. The right panel shows the total frequency shift and change of total linewidth from the split modes.

4. Once a particle is detected with a measurable change in both the total linewidth and the total frequency of the split modes in the two frames right before and right after the particle binding, calculate the ratio of total linewidth change to total frequency change and extract the polarizability of the particle according to Eq. 4.11.

5. If the refractive index of the particle is known, estimate the size using the relation between polarizability, refractive index and size of the particle assuming the particle is spherical. This assumption is largely validated as we have used reference PS and gold nanoparticles. For the case of InfA virions, our measurement yields the size equivalent to a spherical nanoparticle with refractive index 1.5 (reported value of refractive index for InfA virions).

6. Repeat the particle detection and measurement steps until the Q-factor of the resonance is too low to accurately measure the upcoming particle induced changes.

4.4   Analysis

In this section we present several simulations and discussions on the experiment results and the theoretical model.

4.4.1   Detection and Sizing Limit

Theoretical detection limit of our scheme is mainly dependent on Q/V of the resonator and the wavelength of the resonance. For a dielectric nanoparticle of refractive index 1.5, detection limit is around $R = 10$nm with an ultra-high-Q resonance in 670nm wavelength band. In our experiments using microtoroids with $Q \geq 10^8$, the smallest detected PS particles were of radii $R = 20$nm, and the smallest PS particles detected and accurately measured were of radii $R = 30$nm.

4.4.2   Performance Comparison

In this subsection, we compare the performance of size estimation using mode splitting in a WGM optical resonator with those using Scanning mobility particle sizer (SMPS), dynamic light scattering (DLS), SEM and the manufacturer provided data. In this study we used Gold and PS nanoparticles and Influenza A virions. The gold and PS nanoparticles of radii R=100nm are certified reference materials provided by British Biocell International Limited and Duke Scientific, respectively. The manufacturer data sheet claims that measurements using transmission electron microscopy (TEM) yield an average radius of R=98.5 nm with a standard deviation of 7.9% for the gold particles, and an average radius of R= 101.5nm with a standard deviation of 2.3% for the PS nanoparticles. The published data in the literature reports that the InfA virions have radius in the range of 40-70nm.

Scanning Mobility Particle Sizer (SMPS) measurement of PS and gold particles.   We measured the size distribution of the particles exiting the DMA used in our experiments by using a scanning mobility particle sizer (SMPS). The particles exiting the output of the first DMA used in our experiments were fed into the SMPS which is a second DMA whose central rod voltage is exponentially scanned to obtain the full particle size distribution at its output. Note that in our experiments, the particles at the output of the first DMA are deposited onto the toroidal resonators. Thus, in these measurements SMPS replaces our resonator-based measurement scheme. In the measurements, particle flow rates were set as 1.5 liter/minute for both DMAs, and sheath flow rate was set at 15 liter/minute for the first DMA and 10 liter/minute for the second one. Obtained size distributions for R=100 nm gold and PS particles
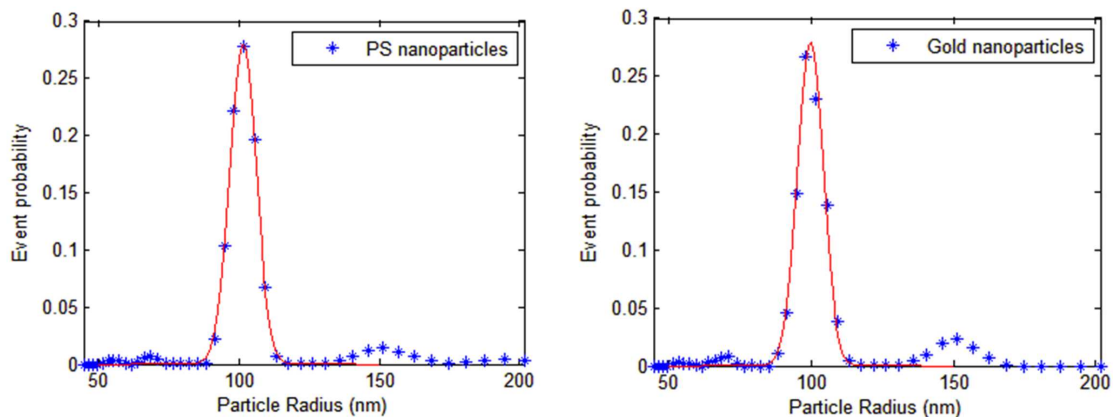
Figure 4.14: Measured size distribution for 100 nm PS and Gold nanoparticles using SMPS. The side peaks are due to multiply charged particles in the DMAs.

are given in Fig. 4.14 Two small side peaks around the major peak are due to the multiply charged particles in either first or second DMA, which results in different electrical mobility for the particles of the same size. Multiple-charge correction algorithm has been applied to the size distributions. The correction reduces the height of the side peaks but cannot eliminate them entirely. Gaussian fit is applied to both distributions to extract the mean size and standard deviation.

Dynamic Light Scattering (DLS) measurement of PS, gold particles and InfA virions. We used a DLS system (Malvern Zetasizer Nano) to measure the PS and gold nanoparticles and InfA virions used in our experiments. In DLS, particles are in a suspension undergoing Brownian motion. When illuminated with a laser, the intensity of the scattered light fluctuates at a rate depending on the sizes of the particles, i.e., smaller particles move more rapidly. The velocities of the Brownian motion of the particles are extracted from intensity fluctuations of the scattered light and then the particle size is estimated using the Stokes-Einstein relationship. In a DLS measurement, what is measured is the hydrodynamic size of the particle. In other words, size obtained by DLS is that of a spherical particle having the same translational diffusion coefficient as the particle under test. It is to be noted that besides the particle's size, the diffusion coefficient depends on the surface structure, the concentration and type of ions in the measurement medium. Thus, the size obtained by DLS can be larger than the size measured by SEM, TEM, SMPS or our resonator-based method where the particles are removed from their aquatic environment. The

72
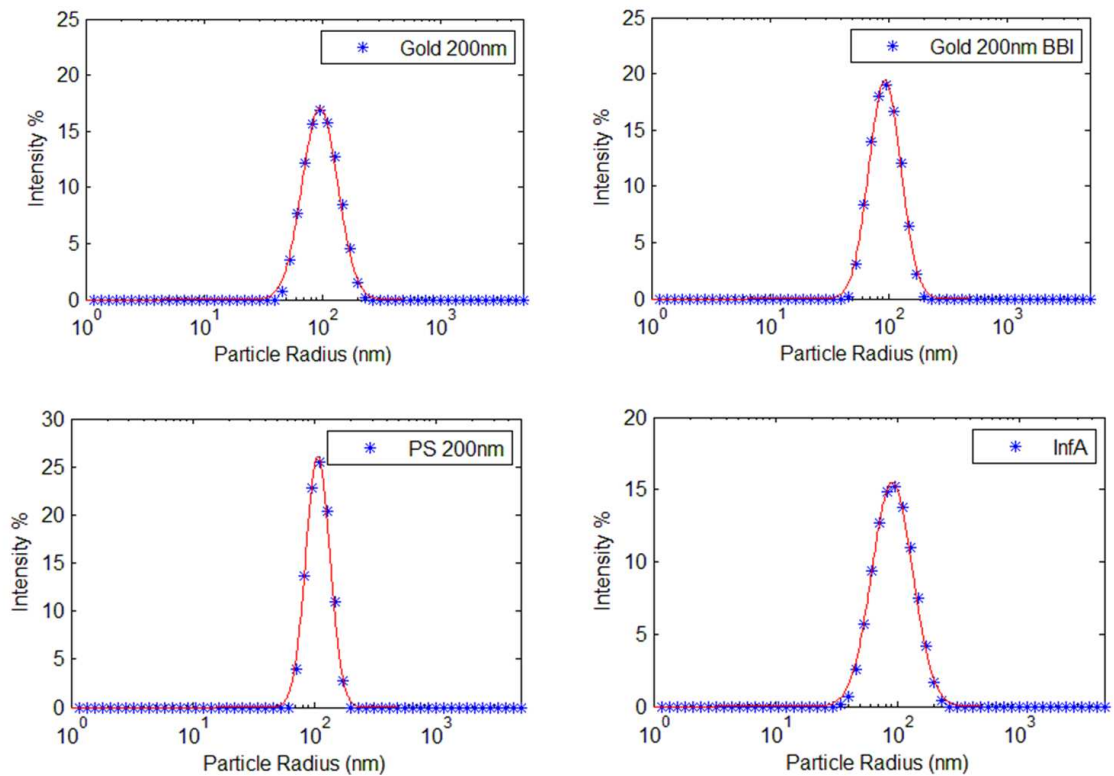
Figure 4.15: DLS measurement of gold, PS nanoparticles with radius of 100nm and Influenza A virions. The DLS data provided by the manufacturer (British Biocell International) for gold nanoparticles with 100nm radius is shown in top right panel.

size distributions we get from our DLS measurement of PS, gold and InfA virions are given in Fig. 4.15. We also give the DLS measurement provided by the manufacturer (Fig. 4.15, top right panel).

Scanning Electron Microscopy (SEM) measurement of PS, gold particles and InfA virions. The particles at the output of the DMA used in our mode-splitting experiments were deposited onto the resonators. The resonators are then examined using a SEM (JEOL 7001LVF FE-SEM). By processing the acquired images, we measured the size of the particles on the resonators. For each particle type, we measured about 100 particles deposited on the resonator surface and calculated a mean size and a standard deviation. Samples of SEM images taken during these measurements for PS and gold nanoparticles and InfA virions are given in Figs. 4.7, 4.10 and 4.11.

Performance comparison. In Table 4.1, we list the results of size measurements performed by various techniques discussed above. It is worth noting here once more that DLS provides hydrodynamic sizes of particles while all the other methods (SEM, TEM, SMPS and Mode-splitting in resonator) provide the dry sizes. Size estimation in SEM and TEM relies on image processing techniques, in SMPS it relies on electric mobility of particles, and in our resonator based scheme it relies on polarizability estimation from mode splitting spectra. In table 4.1, we also list the TEM measurement data provided by the manufacturers. All the measurement results yield mean values close to each other. However, the standard deviations vary among the measurement techniques. Our SEM measurement results are very close both in mean and standard deviation to those reported by the TEM measurements of the manufacturers. The manufacturer has provided the DLS measurements of R=100nm Gold nanoparticle batch as 93.5nm (31.4%), whereas our DLS measurements yielded 96.0(35.2%) for the same batch. The discrepancy can be attributed to the measurement conditions (e.g., viscosity and ionic properties of the dispersant, temperature, etc.) which affect the hydrodynamic size of the particles.

The particles used in our SEM, SMPS and mode splitting measurements were all deposited using a DMA which selects and output particles of electric mobility falling in a narrow distribution with standard deviation of 5% provided that the particle has spherical shape. Thus, a direct comparison between them is possible. For manufacturer provided PS particles, labeled as 100 nm (Note: manufacturer provided TEM data reports an average radius of 101.5 nm with 2.3% standard deviation for this sample), we obtain mean radii of 100.6 nm, 101.4 nm and 101.2 nm, respectively, using SEM, SMPS and our mode-splitting based measurements. This confirms that our technique has the ability to provide the accurate mean size value. Standard deviations in these measurements were 3.07%, 4.7% and 8.96%, respectively, which are larger than the manufacturer's data. We believe that there is room to improve the standard deviation results obtained by our technique, for example by better control of the experimental conditions (such as fluctuations in the fiber-resonator gap, mechanical fluctuations, etc) and by reducing electrical and curve-fitting noises.

Contrary to DLS which is an ensemble measurement, our technique allows single particle detection and measurement. The state-of-the-art DLS technology has reached to a detection limit of 1 nm (ensemble). Our technique in this early stage can detect

74

and count particles with size down to 20 nm (single), and can measure the size for particles down to 30nm (single). The theoretical studies have confirmed that our technique can reach a detection limit of a few nanometers. The DLS measurements are significantly biased towards larger size or higher scattering particles due to ensemble measurement feature, thus the resulting intensity weighted average can be misleading when the sample under test is polydisperse (e.g., heterogeneous mixture of the same particle type but different size or different type of particles with the same size). In order to extract polydisperse features accurately, prior information on the mixture is crucial. In our technique, on the other hand, each particle is measured one-by-one, and no averaging or weighing function is used. Thus, provided that the components of the mixture have sufficient polarizability difference, the polydispersity of the samples can be verified.

Table 4.1: Performance comparison of different nanoparticle measurement schemes

Radius (CV)	Manu--facturer	SEM	DLS	SMPS	Mode Splitting
PS 100 nm	$101.5\ (2.3\%)^a$	100.6 (3.07%)	107.4 (23.0%)	101.4 (4.7%)	101.2 (8.96%)
Gold 50 nm	$49.4\ (< 8\%)^a$	49.7 (7.8%)	54.0 (35.7%)	50.8 (4.6%)	49.0 (10.8%)
InfA	$45\text{-}55^b$ $54.5\ (11.9\%)^c$ $40\text{-}60^e$	41.4-71.0	91.2 (39.2%)	$—\ ^d$	53.2 (10.3%)

[a] Manufacturer provided TEM data. [b] Reported data from SEM measurement (Vollmer, Arnold and Keng 2008). [c] Reported data from plasmon imaging (Wang et. al. 2010). [d] Since only one DMA system is available to us for measurement of viral particles, we could not perform SMPS measurements for InfA virions (Note: SMPS requires two DMAs). [e] The Universal database of the International Committee on Taxonomy of viruses (ICTVdB, http://www.ictvdb.org/ICTVdB/index.htm).

In Fig. 4.12 of the main text of the manuscript, we present the result of polydispersity test applied to our mode splitting technique using a mixture of gold and PS nanoparticles having average radii 50 nm. It is clearly seen that our single particle detection and measurement technique has the ability to extract the bi-modal feature of the mixture. We applied a similar test to our DLS system using (1) a mixture of
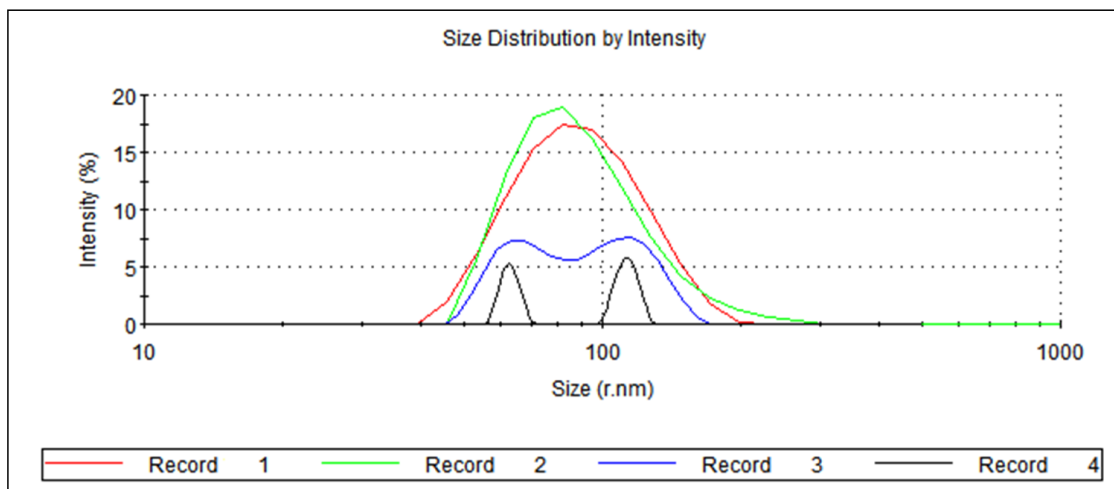
Figure 4.16: DLS measurement of a mixture of PS particles with radii 50 nm and 100nm. Refer to Table 4.2 for the measurement settings of records 1-4.

PS and gold nanoparticles having radii 50 nm and (2) a mixture of 50 nm and 100 nm PS particles. Since the size measurement algorithm used in the DLS measurement relies on the solution of an inverse-problem, it is clear that one should be careful in the data processing not to induce artificial errors. This heterogeneous mixture should appear as a distribution with two distinct peaks. For the test (1) DLS could not resolve separate peaks regardless of the parameter settings available in our system. The result of test (2) is depicted in Fig. 4.16 for various settings of the data processing algorithm. In the default setting of the system, only a large distribution with a single peak appeared. Changing the settings from default to default multi-narrow mode did not change the single peak feature. Then using the customized settings and changing the number of size classes and the size limits, we could observe distributions with two peaks. This, as has been stated in the manual of the DLS system, implies that to get the correct distributions for heterogeneous mixtures, one needs to have priori information on the type of the mixture.

It is generally accepted that DLS has a resolution ratio of 1:4, that is the larger particle in the mixed population should have 4 times bigger size than the smaller particle, i.e., DLS will have problem in resolving a mixture of 50 nm and 100 nm but will resolve a population of 50 nm and 200 nm particles. Our mode-splitting based measurement technique, indeed have performed better than the DLS system by discriminating mixture of 50 nm Gold and PS particle just by sorting them according

76

Table 4.2: Settings used in Fig. 4.16 for DLS measurement

	Record 1	Record 2	Record 3	Record 4
Settings	Default general	Default Multi Narrow Modes	Customized	Customized
Resolution	Normal	High	High	High
# size classes	70	70	70	300
Lower size limit	0.4	0.4	10	10
Upper size limit	10000	10000	1000	1000
Peak1 (width)	91.6(28.1)	92.4(32.9)	110.4(19.16)	113.1(6.12)
Peak2 (width)	-	-	66.95(9.375)	62.8(2.92)

to their polarizability without the need for apriori information about the mixture. A straightforward calculation shows that 50nm spherical Gold nanoparticles have about the same polarizability as 75 nm PS particles. This indicates that our mode splitting based measurement system should be able to resolve 50 nm and 75 nm PS particle mixtures, which is impossible for DLS.

The sizes of InfA virions given in Table 4.1 correspond to the size of spherical particles having the similar equivalent values of hydrodynamic mobility, polarizability or SEM image dimensions depending on the measurement method used. Here, too, results of DLS measurement stand differently from those of the other methods, since it measures the hydrodynamics size of virions. The result of the mode splitting based measurement on InfA is consistent with that of the SEM measurements and those reported in the literature.

4.4.3   Detection and Sizing Efficiency

In Fig. 4.17, we present the simulation results for frequency splitting, changes in the frequencies and linewidths of the split modes and the splitting quality (ratio of frequency splitting over average linewidth of the split modes) for random depositions of PS particles of $R = 50$ nm, using the multi-scatterer model proposed above. The frequency and linewidth of the split modes are continuously changed by the attached nanoparticles, so do the frequency splitting and splitting quality. It is seen that the arriving particle may lead to an increase or decrease in the amount of splitting as well
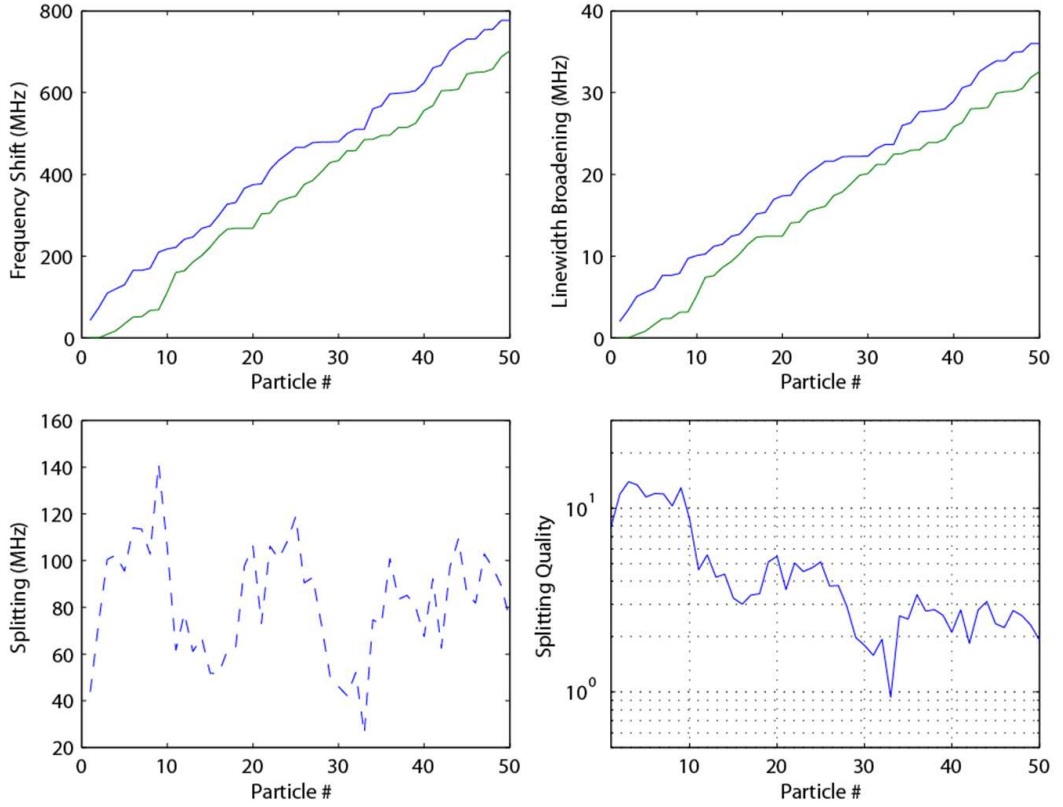
Figure 4.17: Simulation results using the multi-scatterer theoretical model. PS nanoparticles with diameters of 100 nm are continuously and randomly deposited onto a microtoroid with $V = 600\mu m^3$ and $0.05 < f(\mathbf{r}) < 0.36$. Initial Q factor is 10^8

as in the linewidth difference of the split modes. This reflects the position dependence of the amount of mode splitting and linewidth broadening as denoted by Eqs. 4.9 and 4.10 where the term $cos(2\psi_{Ni})$ depends on the azimuthal locations of particles, and g_i and Γ_i depend on the polar locations of particles. Since particle locations are random, fluctuations appear in frequency and linewidth.

It is also clear that both the linewidth broadening and the amount of splitting have an increasing trend as the total number of particles in the mode volume of the resonator increases (see Eqs. 4.9 and 4.10). To probe the fundamental relation between splitting amount and particle number, we eliminate the randomness in splitting by averaging the results of 500 simulations, as shown in Fig. 4.18. It is seen that the splitting amount increases with particle number whereas the splitting quality first increases and then starts decreasing with increasing particle number. These simulations
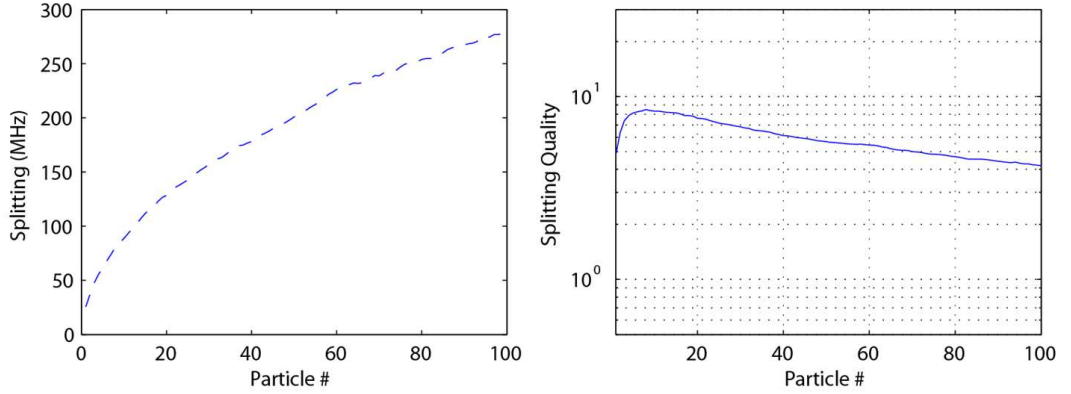
Figure 4.18: Simulation results showing the average value of frequency splitting and splitting quality for 500 times of simulations. In each round of simulation, 100 PS nanoparticle (with diameters of 100 nm) are randomly deposited onto a microtoroid with $V = 600\mu m^3$ and $0.05 \leq f(\mathbf{r}) \leq 0.36$. Initial Q factor is 10^8

only consider scarce coverage situation (i.e. particle number $\ll$ number of particles required to fully cover the surface of the resonator).

Number of particles that can be detected/sized We performed numerical simulations by placing 1000 PS particles of R = 50 nm at random locations in the mode volume of a microtoroid with $Q = 10^8, V = 200\mu m^3$ and uniform distribution for $0 \leq f(r) \leq 0.36$. We consider a particle detectable when the average shift induced by the particle is larger than 2% of the average linewidth of split modes, and a particle is measurable (sizable) when the particle induced change in both the average frequency and linewidth of split modes is more than 2% (1/50 of the average linewidth). Imposing these criteria, our simulations yielded a detection rate 70%, i.e., 700 particles were detected, and > 40 particles were measured. The undetected particles land in the insensitive area of the resonator mode volume where $f(\mathbf{r})$ value is too small. These numbers are valid only for the scenario considered in our numerical simulations. In practice, they may vary with the properties of the particles and resonators used as well as the specific particle deposition technique. Results of this numerical study are given in Fig. 4.19 which shows that each particle detection event leads to fluctuations in both the frequency splitting and the splitting quality. It is also seen in Fig. 4.19 that as the number of detected particles increases, the splitting quality shows a decreasing tendency and at some critical value of the particle number its value drops

79
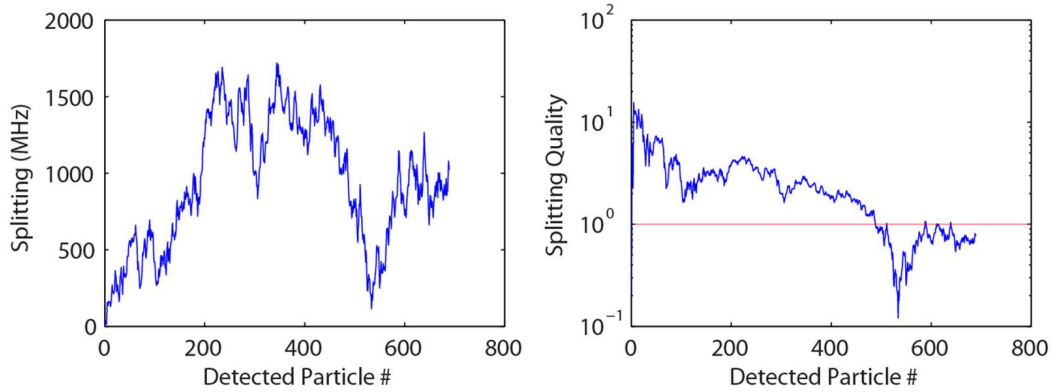
Figure 4.19: Splitting and splitting quality as a function of the number of detected particles. 1000 PS nanoparticles with diameters of 100 nm are continuously and randomly deposited onto a microtoroid with $V = 200\mu m^3$ and $f(\mathbf{r}) \leq 0.36$. Initial Q factor is 10^8

below one, implying that the mode splitting is not resolvable anymore. This puts a limitation on the number of measurable particle number.

We further probed this issue by performing numerical simulations for various values of Q factor and particle sizes. Simulations were performed by depositing 100 or 1000 particles. The results are given in Fig. 4.20. It is clear that both the number of detected and the number of accurately measured particles increases with increasing Q-factor. The number of particles deposited (100 or 1000) does not cause a significant change in the number of measurable particles. A closer look at the simulations reveals that the majority of the accurately measured particles are those within the first 100 deposited particles. It is also seen in Fig. 4.20 that increasing the Q-factor beyond a threshold value, which depends on the particle size, does not lead to significant change in the number of detectable particles. For example, in Fig. S10, this threshold Q value is 10^7 for $R = 60$ nm, and 10^8 for $R = 40$ nm.

Detecting smaller particles requires higher Q values. For example, in the left top panel, we see that the number of detected particles with smaller R is lower than that for larger R when $Q = 10^6$. However, this trend reverses as Q increases; the detectable particle number becomes higher for smaller particles with $Q = 10^8$. This can be understood with the fact that smaller particles induce less Q degradation which helps to detect more particles. Since larger particles induce larger changes in the frequency splitting and linewidths, it is easier to measure their sizes. For example,
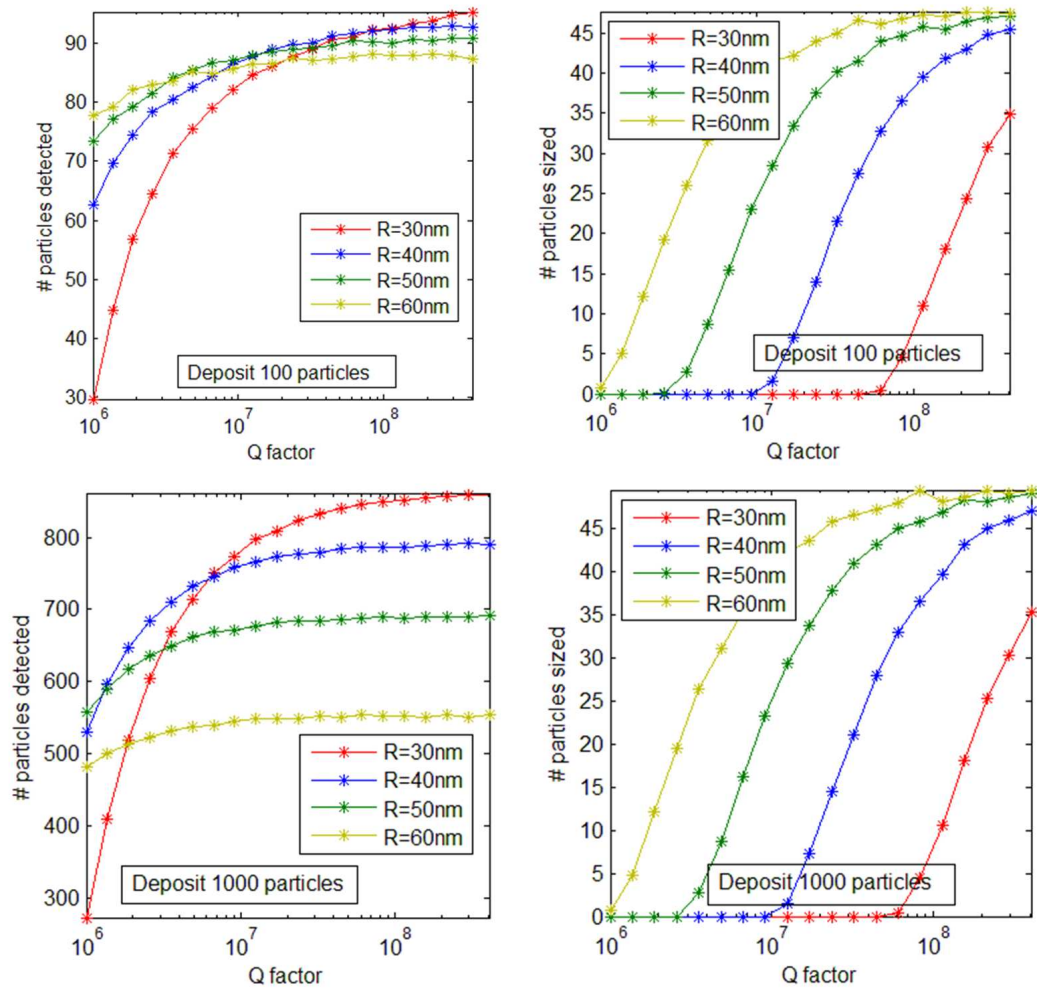
Figure 4.20: Simulated number of particles that are detected and sized, as a function of Q factor and particle sizes. Each date point represents an average value from 100 simulations with the same parameters. In the top two panels, 100 particles are deposited, and in the lower two panels, 1000 particles are deposited.

81

as seen in Fig. 4.20 right panels, Q values as small as 10^7 is sufficient to accurately measure particles of $R = 50$ nm. However, measuring particles of $R = 30$ nm requires Q values around 10^8.

In this scheme, detection of a particle requires an observable change in the frequency or the linewidth of one or both of the split modes. Size measurement, on the other hand, requires accurate measurement of both the linewidth and frequency changes of both split modes, thus size measurement is a more difficult task. Hence, the number of particles detected and the number of particles detected and accurately measured are different, the latter being smaller than the first. The higher the Q, the higher the number of particles that can be detected and measured with a single resonator. These simulation results are in agreement with our experimental observations. In experiments, we can measure as many as 40-50 particles with a single resonator, while hundreds of particles can be detected, without cleaning of the resonator.

4.4.4 Ensemble Measurement

If all the particles deposited on a resonator are the same (having the same or very similar polarizability α), we have

$$\frac{\Gamma_i}{g_i} \approx \frac{\Gamma_j}{g_j}, \forall i, j \leq N \tag{4.13}$$

Subsitituting it into Eq. 4.9 and 4.10 gives us:

$$\frac{\varrho_N^-}{\delta_N^-} = -\frac{\Gamma_i}{g_i} \tag{4.14}$$

Therefore

$$\alpha_{eff} = \frac{\varrho_N^-}{\delta_N^-} \frac{3\lambda^3}{8\pi^2} \tag{4.15}$$

This means that one can use the ratio of linewidth difference over splitting to calculate the "average" (or effective) size of particles deposited on the resonator, if all particles have the same polarizability. To evaluate the robustness of this ensemble measurement

method, we performed simulations by depositing 100 PS particles with mean radius R = 50 nm and coefficient of variation (c.v., ratio of standard deviation to mean value) of 3%, 5% and 10%. After each particle deposition, Eq. 4.15 is applied to calculate the effective size. The results are given in Fig. 4.21 The effective size fluctuates around the mean radius of 50 nm in all three cases, and as expected the fluctuations are larger for the particle ensembles with larger CV.

Indeed, during a continuous deposition of nanoparticles, mode splitting spectra at any instant is related to the effective polarizability of already deposited nanoparticles. If we assume that N-particles are deposited to the mode volume of the resonator and the history of the mode splitting spectra is not available, then we can assign an effective polarizability α_{eff} felt by the resonator using

$$\alpha_{\text{eff}} = -\frac{3\lambda^3}{8\pi^2} \frac{\varrho_N^-}{\delta_N^-} = -\frac{3\lambda^3}{8\pi^2} \frac{(\gamma_N^+ - \gamma_N^-)}{(\omega_N^+ - \omega_N^-)} \tag{4.16}$$

If all the deposited particles are the same, α_{eff} of Eq. 4.16 corresponds to the polarizability of a single particle. For verification, we used the data presented in Fig. 4.8 for InfA virions. The calculated size using Eq. 4.16 is given in Fig. 4.22. The result coincides well with the sizes of single virions acquired in Fig. 4.8g. Notice that the noise level decreases as the splitting quality Q_{sp} increases (Fig. 4.8f). This method of size estimation requires that all the particles on the resonator have very similar sizes and materials, and the mode splitting has decent quality. For example, the effective polarizability of a virus ensemble coated onto a resonator pre-treated with specific antibody receptors can be measured using this approach. Selectivity of virus-antibody binding will greatly influence the accuracy of this scheme.

It is worth noting here that $\delta_N^- > \varrho_N^+/2 + \gamma_0$ should be satisfied in order to observe the mode splitting after the deposition of the N-th scatterer. Since each additional scatterer increases the linewidths, at some point the mode splitting quality $Q_{sp} = \delta_N^-/(\varrho_N^+/2 + \gamma_0)$ may become less than one (with larger particles, fewer particles are needed to reach this point). Consequently, mode splitting cannot be resolved. On the other hand, in some situations the initial Q-factor is too low to observe splitting. However, even in such cases, one may still be able to extract useful information if we assume that mode splitting is much smaller than the individual linewidths $\omega_N^+ - \omega_N^- \ll \gamma_N^-, \gamma_N^+$, and the two resonances have similar linewidth $\gamma_N^- \approx \gamma_N^+$. In
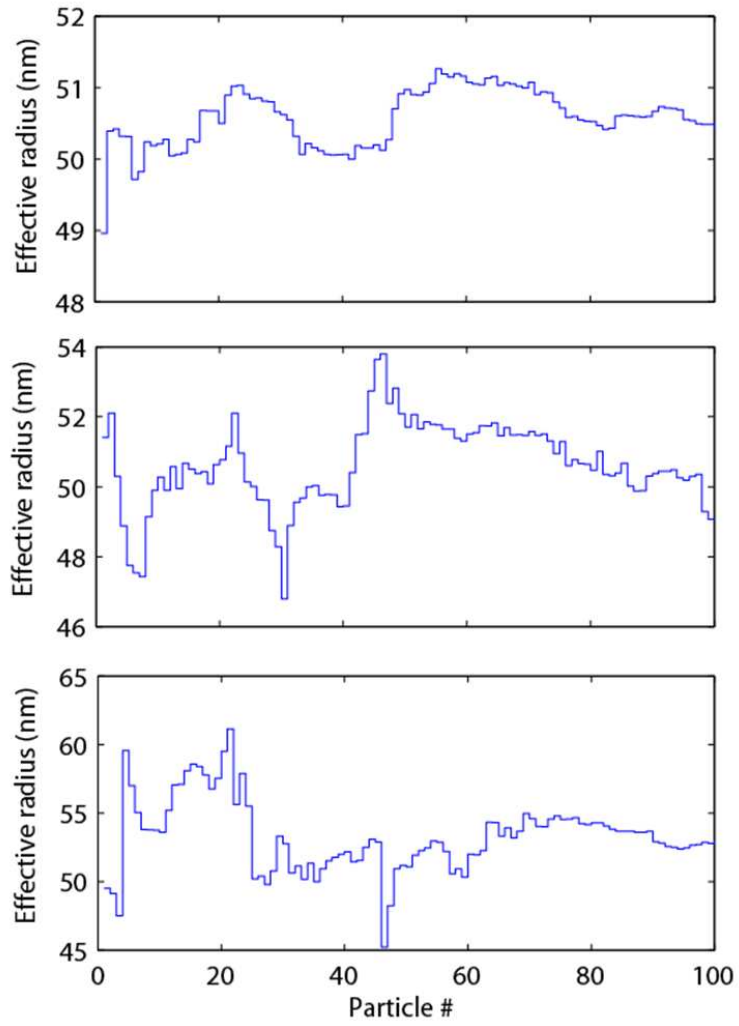
Figure 4.21: Simulations of measurement of effective radius for mean radius R=50 nm PS particle ensembles with coefficient of variations (ratio of standard deviation to mean value) of 3% (top panel), 5% (middle panel) and 10% (bottom panel).
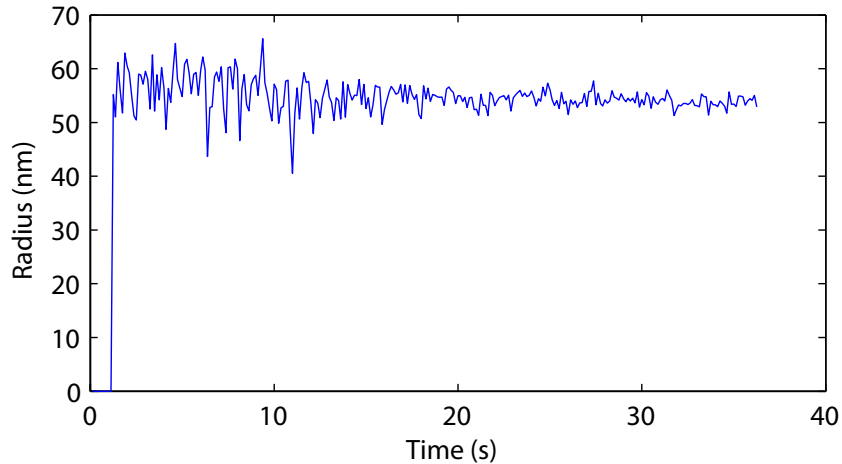
Figure 4.22: Estimation of the size of InfA virions by applying Eq. 4.16 on the data in Fig. 4.8. The fluctuations in size estimation decreases as the splitting quality Q_{sp} increases (Fig. 4.8f)

such a case, the transmission spectrum will show a single lorentzian peak with a linewidth of $\gamma_N = \sqrt{\gamma_N^- \gamma_N^+} \approx (\gamma_N^- + \gamma_N^+)/2$ and a resonance at $\omega_N \approx (\omega_N^- + \omega_N^+)/2$. This expression then can be used with Eq. 4.11 to calculate the polarizability of the N-th particle, given that the linewidth change can be measured for a single resonance peak. Please also see chapter 3 for the discussion of the possibility using non-split mode for particle polarizability (size) measurement.

4.4.5 Summary

We have shown that adsorption of individual viruses and nanoparticles leads to discrete changes in the mode splitting spectra of a WGM microcavity. We developed an accurate and efficient method to detect and measure individual nanospecies one-by-one as they are adsorbed in the mode volume of a microresonator and experimentally verified it using InfA virions, PS and Au nanoparticles of various sizes. We achieved this by developing a theoretical model and measurement strategy which take into account the effect of multiple scatterers deposited on an optical WGM resonator. This approach works equally well regardless of whether there is intrinsic mode splitting or whether a particle is deposited in the resonator mode volume before the actual measurement starts. The particles are characterized accurately regardless of their

positions in the mode volume without the need for complicated processes such as stochastic analysis or excitation and tracking of multiple resonant modes. Moreover, this method is capable of identifying the modality of mixtures of nanoparticle ensembles. Thus, the proposed single nanoparticle measurement technique provides a suitable platform for real-time and highly sensitive detection and sizing of individual nano-sized particles and larege biological particles.

Since nanoparticle induced mode splitting has been demonstrated in water (Kim et.al. 2010), the techniques developed here could be effectively extended to aqueous environment and incorporated into microfluidic or lab-on-chip devices which will pave the way for detecting and sorting of single bio- molecules/particles based on their polarizability or size. Further improvements in detection and size measurement limits could be made by improving the fiber taper stability, using frequency noise reduction methods (e.g. Lu et.al. 2011), as well as employing gain-media doped microresonators (He et.al. 2011).

Chapter 5

Non-Spectrogram Based Single Nanoparticle Detection

The methods described in the last two paragraph are based on monitoring the changes in spectra of the resonator-particle system. A tunable laser is required to achieve the real-time operation. At the data rate of 10 frames per second, it also require the data capturing system to have enough capability to transfer a large amount of data in given time. Although very high sensitivity and particle sizing ability is achieved. These requirements place significant hinderance on making the sensor compact and cost effective. We developed two techniques that are based on power measurements, which in principle do not require a tunable laser. The first technique is based on the back reflection induced by nanoparticles in a microresonator. Note that this idea has been previously reported in literatures through the configuration of add-drop filter (Koch et.al. 2009, Haddadpour and Yi 2010). Although in the prototype experiment we still used a tunable laser, method are available to replace it with a laser diode which can be thermally locked to a resonance (McRae et.al. 2009), which is sufficient to conduct the reflection power measurements. The second technique is based on the drop of transmission of a tapered fiber upon particle binding in the taper waist region. This scheme is very simple and easy to implement, but provides good sensitivity.
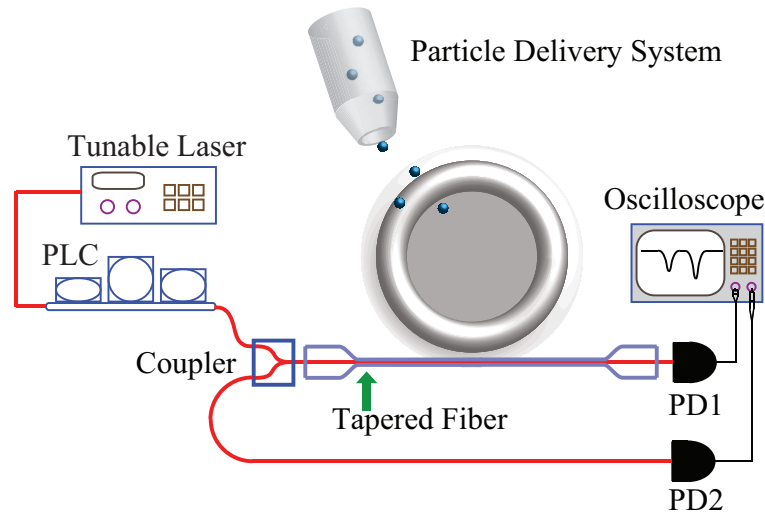
Figure 5.1: The experiment setup for back-reflection based nanoparticle detection. The particle delivery system has been described in Chapter 3.

5.1 Reflection Based Nanoparticle Detection in Microresonators

Nanoparticles can induce mode splitting in a microresonators. It effectively couples the two counter-propagating modes. Therefore the power in the original forward propagating direction is coupled into the backward direction. It allows us to receive light in the back-reflection port. Fig. 5.1 describes the experiment setup. Initially when there is no particles on the microtoroid, only counter clock-wise (CCW) mode exist and PD_2 receives no light. When particles are adsorbed onto the surfaces of the microtoroid, they induced mode splitting and clock-wise (CW) mode is excited and coupled back to the fiber taper in the back-reflection direction. This process can be monitored by PD_2 in real-time.

5.1.1 Nanaoparticle Induced Back Reflection

According to the formulation in Chapter 3 and 4 and defining the eigenmodes (or standing wave modes) of the resonator as $a\pm$, we find that in steady-state regime the two eigenmodes can be expressed as:

$$(-i(\Delta - 2g_+) + \frac{\kappa_0 + \kappa_1 + 2\Gamma_+}{2})a_+ + \sqrt{\kappa_1}a_+^{in} = 0 \tag{5.1}$$

$$(-i(\Delta - 2g_-) + \frac{\kappa_0 + \kappa_1 + 2\Gamma_-}{2}]a_- + \sqrt{\kappa_1}a_-^{in} = 0 \tag{5.2}$$

where $\Delta = \omega - \omega_c$ denotes the lase-cavity detuning. $2g\pm$ and $2\Gamma\pm$ are given as:

$$2g_- = \sum_{i=1}^{N} 2g_i \cos^2(\psi_{Ni}), \quad 2g_+ = \sum_{i=1}^{N} 2g_i \sin^2(\psi_{Ni}) \tag{5.3}$$

$$2\Gamma_- = \sum_{i=1}^{N} 2\Gamma_i \cos^2(\psi_{Ni}), \quad 2\Gamma_+ = \sum_{i=1}^{N} 2\Gamma_i \sin^2(\psi_{Ni}) \tag{5.4}$$

where $\psi_{Ni} = \phi_N - \beta_i$. They are the frequency shift and linewidth broadening of the $a\pm$ modes. From Eq. 5.1 and 5.2 we can write the rate equations for CW an CCW modes:

$$\frac{da_{CW}}{dt} = -[i(\omega_c + g_- + g_+) + \frac{\Gamma_- + \Gamma_+ + \kappa_0 + \kappa_1}{2}]a_{CW}$$
$$-(i(g_- - g_+) + \frac{\Gamma_- - \Gamma_+ +}{2})a_{CCW} - \sqrt{\kappa_1}a_{CW}^{in} \tag{5.5}$$

$$\frac{da_{CCW}}{dt} = -[i(\omega_c + g_- + g_+) + \frac{\Gamma_- + \Gamma_+ + \kappa_0 + \kappa_1}{2}]a_{CCW}$$
$$-(i(g_- - g_+) + \frac{\Gamma_- - \Gamma_+ +}{2})a_{CW} - \sqrt{\kappa_1}a_{CCW}^{in} \tag{5.6}$$

Substituting Eqs. 5.3 and 5.4 into Eqs. 5.5 and 5.6 we have:

$$\frac{da_{CW}}{dt} = -[i(\omega_c + \sum_{i=1}^{N} 2g_i) + \frac{\sum_{i=1}^{N}\Gamma_i + \kappa_0 + \kappa_1}{2}]a_{CW}$$
$$-(i\sum_{i=1}^{N} 2g_i \cos(2\psi_{Ni}) + \frac{\sum_{i=1}^{N}\Gamma_i \cos(2\psi_{Ni})}{2})a_{CCW} - \sqrt{\kappa_1}a_{CW}^{in} \tag{5.7}$$

$$\frac{\mathrm{d}a_{CCW}}{\mathrm{d}t} = -[i(\omega_c + \sum_{i=1}^{N} 2g_i) + \frac{\sum_{i=1}^{N} \Gamma_i + \kappa_0 + \kappa_1}{2}]a_{CCW}$$

$$-(i\sum_{i=1}^{N} 2g_i \cos(2\psi_{Ni}) + \frac{\sum_{i=1}^{N} \Gamma_i \cos(2\psi_{Ni})}{2})a_{CW} - \sqrt{\kappa_1}a_{CCW}^{in} \tag{5.8}$$

With input light only in a_{CW}^{in}, at steady state, the field amplitude of back-reflection collected in the fiber can be can be calculated by $\sqrt{\kappa_1}a_{CCW}$, as

$$a_{ref} = \frac{B\kappa_1 a_{CW}^{in}}{B^2 - A^2} \tag{5.9}$$

where

$$A = -[i(\omega_c + \sum_{i=1}^{N} 2g_i) + \frac{\sum_{i=1}^{N} \Gamma_i + \kappa_0 + \kappa_1}{2}] \tag{5.10}$$

$$B = -(i\sum_{i=1}^{N} 2g_i \cos(2\psi_{Ni}) + \frac{\sum_{i=1}^{N} \Gamma_i \cos(2\psi_{Ni})}{2}) \tag{5.11}$$

5.1.2   Sensitivity

It is worth noting that backscattering in the system does not guarantee that mode splitting is observable. To observe mode splitting, the splitting amount has to be comparable or larger than the average linewidth of the two eigenmodes. Therefore it could be easier to observe back reflection in the fiber than to see particle induced mode splitting. On the other hand, an microresonator free of any contaminations should give no or very little back reflection before particle binding. This essentially creates a background free situation to observe particle induced reflection, whose detection limit is constrained by the noise of laser and sensitivity of the photo-detector.

Figures 5.2 and 5.3 present the calculated transmission and reflection spectra for two particle radii $R = 40$ nm and $R = 5$ nm, respectively. In the former case, mode splitting is observable the reflected power is 250 μW with 1 mW of input power. In
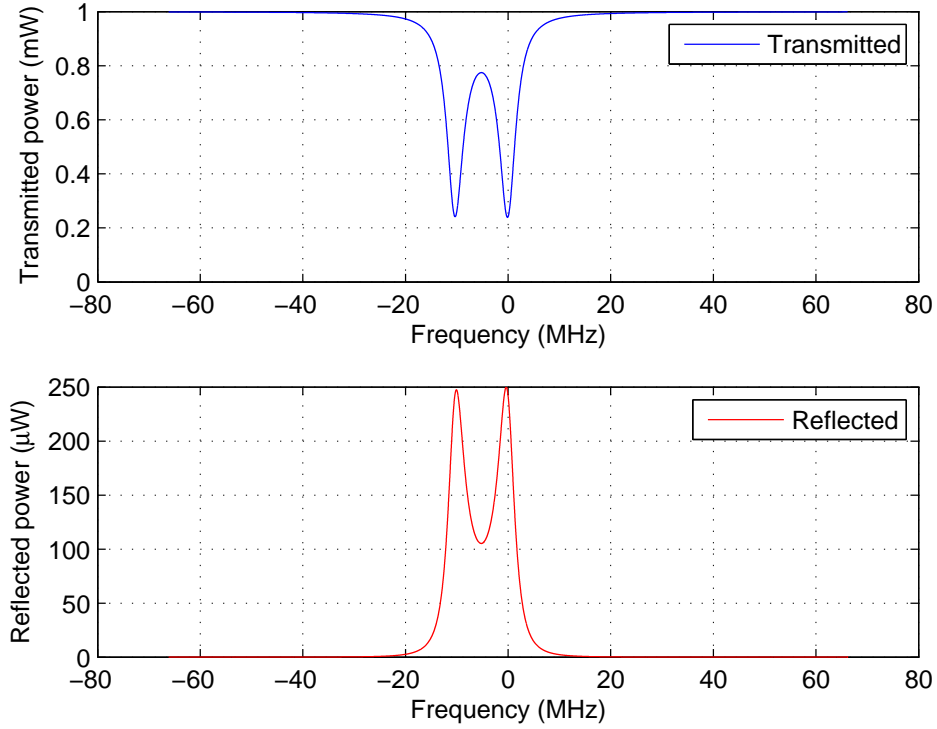
Figure 5.2: Calculated transmission and reflection spectra for 1 mW of power coupled into a resonator. Simulated Q factor is 10^8 and mode volume is $200 \mu m^3$. The particle radius is $R = 40$ nm and its refractive index is 1.59.

the latter case, no mode splitting is visible and the reflected power is much less than the transmission. At 1 mW input about 30 nW of power is reflected, which is large enough for a photo-detector to measure.

From the above examples one can easily see the potential of this scheme, in theory, with a large input power (amplified before sending into the resonator), a shot-noise limited photo-detector and an ultra-high-Q, small mode volume resonator, this scheme can detect a much smaller particles than all the available optical methods. For example if we consider an input power of 10 mW and a photo-detector sensitivity of 1 nW, one can detect a PS particle as small as $R = 1.6$ nm, with a microtoroid with $Q = 2 \times 10^8$.
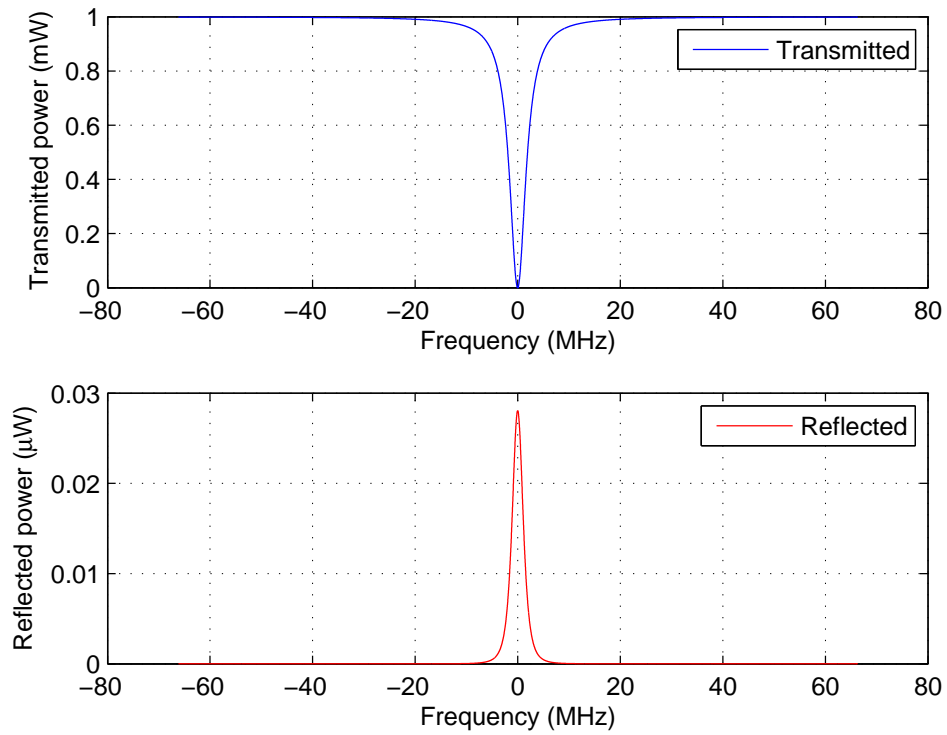
Figure 5.3: Calculated transmission and reflection spectra for 1 mW of power coupled into a resonator. Simulated Q factor is 10^8 and mode volume is $200 \mu m^3$. The particle radius is $R = 5$ nm and its refractive index is 1.59.
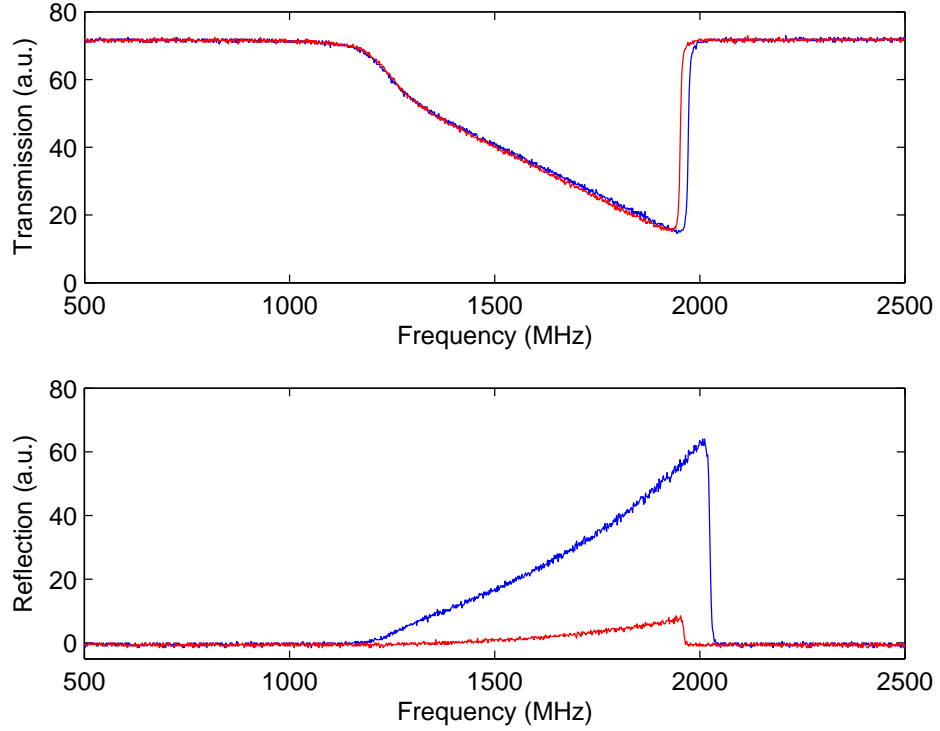
Figure 5.4: Transmission and reflection spectra at time 50 s (blue curve) and 100 s (red curve) after particle deposition started. The triangular shape of the spectra is due to opto-thermal heating of the microresonator during wavelength up-scanning.

5.1.3 Experiments

Using the setup described in 5.1, we first conduct the experiments with PS particles of $R = 50$ nm. The microtoroid we used in this test has Q factor of about 5×10^6. The input power is about 5 mW. Due to the strong on-resonance pumping, the spectra exhibits a triangular shape due to the heating of silica material and red-shift of resonance during wavelength up-scanning (Carmon et.al. 2004). We measured the transmission and reflection mode is at PD_1 and PD_2, respectively.

Figure 5.5 depicts the captured reflection spectra during the first 150 seconds after particle delivery starts. Four discrete changes are seen in the reflection spectra, signalling four particle biding events. Note that in this specific test, the microtoroid has
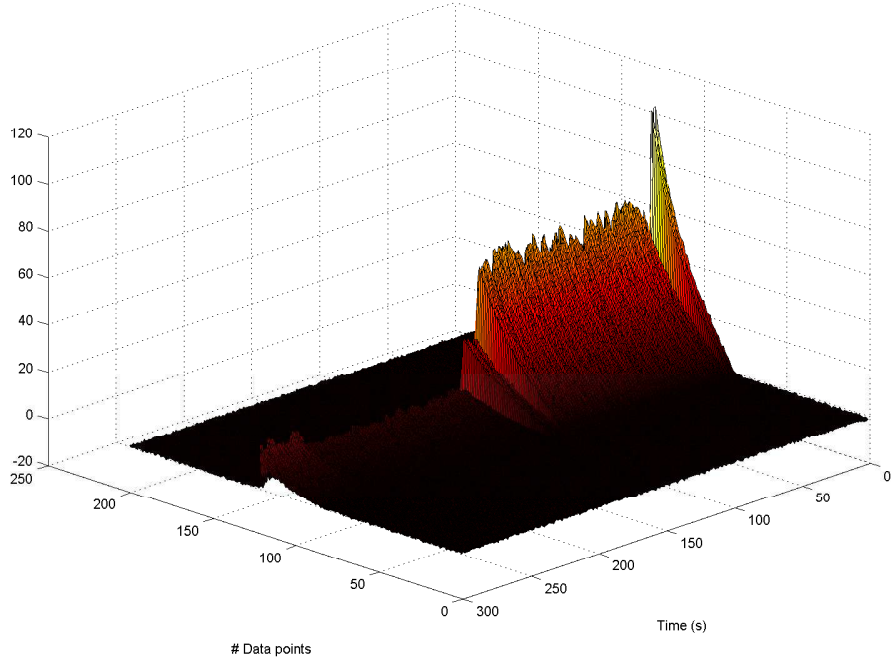
Figure 5.5: Calculated transmission and reflection spectra for 1 mW of power coupled into a resonator. Simulated Q factor is 10^8 and mode volume is $200 \mu m^3$. The particle radius is $R = 5$ nm and its refractive index is 1.59.

initial mode splitting and the reflection before the particle binding is clearly observable. The consecutively deposited particles may increase or decrease the refelection amplitude as indicated by Eq. 5.9, depending on the particle location.

For a clearer presentation we plot the reflection amplitude against time in Fig. 5.6, where the four discrete changes are shown clearly. To further test the sensitivity of the scheme, we tested with $R = 20$ nm Sodium Chloride (NaCl) nanoparticles ($n \approx 1.52$). The results are shown in Fig. 5.7. The Q factor of the microtorid in this test is about 2×10^7.

In these experiments, the major noise source came from the fluctuation of taper-resonator air-gap. It can be induced by mechanical vibration and airflow around the microtoroid and can change the coupling condition of taper and resonator, hence give the reflection amplitude bad fluctuations as seen in Fig. 5.6. To eliminate this noise, one may increase the stability of the coupling by isolating the system or let the taper and resonator to be in contact with each other.
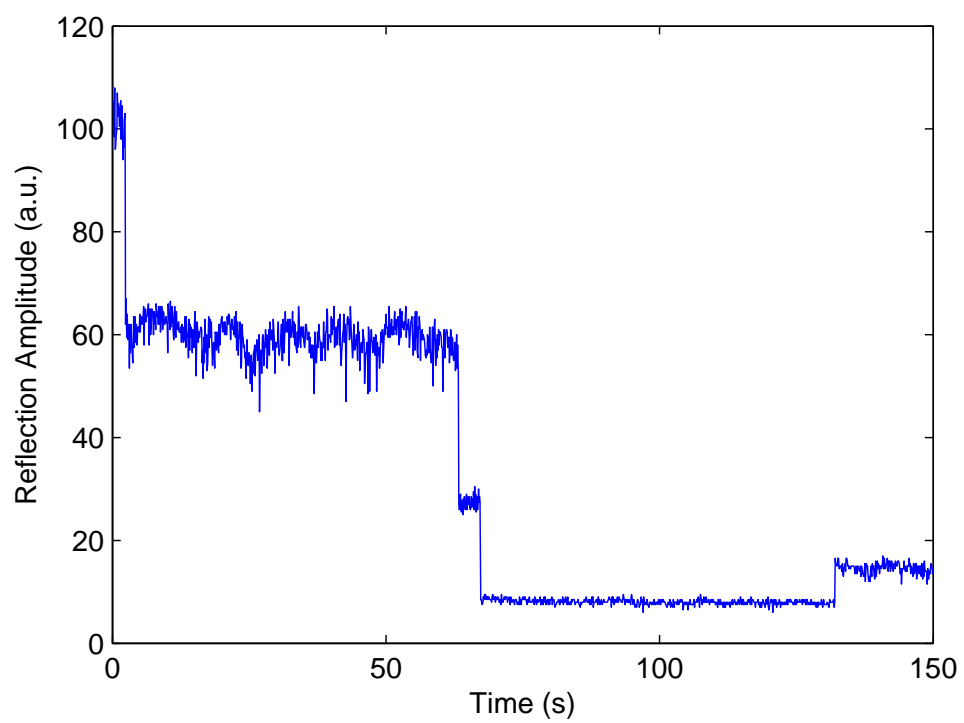
Figure 5.6: Reflection amplitude change showing detection of $R = 50$ nm PS particles.
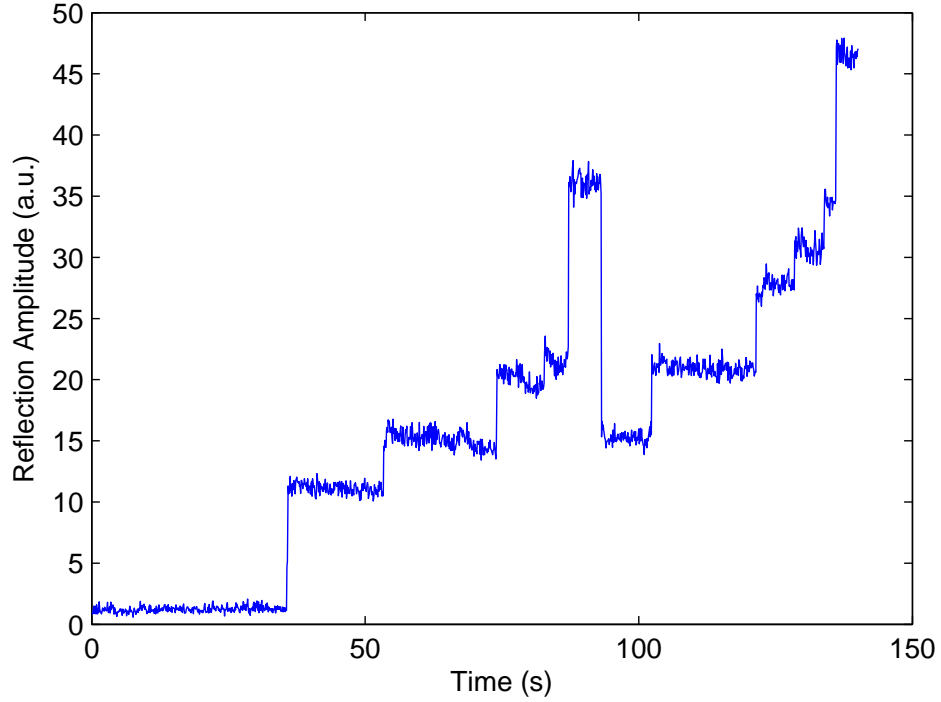
Figure 5.7: Reflection amplitude change showing detection of $R = 20$ nm NaCl particles.

As suggested in both calculations and experiments, the reflection amplitude is maximized when the resonator is at critical or slightly over-coupled conditions (if mode splitting is observable). This scheme is especially suitable for small particles $R < 20$ nm, as mode splitting cannot be easily observed for this particle size range.

In summary, we present the theory and experiments for detecting nanoparticles using the reflection mode in a microresonator. Unprecedented sensitivity could be achieved using this scheme, as indicated by both calculations and the signal-noise-ratio in the initial tests (5.7). Since this scheme is based on power detection, tunable laser is not necessary which will greatly reduce the complexity and cost of the whole sensor system. By further optimizing the experimental conditions, size range below 5 nm will be within reach.

5.2 Fiber Taper Based Nanoparticle Detection

[3]With the progress in nanotechnology, there is an urgent need to develop compact, sensitive and cost-effective sensors for detecting single nano-scale objects, especially for artificial nanoparticles and biological objects in the submicron range. In the past few decades, much effort has been devoted to developing fiber optic evanescent field-based sensors using tapered optical fibers. These sensors have been shown to be very sensitive to changes of the surrounding medium providing a compact, inexpensive and in-line sensing platform for measuring physical parameters such as temperature and refractive index, as well as for quantitatively detecting the concentration of chemical compounds (Brambilla 2009, Villatoro and Monzon-Hernandez 2005).

In this chapter we discuss a sensor consist of a submicron tapered fiber. Detection and ensemble measurement of single R=120 nm and 175 nm polystyrene (PS) nanoparticles are demonstrated in the 1550 nm wavelength band. The detection mechanism relies on the extra scattering loss induced by a single nanoparticle adsorbed on the tapered fiber. According to calculation, lower detection limit down to R = 50 nm can be easily achieved with light source in the visible wavelength band. This will cover the range of many important biological agents such as Influenza viruses. Compared with micro-resonator based nanoparticle detection scheme or other light scattering particle measurement schemes, this method has the advantage of extreme simplicity and good sensitivity. Large scale integration may be achieved by arraying tapered fibers.

5.2.1 Theory

The underlying principle of the proposed sensing mechanism is based on optical scattering of the evanescent field of a tapered optical fiber when a sub-wavelength (Rayleigh) scatterer enters the mode volume. In a single mode fiber, the light propagates as a core mode, i.e., most of the energy is confined within the core. However, as the fiber is tapered down, the core area becomes smaller and light spreads out into the cladding and consequently the core mode adiabatically transforms into a cladding

---

[3]This section has appeared in "Optical Detection of Single Nanoparticles With a Subwavelength Fiber-Taper", Photonics Technology Letters, IEEE, 23, 1346 - 1348 (2011).

mode leading to a highly-confined field at the cladding-medium interface with an evanescent portion in the surrounding medium. This cladding mode is then adiabatically converted back to the propagating core mode after the tapered region. Thus, the tapered region facilitates access to the evanescent field, allowing it to interact with the surrounding medium. Subsequently, making the tapered region susceptible to any perturbations (e.g., changes in refractive index, temperature, humidity, absorbtion, scattering, etc) in the medium.

When a sub-wavelength spherical particle of radius R and permittivity ε_p is placed in the evanescent field $\mathbf{E}_0$ of the tapered region, it will induce a scattering loss which can be described by the field of an induced dipole moment $\mathbf{p} = \alpha\varepsilon_m\mathbf{E}_0$ where $\alpha = 4\pi R^3(\varepsilon_p - \varepsilon_m)/(\varepsilon_p + 2\varepsilon_m)$ is the polarizability of the scatterer and ε_m is the permittivity of the surrounding medium. This scattering loss to the environment will then lead to decrease in the transmitted power at the output port of the fiber. Since the polarizability α is a function of the shape and the size of the particle, and the permittivity (i.e, refractive index) contrast of the particle and the surrounding medium, the loss in the transmission should contain information on these properties of the particle. Thus, monitoring the changes in the transmission, one will be able to detect and quantify the polarizability of the particles entering the evanescent field.

The amount of Rayleigh scattering for a beam of light is dependent on the size of the particles as well as the wavelength of the light. Specifically, the intensity of the scattered light varies as the sixth power of the particle size and varies inversely with the fourth power of the wavelength. The corss-section of a particle in the Rayleigh regime is described by:

$$\sigma_s = \frac{2\pi^5}{3}\frac{d^6}{\lambda^4}\left(\frac{n^2 - 1}{n^2 + 2}\right) \tag{5.12}$$

where d is the diameter of of the particle and n is the refractive index of the particle. Here air is considered as the medium. For a group of Rayleigh particles, in the case of incoherent scattering the scattered power add arithmetically, while for coherent scattering (such as very closely placed particles), interference takes place and the scattered field add arithmetically. The aspect coherent scattering adds complexity

98

Figure 5.8: Results of numerical simulations performed using COMSOL showing the pattern of the electrical field of the light scattered by a nanoparticle adsorbed on a nano-taper. **a,** Without particle. **b,** With particle. The nano-taper has a thickness of $0.8\mu m$ and refractive index of 1.45, light wavelength is 1550 nm and the nanoparticle has refractive index of 1.59 and a radius of 150 nm.

to the analysis for the fiber taper sensor. But for a long fiber taper and scarcely distributed particles on the taper, one may choose to neglect the coherent scattering. As the scattered power decrease with the 2nd power of distance, given enough space between two scatterer, the interference is negligible.

Numerical simulations of electric field around a taper in the presence of a subwavelength nanoparticle clearly show the particle-induced disturbance and the consequent scattering (Fig. 5.8). For different sizes of subwavelength fiber taper, although they all support only a single mode, but the mode index decreases with taper size, and more light is guided outside the silica material. At $\lambda = 1.5\mu m$, when taper diameter D reduces to below 800 nm, the mode pattern starts to polarize. Figure 5.9 clearly shows this transition. The mode index for the three sizes of taper is 1.26, 1.09, 1.024 for the $D = 1\mu m$, $D = 800$ nm and $D = 600$ nm, respectively.

Note that Eq. 5.12 considers the case when the particle is in a uniform medium. When a particle is on the interface between silica and air, its scattering profile will change. In the case of very low fiber mode index (e.g. 1.09 for $D = 800$ nm taper) and relatively particles with relatively high index (e.g. PS particles), Eq. 5.12 is still a very good approximation.

5.2.2 Experiments

A schematics of the set-up used in our experiments is given in Fig.5.10. The tapered fibers were prepared by heating and pulling a standard communication single-mode fiber ($R_{\text{core}} = 4\mu m$ and $R_{\text{clad}} = 62.5\mu m$) above a hydrogen flame. The thickness and length of the waist of the fabricated taper was estimated to be 0.8μm and 3mm, respectively. Light was provided by an unmodulated continuous wave (CW) laser diode with fixed power around $P = 2$mW at wavelength of $\lambda = 1.55\mu$m. The transmitted light power was measured with a photodetector (PD; bandwidth: 125MHz) whose output was then acquired to a computer. Polystyrene (PS) nanoparticles of refractive index $n_s = \sqrt{\varepsilon_s} = 1.59$ of mean radii $R = 120$nm and $R = 175$nm were used to test the performance of the nano-taper sensor for detecting nanoparticles at single particle resolution.
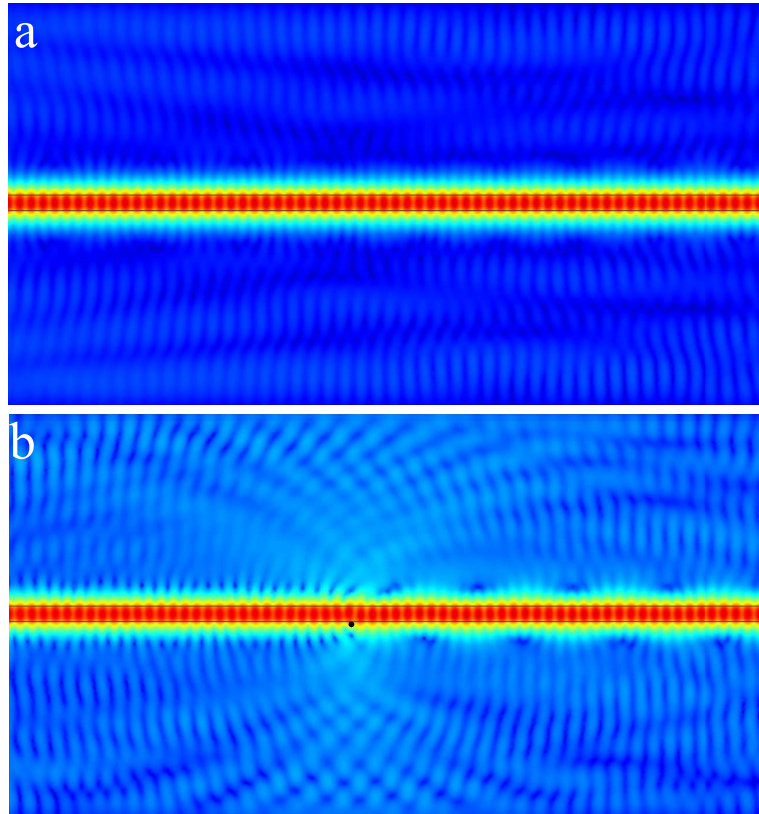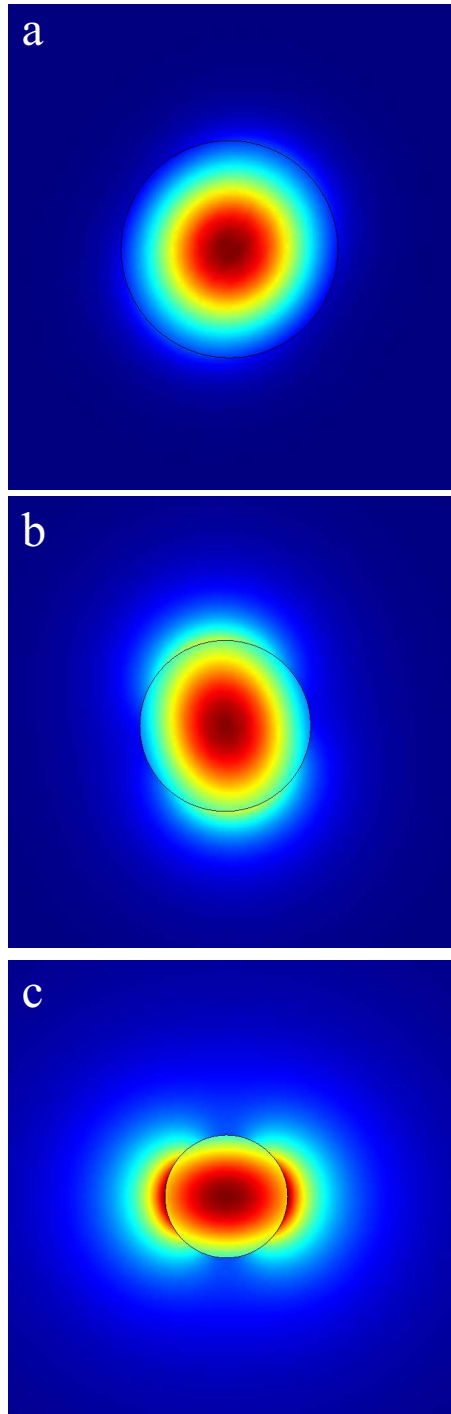
Figure 5.9: Results of numerical simulations performed using COMSOL showing the optical mode pattern of the electrical field of the light inside a subwavelength fiber taper. **a,** Fiber diameter $D = 1\mu m$. **b,** $D = 800$ nm. **c,** $D = 600$ nm. The taper has refractive index of 1.45, light wavelength is 1550 nm.
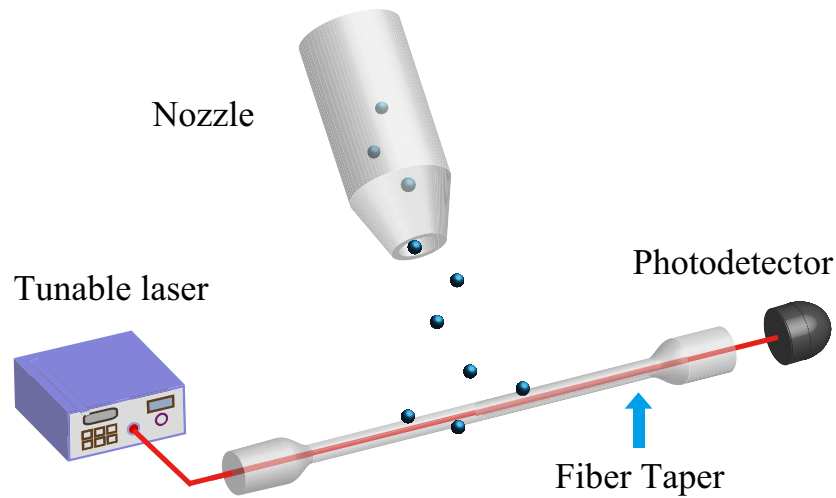
Figure 5.10: Experimental setup for fiber taper nanoparticle detection. A nozzle is used to deliver single particles consecutively onto a tapered fiber.

PS nanoparticles were deposited onto the taper using a set-up which consists of an atomizer, a differential mobility analyzer (DMA) and a nozzle with an inner tip diameter of 80μm. The particles are carried out by compressed air using a collision atomizer and then neutralized by a radioactive source such that they have a narrow charge distribution. The DMA classifies particles according to their electrical mobility, resulting in a narrow size distribution. The filted particles exit through the output slit and are subsequently channeled to the taper waist with a micro-nozzle. The concentration and flow rate of the particle flow is optimized so at the time of detection the average number of particles arriving at the sensing area in 1 second is less than 1.

Figure 5.11 shows the changes in the transmission as a function of time as PS nanoparticles are deposited onto the taper waist section. Each discrete downward jump in Fig. 5.11 signals the binding of a single nanoparticle. Thus, by counting the number of these jumps, one can count the number of particles entering the field of the taper. Height of the jumps, which reflect the effective scattering loss, varies with the 1), position of the particles along the taper waist and 2), their distance from each other. The first is attributed to the slight non-uniformity of the waist diameter which leads to varying local field intensities along the taper. The latter is due to multi-particle coherent scattering and the modification of the local field distribution due to deposited particles. Another important factor worth considering is the dipolization
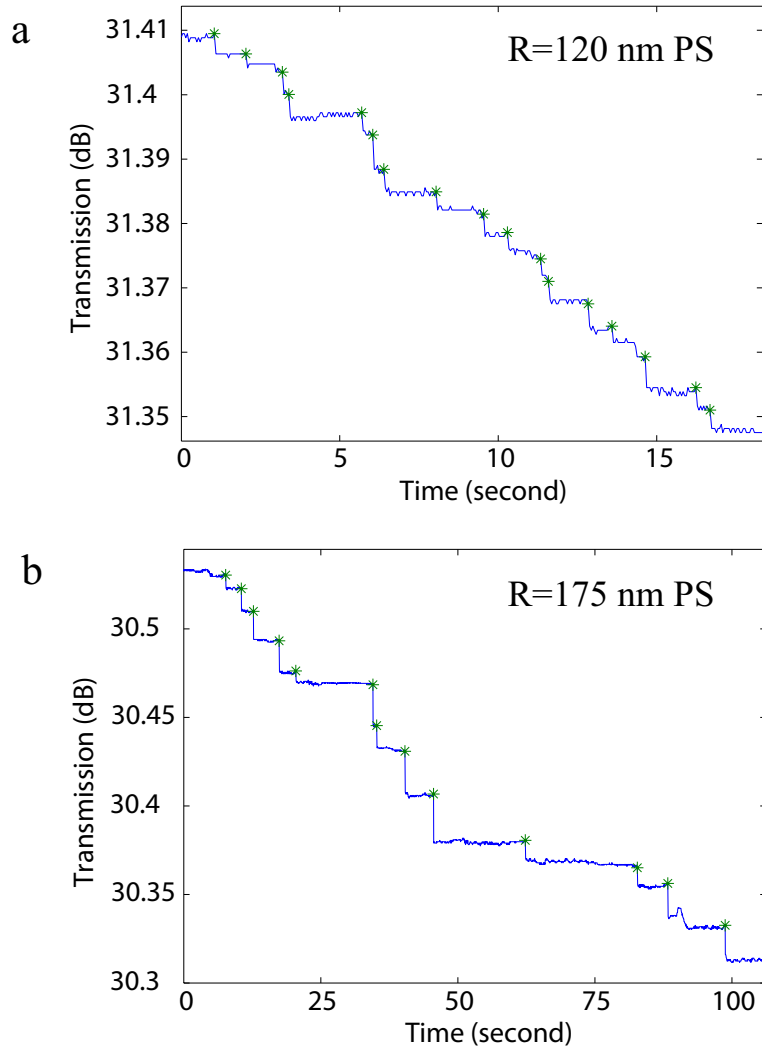
Figure 5.11: The change in the transmission as polystyrene nanoparticles bind to a taper. **a,** $R = 120 \mp 3$nm, and **b,** $R = 175 \mp 4$nm. '*' signs denote the detected particle binding events.

103
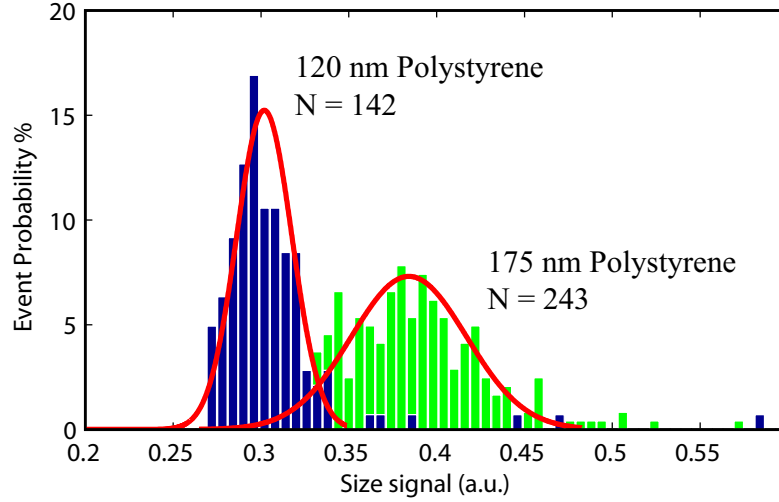
Figure 5.12: Measured size signal ($h^{1/6}$) distributions for polystyrene nanoparticles of $R=120\pm3$ nm (left peak) and $R=175\pm4$ nm (right peak). N denotes the number of particles detected during the experiments.

of the mode pattern (Fig. 5.9b,c), which causes the intensity differences around the surface of taper. It should be noted that the particles falling out of tapered region do not interact with the evanescent field and thus cannot be detected.

It is pointed out that the scattering cross-section and hence the effective scattering loss induced by a sub-wavelength Rayleigh scatterer is proportional to the 6th power of particle size or R^6. Thus, the heights of the jumps in the power transmission carry the information on the particle cross-section or the particle size, despite the other factors causing varying scattering losses. To confirm this, we use $h^{1/6}$ to indicate the particle size where h denotes the height of each discrete jump in the transmission signal. Figure 5.12 shows the recorded distribution of $h^{1/6}$ measured for PS particles of two different sizes. The clear separation of the peaks and the small overlap between the tails of the distributions suggest that the two sizes of particles are well resolved. The standard deviations of the distributions are larger than the nominal deviation provided by the manufacturers mainly due to the reasons mentioned in the last paragraph. The laser power noise and detector noise also contribute to this deviation, especially for the $R=120$ nm case, when particle induced signals are closer to the noise level.
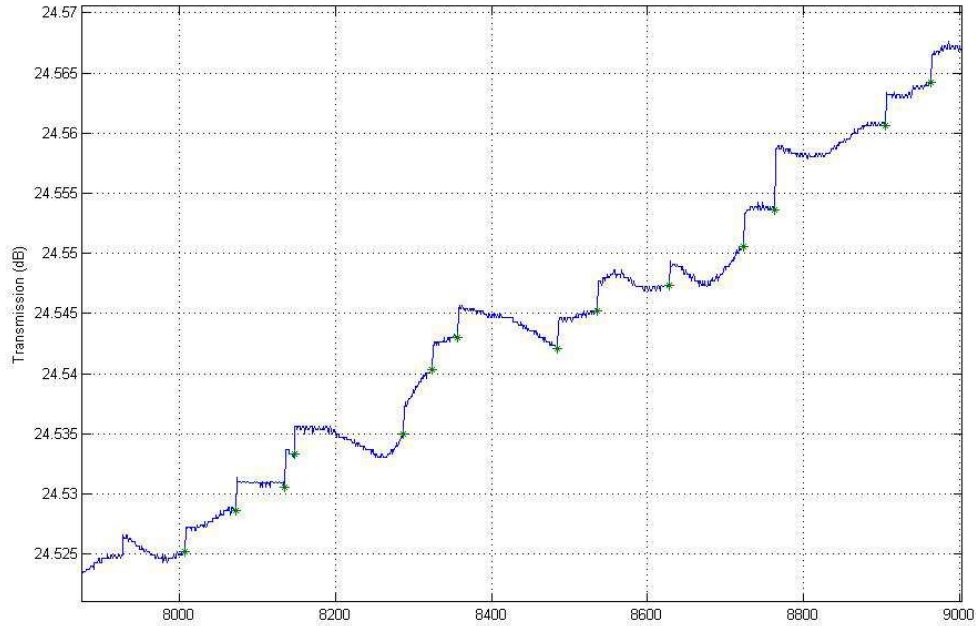
Figure 5.13: The change in the transmission as PS nanoparticles bind to a taper with diameter of about 400 nm. '*' signs denote the detected particle binding events. The gradual drift of transmitted power is due to the movement of fiber taper. The x-axis is the number of data points. The data capturing rate is 10 points/second

One interesting phenomenon in the experiments is that when the taper is thinned much below the wavelength (e.g. $D = 400$ nm at 1550 nm wavelength), the transmission can be considerably lower (e.g. 50%) than the original fiber transmission due to the loss induced by the tapering process. In simulations for a 400 nm taper, the mode is highly dipolized and the evanescent tail extends significantly outside the taper. When using such a taper for particle detection, we actually see the transmission increases upon particle binding (Fig. 5.13). Our explanation for this phenomenon is that the attached PS particles (refractive index 1.59) enhances the taper's ability to guide light within itself, which reduces radiation loss. However a taper of this size does not enhances the detection sensitivity as its mode volume is much larger than a taper around 1 μm, hence it is more difficult to be perturbed.

In summary, we demonstrated real-time detection and counting of single PS nanoparticles using a tapered-fiber with sub-micron taper waist. The proposed scheme does

not need tunable lasers and offers single-nanoparticle resolution, ease of fabrication, low-cost and versatility. Thus, it provides an alternative and competitive platform to existing technologies with comparable sensitivities. We should note here that since the scattering loss scales as λ^{-4}, and taper field cross-section scales as λ^2 (for the same mode index), the sensitivity of the scheme for detecting particles with much smaller size are within reach by replacing the infrared laser source with shorter wavelength lasers, i.e., visible or UV. Moreover, a number of tapered fibers can be fixed together to form an array which will increase the sensing area thus improving particle capturing efficiency.

This detection scheme can be easily applied to planar waveguide structures. In aqueous medium, our method combined with recently developed waveguide particle trapping and transporting techniques (Brambilla et.al. 2007, Schmidt et.al. 2007, Senthil Murugan et. al. 2008, Sheu et.al. 2010) can form a complete nanoparticle detection and sorting platform on a chip. This technology is not limited to the detection of dielectric nanoparticles, but it can be used for the detection of metal nanoparticles and large bio-particles, as well. The selectivity can be achieved by applying recognition coatings on the tapered region.

Chapter 6

Future Work and Conclusions

6.1 Microcavity Lasers and Nanoparticle Detection

With its high quality factor small mode volume, microtoroid is a great device to make low threshold lasers. By incorporating gain medium into the microtoroid, high quality lasers can be generated at threshold as low as a few micro-watts. A general method of incorporating gain medium into silica material is by doping with rare-earth ions, such as Erbium(Er) and Ytterbium (Yb). A very flexible way to dope these ions into silica matrix is by the sol-gel method (Yang et.al. 2005). For Er laser, threshold power less than 1 μW is obtainable.

On the other hand, Raman scattering in silica provides amplification at the stokes band. If an ultra-high-Q microtoroid is pumped with sufficient power, Raman laser can be generated. In silica the maximum Raman gain takes place at a frequency offset of 13.2 THz from the pump. Generally pump power of a few hundred μW is needed to observe Raman laser in microtoroid (Kippenberg et.al. 2004).

Figure 6.1 shows the measured pump and laser output power for a microtoroid Raman laser using an optical spectrum analyzer. The pump wavelength is 1535 nm and Raman laser appears at 1640 nm. Because the raman gain band in silica is over 20 THz wide, it is possible to excite multiple Raman lasers in a microtoroid. If pump power is sufficiently strong, cascaded Raman lasing can occur. This mechanism has been used to generate lasers at a much longer wavelength. To have single mode
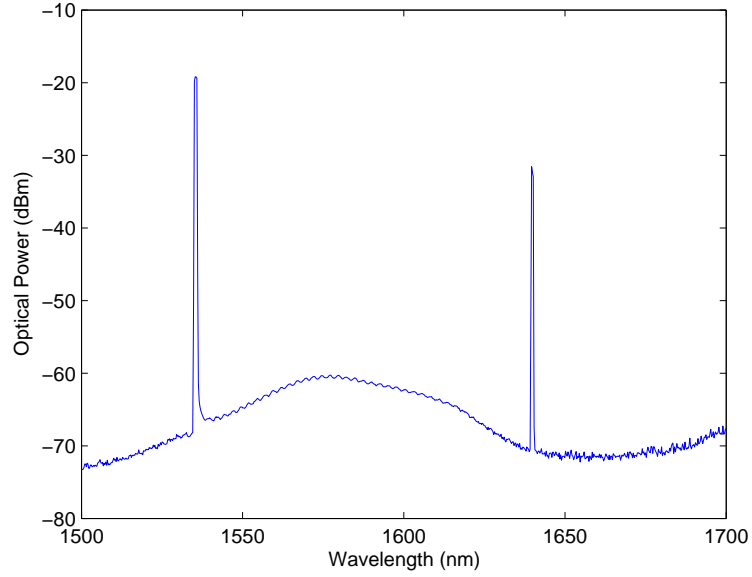
Figure 6.1: Measured Raman laser output power (right peak) and pump power (left peak) for a microtoroid.

operation, one can decrease the pumping power appropriately and tune the taper-resonator coupling condition to maximize the coupling efficiency of one of the lasing mode.

In the presence of mode splitting, the lasing mode splits into two closely spaced mode. Because mode splitting frequency is usually less than 1 GHz, the lasing conditions for the split lasing modes are so close that they always appear in pairs. These two lasers interferes and generate a radio frequency beatnote that has the same frequency as the splitting. Figure 6.2 shows the measured beatnote pattern and measured spectrum for the beatnote signal. The beatnote spectrum clearly shows a peak which corresponds to the splitting frequency.

To quantify the noise level of the splitting frequency over time, we measured the beatnote frequency for a period of time (Fig. 6.3). As seen in Fig. 6.3, the experiment noise is generally smaller than ± 0.1 MHz.

As discussed in Chapter 3 and 4, if the amount of mode splitting can be precisely monitored, nanoparticle detection can be achieved. With a noise level of 0.1 MHz, using the beatnote as the detection method for splitting and nanoparticle adsorption
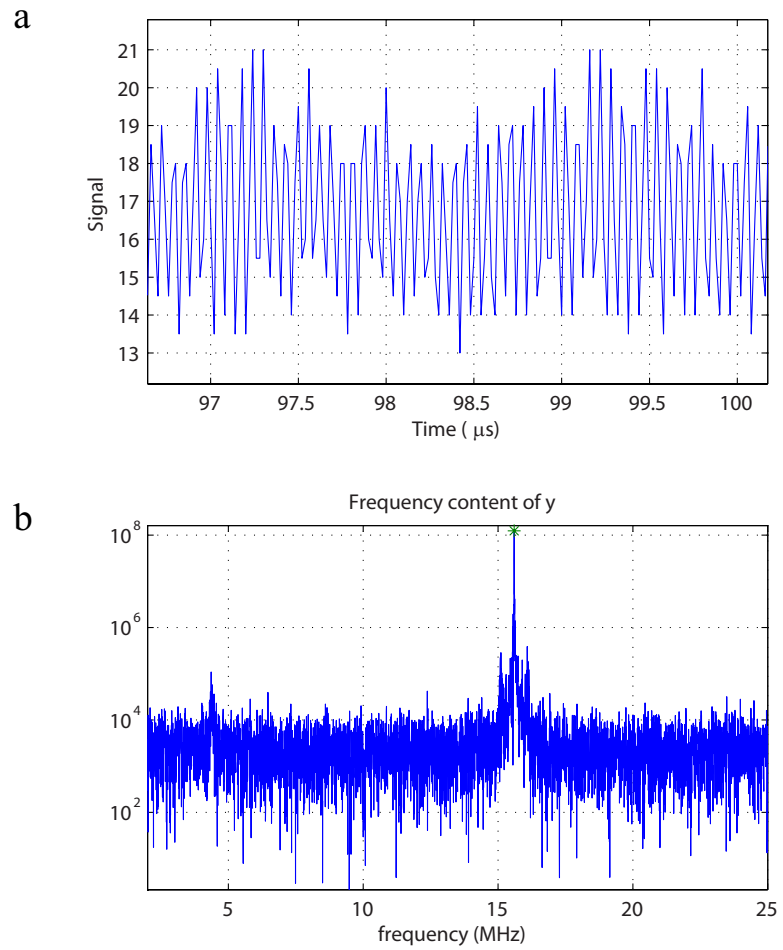
Figure 6.2: Measured beatnote signal (**a**) and its calculated spectrum ($200\mu s$ window) (**b**).
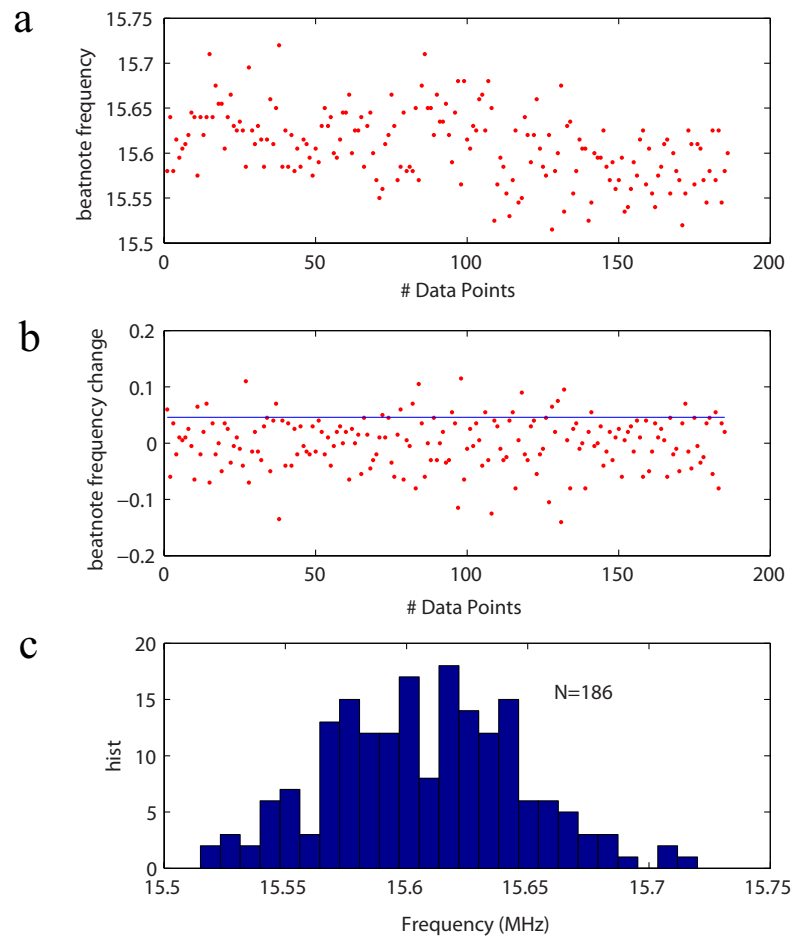
Figure 6.3: Measured noise characteristics for the beatnote frequency. **a,** Measured beatnote frequency for a period of time (# data points N=186). **b,** Measured beatnote frequency fluctuation around its mean frequency showing the deviation of the signal. Blue line shows the level of standard deviation. **c,** Histogram of the beatnote frequency
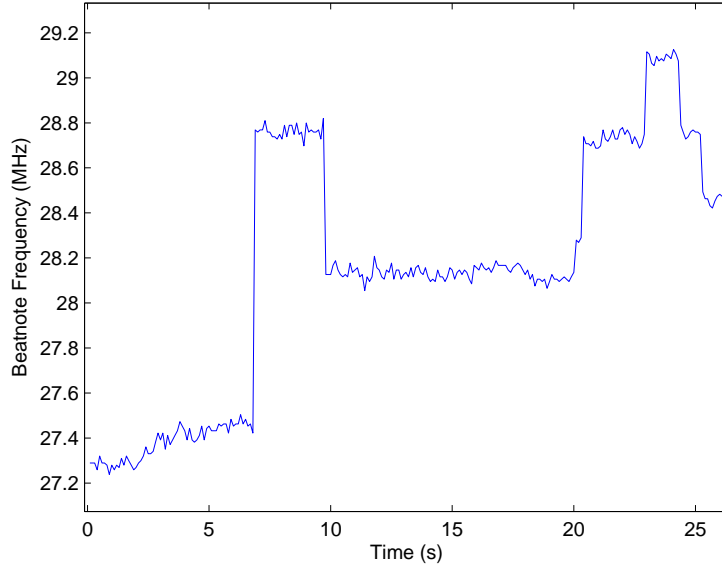
Figure 6.4: Measured beatnote frequency changes when gold nanoparticles of $R = 25$ nm are consecutively deposited. Each step change signals the detection of a particle.

will be very sensitive. Gold nanoparticles as small as $R = 10$ nm has been detected using Erbium laser (He et.al. 2011). Figure 6.4 shows the beatnote change when gold nanoparticles of radii 25 nm are deposited. Each step change in the frequency signals a change in the amount of splitting, hence signals the detection of a nanoparticle. The size information of each particle cannot be measured because the linewidth information can not be extracted from the lasing beatnotes. However if enough number of data points are gathered, one can use the distribution of changes in splitting amount to estimate the average sizes of a particle ensemble.

In theory, the ultimate detection limit is set by the laser linewidth, which is much narrower than the resonance linewidth of any passive resonator. This means that microlaser sensors have the potential to detect objects that are too small to be detected by passive resonator sensors.
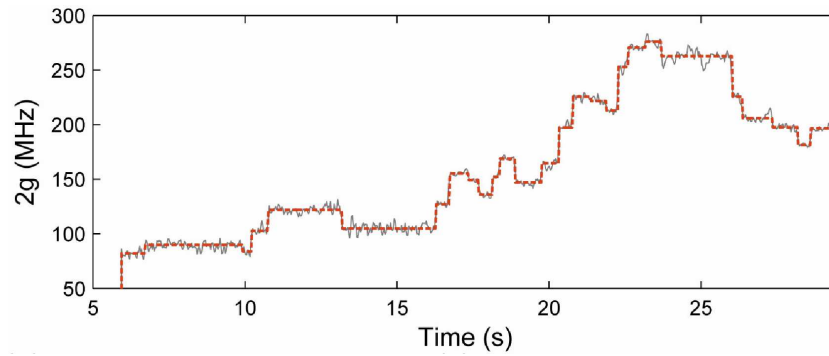
Figure 6.5: Measured mode splitting changes when microtoroid is placed in solutions of PS particle with radii 75 nm. Each discrete change signals a nanoparticle binding event.

6.2 Bio-molecule Detection

The techniques developed in this dissertation are very effective in detecting nanoparticles with sizes from R=10 nm to R=175 nm, which covers the size range of many important biological particles such as protein and viruses. Further improvement in experimental implications will allow tapping into the range of a few nm, which approaches the single bio-molecule level.

One problem associated with bio-molecules is that they are usually in aqueous solutions (water). To bring them to the resonator surface, one has to either submerge the resonator into solution or bring the molecules into dry environment. For the former approach one has to first guarantee that the quality factor of the resonator does not drop significantly in aqueous environment. This requires to use ultra pure water and purified and diluted samples. On the other hand, because water has a refractive index of 1.3, the index contrast between silica microtoroid and the environment is much reduced than in air. To keep similar quality factor it requires to use slightly larger resonator size to decrease radiation loss, which decreases the sensitively of the sensor. The index contrast between the bio-molecules in water is also much smaller than when they are in air. These all place obstacles for using microtoroid as bio-sensor. Progress has been made recently on detecting nanoparticles in water. Q factors above 10^7 has been achieved for microtoroid and mode splitting has been observed and used to detect nanoparticles (Fig. 6.5).

112

The particle binding kinetics in water is very different with that in air. Flow, electrostatic force, Van Der Waal force, Brownian motion and optical radiation force (Arnold et.al. 2009) dominate the movement of particles. There is a fairly small probability that the particle binds on to the silica surface upon collision and there is higher probability that a particle gets removed from resonator surface in water. Modification of the surface is needed to ensure efficient capture of target nanoparticle or molecules. But additional steps of surface functionalization may again decrease the quality factor thus decrease the sensitivity.

The second approach of bringing the molecules to the resonator is by extracting molecules from water. Ionization (sample preparation process in Mass spectrometry) or electro-spraying the biological samples followed by drying them in air flow are the possible methods. The measurements can be done in air of vacuum, thus the high-sensitivity of microresonator will be maintained. The disadvantage of the approach is that it is not an in vivo method.

In order to increase sensitivity, fabrication have been improved to achieve resonators with smaller mode volumes and higher quality factors. Meanwhile, there is a great demand in performing measurements with ultra low samples concentrations at single particle/molecule resolutions. Therefore, transporting trace amount of molecules or particles in a solution to nano- or micro-scale sensing area within a reasonable time have emerged as a problem for practical applications of these sensors. Thus, efficient ways of sample collection and delivery are in urgent need to improve the detection capabilities of these sensors in various environments (Sheehan and Whitman 2005, Zhu, Ozdemir and Yang 2011).

6.3 Conclusions

We have reported the theory and experiments of several schemes utilizing mode splitting phenomena for detection and measurement of nanoparticles. These techniques are still in development stage. However, they have shown great potential for detecting nanoscale objects at single particle level. In order to achieve selectivity and specificity in sensing, various surface functionalization techniques have been developed and affectively used in photopic crystal and WGM resonators employing spectral shift method

(Soria et.al. 2011). Although detection and measurement of individual nanoparticles and virions have been achieved using mode splitting in WGM resonators, there has been no report whether surface functionalized resonators could undergo mode splitting and enable the detection of specific nanomaterials. This should be investigated and realized to make use of the full potential of mode splitting technique. Currently, WGM resonators are generally fabricated from silica or silicon with a small number of reports on chalcogenide glass based resonators (Hu et.al. 2008). Investigating and developing new materials for WGM resonators will immensely help for the progress of WGM sensing field.

In conclusion, WGM microresonators have been demonstrated to be a great tool for studying single nanoparticle and its dynamics, they also have the potential to detect trace amount of disease markers, screening of drugs and studying protein folding, etc. Developing tools to integrate WGM resonators with microfluidic platforms without sacrificing the quality factors and mode volumes of the resonators would greatly contribute to biomolecular and biochemical sensing.

References

[1] S. Arnold, et. al., "Shift of whispering-gallery modes in microspheres by protein adsorption," *Opt. Lett.* 28, 272-274 (2003)

[2] S. Arnold, D. Keng, S. I. Shopova, S. Holler, W. Zurawsky, and F. Vollmer, "Whispering gallery mode carousel C a photonic mechanism for enhanced nanoparticle detection in biosensing," *Opt. Express* 17, 6230-6238 (2009)

[3] S. Arnold, S. I. Shopova, and S. Holler, "Whispering gallery mode bio-sensor for label-free detection of single molecules: thermo-optic vs. reactive mechanism," *Opt. Express* 18, 281-287 (2010)

[4] D. K. Armani, T. J. Kippenberg TJ, S. M. Spillane, K. J. Vahala, "Ultrahigh-Q toroid microcavity on a chip," *Nature*, 421:925-928, (2003).

[5] A. M. Armani, R. P. Kulkarni, S. E. Fraser, R. C. Flagan and K. J. Vahala, "Label-Free, Single-Molecule Detection with Optical Microcavities," *Science* 10, 783-787, (2007).

[6] S. Banerjee and A. Campbell, "Principles and mechanisms of sub-micrometer particles removal by CO2 cryogenic technique," *J. of Adhesion Sci. and Technology* 19(9) 739-751 (2005).

[7] V.B. Braginsky, M.L. Gorodetsky, V.S. Ilchenko, "Quality-factor and nonlinear properties of optical whispering-gallery modes," *Physics Letters A*, 137, 7-8, (1989).

[8] G. Brambilla, G. Senthil Murugan, J. S. Wilkinson, and D. J. Richardson, "Optical manipulation of microspheres along a subwavelength optical wire," *Opt. Lett.*, vol. 32, pp. 3041-3043, 2007.

[9] G. Brambilla, et. al., "Optical fiber nanowires and microwires: fabrication and applications," *Adv. Opt. Photon.*, vol. 1, pp. 107-161, 2009.

[10] T.P. Burg, et. al., "Weighing of biomolecules, single cells and single nanoparticles in fluid," *Nature*, vol. 446, pp. 1066-1069, 2007.

[11] M. Cai, O. Painter, and K. J. Vahala, "Observation of critical coupling in a fiber-taper to silica-microsphere Whispering-Gallery mode system," *Phys. Rev. Lett.* 85, 74-77 (2000).

[12] T. Carmon, L. Yang and K.J. Vahala, Dynamical thermal behavior and thermal self-stability of microcavities, *Opt. Express* 12, 4742-4750 (2004).

[13] T. Carmon, et. al., "Static Envelope Patterns in Composite Resonances Generated by Level Crossing in Optical Toroidal Microcavities," *Phys. Rev. Lett.* **100**, 103905 (2008).

[14] L. Chantada, N. I. Nikolaev, A. L. Ivanov, P. Borri, and W. Langbein, "Optical resonances in microcylinders: response to perturbations for biosensing," *J. Opt. Soc. Am. B* 25: 1312-1321. (2008).

[15] V. L. Colvin, "The potential environmental impact of engineered nanomaterials," *Nature Biotechnology* 21, 1166-1170 (2003).

[16] M. L. Gorodetsky, A. D. Pryamikov, V. S. Ilchenko, "Rayleigh scattering in high-Q microspheres," *J Opt Soc Am B* 17:1051-1057. (2000).

[17] I. S. Grudinin, V. S. Ilchenko, L. Maleki, "Ultrahigh optical Q factors of crystalline resonators in the linear regime," *Physical review. A*, 74, 063806 (2006).

[18] I. S. Grudinin, et. al., "Phonon Laser Action in a Tunable Two-Level System," *Phys. Rev. Lett.* **104**, 083901 (2010).

[19] F. T. Gucker and D. G. Rose, "A photoelectronic instrument for counting and sizing aerosol particles," *Br. J. Appl. Phys.*, vol. 5, 1954.

[20] A. Haddadpour and Y. Yi, "Metallic nanoparticle on micro ring resonator for bio optical detection and sensing," *Biomed. Opt. Express* 1, 378-384 (2010)

[21] N. M. Hanumegowda, C. J. Stica, B. C. Patel, I. White, and X. Fan, "Refractometric sensors based on microsphere resonators," *Appl. Phys. Lett.* 87, 201107 (2005).

[22] L. He, S. K. Ozdemir, J. Zhu, W. Kim, and L. Yang, "Detecting single viruses and nanoparticles using whispering gallery microlasers," *Nature Nanotechnology* 6, 428C432 (2011).

[23] S. V. Heringa, M. R. Stolzenburga, F. R. Quantb, D. R. Oberreitb, P. B. Keady, "A Laminar-Flow, Water-Based Condensation Particle Counter (WCPC)," *Aerosol Sci. Technol.*, vol. 39, pp. 659-672, 2005.

[24] J. B. Heroux, S. Boughaba, I. Ressejac, E. Sacher and M. Meunier, "CO2 laser-assisted removal of submicron particles from solid surfaces," *J. Appl. Phys.* 79, 2857 (1996).

[25] P. H. Hoet, I. Bruske-Hohlfeld, and O. V. Salata, "Nanoparticles - known and unknown health risks," *J. Nanobiotechnol.* 2, 2-12 (2004).

[26] J. Hu, et. al., "Demonstration of chalcogenide glass racetrack microresonators," *Opt. Lett.* 33, 761-763 (2008).

[27] D. Jackson, *Classical Electrodynamics* (Wiley and Sons, New York, 1962).

[28] W. Kim, S. K. Ozdemir, J. Zhu, L. He, L. Yang, "Demonstration of mode splitting in an optical microcavity in aqueous environment," *Appl Phys Lett* 97:071111-071113, (2010).

[29] T. Kipp, H. Welsch, Ch. Strelow, Ch. Heyn, and D. Heitmann, "Optical Modes in Semiconductor Microtube Ring Resonators," *Phys. Rev. Lett.* 96, 077403 (2006).

[30] T. J. Kippenberg, S. M. Spillane, and K. J. Vahala, "Modal coupling in traveling-wave resonators," *Opt. Lett.* 27, 1669-1671 (2002)

[31] T. J. Kippenberg, S. M. Spillane, and K. J. Vahala, "Demonstration of ultra-high-Q small mode volume toroid microcavities on a chip," *Appl. Phys. Lett.* 85, 6113 (2004).

[32] T. J. Kippenberg, S. M. Spillane, D. K. Armani, and K. J. Vahala, "Ultralow-threshold microcavity Raman laser on a microelectronic chip," *Opt. Lett.* 29, 1224-1226 (2004)

[33] T.J. Kippenberg, H. Rokhsari, T. Carmon, A. Scherer, and K. J. Vahala, "Analysis of Radiation-Pressure Induced Mechanical Oscillation of an Optical Microcavity," *Phys. Rev. Lett.* **95**, 033901 (2005).

[34] T.J. Kippenberg and K.J. Vahala, "Cavity Opto-Mechanics," *Opt. Express.* 15, 17172-17205 (2007).

[35] J. C. Knight, G. Cheung, F. Jacques, and T. A. Birks, "Phase-matched excitation of whispering-gallery-mode resonances by a fiber taper," Opt. Lett. 22, 1129-1131 (1997)

[36] R.G. Knollenberg, "The measurement of latex particle sizes using scattering ratios in the rayleigh scattering size range," *J. of Aerosol Sci.* 20, 331-345 (1989).

[37] E. O. Knutson and K. T. Whitby, "Aerosol Classification by Electric Mobility: Apparatus, Theory, and Applications," *J. Aerosol Sci.* 6, 443-451 (1975).

[38] B. Koch, Y. Yi, J.-Y. Zhang, S. Znameroski, and T. Smith, "Reflection-mode sensing using optical microresonators," *Appl. Phys. Lett.* 95, 201111 (2009).

[39] S.-B. Lee, et. al., "Observation of an Exceptional Point in a Chaotic Optical Microcavity," *Phys. Rev. Lett.* 103, 134101 (2009).

[40] B. E. Little and S. T. Chu, Estimating surface-roughness loss and output coupling in microdisk resonators, *Opt. Lett.* 21, 1390C1392 (1996).

[41] Y. F. Lu, et. al., "Removal of submicron particles from nickel-phosphorus surfaces by pulsed laser irradiation," *Appl. Surf. Sci.*, 120, 317-322 (1997).

[42] T. Lu, et. al., "High sensitivity nanoparticle detection using optical microcavities," *Proc. Natl. Acad. Sci. USA.*, 108 (13): 5141-5472 (2011).

[43] P. Leiderer, et al. "Laser-induced particle removal from silicon wafers," *High-power Laser Ablation III, Santa Fe (USA), Proc. SPIE* 4065, 249-259. (2000).

[44] B.Y.H. Liu and D.Y.H. Pui, "A Submicron Aerosol Standard and the Primary, Absolute Calibration of the Condensation Nuclei Counter," *J. Colloid Interface Sci.* 47, 155-171 (1974).

[45] McDermott, et al., "Surface cleaning using an argon or nitrogen aerosol," US patent 5, 294, 261 (1994).

[46] A. Mazzei, et al. Controlled coupling of counterpropagating whispering-gallery modes by a single Rayleigh scatterer: a classical problem in a quantum optical light. *Phys Rev Lett* 99: 173603. (2007)

[47] T. G. McRae, K. H. Lee, M. McGovern, D. Gwyther, and W. P. Bowen, "Thermo-optic locking of a semiconductor laser to a microcavity resonance," *Opt. Express* 17, 21977-21985 (2009)

[48] A. K. Naik, M. S. Hanay, W. K. Hiebert, X. L. Feng, M. L. Roukes, "Towards single-molecule nanomechanical mass spectrometry," *Nat. Nanotechnol.*, vol. 4, pp. 445C450, 2009.

[49] A. Otto, "Excitation of nonradiative surface plasma waves in silver by the method of frustrated total reflection," *Z. Physik* 216, 398-410 (1968).

[50] S. K. Ozdemir, J. Zhu, L. He and Lan Yang, "Estimation of Purcell factor from mode-splitting spectra in an optical microcavity," *Phys. Rev. A* 83, 033817 (2011).

[51] Hai-Cang Ren, Frank Vollmer, Stephen Arnold, and Albert Libchaber, "High-Q microsphere biosensor - analysis for adsorption of rodlike bacteria," *Opt. Express* 15, 17410-17423 (2007)

[52] S. M. Spillane, T. J. Kippenberg, O. Painter, and K. J. Vahala, "Ideality in a Fiber-Taper-Coupled Microresonator System for Application to Cavity Quantum Electrodynamics," *Phys. Rev. Lett.* 91, 043902 (2003).

[53] B. S. Schmidt, A. H. Yang, D. Erickson, M. Lipson, "Optofluidic trapping and transport on solid core waveguides within a microfluidic device," *Opt. Express*, vol. 15, pp. 14322C14334, 2007.

[54] C. Schmidt, et al. "Nonlinear thermal effects in optical microspheres at different wavelength sweeping speeds," *Opt. Express* 16, 6285-6301 (2008).

[55] G. Senthil Murugan, G. Brambilla, J. S. Wilkinson, D. J. Richardson, "Optical Propulsion of Individual and Clustered Microspheres along Sub-Micron Optical Wires," *Jpn. J. Appl. Phys.*, vol. 47, pp. 6716-6718, 2008.

[56] P. E. Sheehan and L. J. Whitman, "Detection Limits for Nanoscale Biosensors," *Nano Lett.,* 5 (4), 803C807, (2005).

[57] F.-W. Sheu, H.-Y. Wu, S.-H. Chen, "Using a slightly tapered optical fiber to attract and transport microparticles," *Opt. Express*, vol. 18, pp. 5574-5579, 2010.

[58] Ch. Strelow, H. Rehberg, C. M. Schultz, H. Welsch, Ch. Heyn, D. Heitmann, and T. Kipp, "Optical Microcavities Formed by Semiconductor Microtubes Using a Bottlelike Geometry," *Phys. Rev. Lett.* 101, 127403 (2008)

[59] W. D. Song, et. al., "Laser-induced removal of plate-like particles from solid surfaces," Appl. Surf. Sci. 186, 69-74 (2002).

[60] S. Soria, et. al., "Optical Microspherical Resonators for Biomedical Sensing," *Sensors* 11, 785-805, (2011).

[61] M. Sumetsky, "Whispering-gallery-bottle microcavities: the three-dimensional etalon," Opt. Lett. 29, 8-10 (2004)

[62] K.J. Vahala, "Optical microcavities," *Nature* **424**, 839-846 (2003).

[63] J. Villatoro and D. Monzon-Hernandez, "Fast detection of hydrogen with nano fiber tapers coated with ultra thin palladium layers," *Opt. Express*, vol. 13, pp. 5087-5092, 2005.

[64] F. Vollmer, D. Braun, A. Libchaber, M. Khoshsima, I. Teraoka, and S. Arnold, "Protein detection by optical shift of a resonant microcavity," *Appl. Phys. Lett.* 80(21), 4057C4059 (2002).

[65] F. Vollmer, S. Arnold, "Whispering-gallery-mode biosensing: label-free detection down to single molecules," *Nature. Meth.*, vol. 5, pp. 591-596, 2008.

[66] F. Vollmer, S. Arnold, D. Keng, "Single virus detection from the reactive shift of a whispering-gallery mode," *Proc. Natl. Acad. Sci. USA.*, vol. 105, pp. 20701-20704, 2008.

[67] S. P. Wang, et. al., Label-free imaging, detection, and mass measurement of single viruses by surface plasmon resonance. *Proc Natl Acad Sci USA* 107:16028-16032. (2010).

119

[68] M. Watanabe, T. Sanada, A. Hayashida and Y. Isago, "Cleaning technique using high-speed steam-water mixed spray," *Solid State Phenomena*, 145-146, 43-46 (2009).

[69] D. S. Weiss, et al., "Splitting of high-Q Mie modes induced by light backscattering in silica microspheres," *Opt Lett* 20:1835-1837. (1995)

[70] I. M. White, H. Oveys, and X. Fan, "Liquid-core optical ring-resonator sensors," *Opt. Lett.* 31, 1319-1321 (2006)

[71] Q. Xu, D. Fattal, and R. G. Beausoleil, "Silicon microring resonators with 1.5 μm radius," Opt. Express 16, 4309-4315 (2008).

[72] L. Yang, T. Carmon, B. Min, S. M. Spillane, and K. J. Vahala, "Erbium-doped and Raman microlasers on a silicon chip fabricated by the sol-gel process," *Appl. Phys. Lett.* 86, 091114 (2005).

[73] C. Zhao, et. al., "Three-Mode Optoacoustic Parametric Amplifier: A Tool for Macroscopic Quantum Experiments," *Phys. Rev. Lett.*, 102, 243902 (2009).

[74] J. Zhu, et. al., "On-chip single nanoparticle detection and sizing by mode splitting in an ultrahigh-Q microresonator," *Nat. Photonics*, vol. 4, pp. 46-49, 2010.

[75] J. Zhu, S. K. Ozdemir, L. He, D.-R. Chen, and L. Yang, "Single virus and nanoparticle size spectrometry by whispering-gallery-mode microcavities," *Opt. Express* 19, 16195-16206 (2011)

[76] J. Zhu, S. K. Ozdemir, L. He, and Lan Yang, "Controlled manipulation of mode splitting in an optical microcavity by two Rayleigh scatterers," *Opt. Express* 18, 23535-23543 (2010)

[77] J. Zhu, S. K. Ozdemir and L. Yang, "Optical Detection of Single Nanoparticles With a Subwavelength Fiber-Taper," *Photonics Technology Letters, IEEE,* 23, 1346 - 1348 (2011).

[78] J. Zhu, S. K. Ozdemir and L. Yang, "Bypassing the diffusion limit," *Nature Photonics* 5, 653C654 (2011)

Vita

Jiangang Zhu

Date of Birth   August 30, 1984

Place of Birth   Jiangyin, Jiangsu, China

Degrees   Ph.D. Electrical Engineering, Washington University, 2011
B.S. Automation, Tsinghua University, 2006

Professional   Institute of Electrical and Electronic Engineers
Societies   Optical Society of America
American Physical Society
Society of Photo-Optical Instrumentation Engineers

Publications   [1] J. Zhu, S. K. Ozdemir, L. Yang. Bypassing the diffusion limit, *Nature Photonics* 5, 653-654 (2011)

[2] J. Zhu, S. K. Ozdemir, L. He and L. Yang. Optothermal spectroscopy of whispering gallery microresonators, *Applied Physics Letters* 99, 171101 (2011)

[3] J. Zhu, S. K. Ozdemir, L. He, D.-R. Chen and L. Yang. Single virus and nanoparticle spectrometry using whispering-gallery-mode optical microcavities, *Optics Express* 19, 16195-16206 (2011). Selected for publication in the Virtual Journal for *Biomedical Optics*, Vol. 6, Iss. 9.

[4] L. He, S. K. Ozdemir, J. Zhu, W. Kim, L. Yang. Detecting single viruses and nanoparticles using whispering gallery microlasers, *Nature Nanotechnology* 6, 428-432 (2011).

[5] J. Zhu, S. K. Ozdemir and L. Yang. Optical Detection of Single Nanoparticles with a Nano Fiber-Taper, *Photonics Technology Letters, IEEE* 23, 1346-1348 (2011).

[6] W. Kim, S. K. Ozdemir, J. Zhu and L. Yang. Observation and characterization of mode splitting in microsphere resonators in aquatic environment, *Applied Physics Letters* 98, 141106 (2011)

[7] S. K. Ozdemir, J. Zhu, L. He and L. Yang. Estimation of Purcell factor from mode-splitting spectra in an optical microcavity, *Phys. Rev. A* 83, 033817 (2011)

[8] L. He, S. K. Ozdemir, J. Zhu and L. Yang. Ultra sensitive detection of mode splitting in an active optical microcavity, *Phys. Rev. A* 82, (2010)

[9] J. Zhu, S. K. Ozdemir, L. He and L. Yang. Controlled Manipulation of Mode Splitting in an Optical Microcavity by Two Rayleigh Scatterers, *Optics Express* 18, (2010)

[10] W. Kim, S. K. Ozdemir, J. Zhu, L. He and L. Yang. Demonstration of mode splitting in an optical microcavity in aqueous environment, *Applied Physics Letters* 97, (2010)

[11] L. He, S. K. Ozdemir, J. Zhu and L. Yang. Scatterer induced mode splitting in poly(dimethylsiloxane) coated microresonators, *Applied Physics Letters* 96, (2010)

[12] L. He, S. K. Ozdemir, J. Zhu and L. Yang. Self-pulsation in fiber-coupled on-chip microcavity lasers, *Optics Letters* 35, (2010)

[13] J. Zhu, S. K. Ozdemir, Y.-F. Xiao, L. Li, L. He, D.-R. Chen and L. Yang. On-chip Single Particle Detection and Sizing by Mode Splitting in a Ultra-high-Q Microtoroid, *Nature Photonics* 4, 46 - 49 (2010)

[14] L. He, Y.-F. Xiao, J. Zhu, S. K. Ozdemir, and L. Yang. Oscillatory thermal dynamics in high-Q PDMS-coated silica toroidal microresonators, *Optics Express* 17, 9571-9581 (2009)

[15] Y.-F. Xiao, L. He, J. Zhu, and L. Yang. Electromagnetically induced transparency-like effect in a single polydimethylsiloxane coated silica microtoroid, *Applied Physics Letters* 94 (2009)

[16] L. He, Y.-F. Xiao, C. Dong, J. Zhu, V. Gaddam, and L. Yang. Compensation of thermal refraction effect in high-Q toroidal microresonator by polydimethylsiloxane coating, *Applied Physics Letters* 93 (2008).

December 2011

Microresonator Nanoparticle Sensing, Zhu, Ph.D. 2011